OCEAN ENGINEERING GROUP

Computational Modeling of FPSO Hull Roll Motions and Two–component Marine Propulsion Systems

Karan Kakar

August 2002

Report No. 02–3

ENVIRONMENTAL AND WATER RESOURCES ENGINEERING

DEPARTMENT OF CIVIL ENGINEERING

THE UNIVERSITY OF TEXAS AT AUSTIN

Austin, TX 78712

Computational Modeling of FPSO Hull Roll Motions and Two-component Marine Propulsion Systems

by

Karan Kakar, B.Tech.

Thesis

Presented to the Faculty of the Graduate School

of The University of Texas at Austin

in Partial Fulfillment

of the Requirements

for the Degree of

Master of Science in Engineering

The University of Texas at Austin

August 2002

Computational Modeling of FPSO Hull Roll Motions and Two-component Marine Propulsion Systems

APPROVED BY
SUPERVISING COMMITTEE:

Supervisor: _____

Spyros A. Kinnas

_____

To my parents and my sister

Acknowledgements

This thesis marks the culmination of a two year learning process, and this journey would not have been possible without the encouragement and guidance of several people. I would like to express my greatest appreciation and gratefulness to Dr. Spyros Kinnas, without whose support and faith I would not have been able to pursue my Masters study in the United States. Over the last two years, he has been a patient teacher, a mentor, an advisor and for all this, sir, I thank you.

I would also like to thank Dr. Ben Hodges for taking time off his busy schedule and reading this thesis and providing valuable input and comments.

I would like to take this opportunity to thank my family. I owe much of what I am today to the love and the values instilled in me by my parents and their constant support and confidence in me and my abilities.

Computational Modeling of FPSO Hull Roll Motions and Two-component Marine Propulsion Systems

by

Karan Kakar, M.S.E.

The University of Texas at Austin, 2002

SUPERVISOR: **Spyros A. Kinnas**

An iterative method, coupling a vortex lattice based potential flow solver and finite volume based Euler solver, is used to model the interaction between components of a multi-component marine propulsion system. The purpose of using the above approach is to determine the effective wake (modified in the presence of the other components) and evaluate the performance of each component subject to this modified effective inflow velocity. The method has been applied to the stator-rotor couple as well as to study the performance of podded propulsors.

The thesis work is extended to include the development of a two-dimensional unsteady Euler and laminar Navier-Stokes solver, based on the pressure correction scheme, to model the roll motions and separated flow past the bilge keels on a

Floating, Production, Storage and Offloading (FPSO) vessel hull and accurately determine the two-dimensional roll added mass and damping coefficients. This computational tool can be coupled with an existing potential based hull motion solver like WAMIT, to predict the motion of a hull subject to a three-dimensional wave environment.

Table of Contents

List of Tables

List of Figures

xiv

Nomenclature

Latin Symbols

a	wave amplitude
a_{ij}	added-mass coefficient
b_{ij}	damping coefficient
B	beam of the ship
c	wave celerity, $c = \sqrt{\frac{gL_o}{2\pi}}$
C_d	drag coefficient
C_m	inertia coefficient
C_Q	torque coefficient based on V_s, $C_Q = \frac{Q}{0.5\rho V_s^2 \pi R^3}$
C_T	thrust coefficient based on V_s, $C_T = \frac{T}{0.5\rho V_s^2 \pi R^2}$
d	water depth
D	propeller diameter, $D = 2R$, or
	draft of the ship
$\vec{f}$	$= (f_x, f_y, f_z)$, body force per unit mass
$\mathbf{F}$	column matrix for the x derivative terms
Fn	Froude number based on propeller diameter D, $Fn = \frac{n^2 D}{g}$
Fn_b	Froude number based on half-beam b, $Fn_B = \omega\sqrt{\frac{b}{g}}$
Fn_B	Froude number based on beam B, $Fn_B = \omega\sqrt{\frac{B}{g}}$
Fn_D	Froude number based on draft D, $Fn_D = \omega\sqrt{\frac{D}{g}}$
F_x, F_y	non-dimensionalized total x- and y-direction force
g	gravitational acceleration

G	column matrix for the y or r derivative terms
h	height of flat plate
H	height of 2-D channel
H	column matrix for the z or θ derivative terms
J_s	advance ratio based on V_s, $J_s = \frac{V_s}{nD}$
k	wave number, $k = \frac{2\pi}{L}$
K	Keulegan-Carpenter number
K_D	non-dimensional bilge-keel depth
K_Q	torque coefficient based on n, $K_Q = \frac{Q}{\rho n^2 D^5}$
K_T	thrust coefficient based on n, $K_T = \frac{T}{\rho n^2 D^4}$
L	reference length used in non-dimensionalization, or
	wavelength, or length of 2-D channel
L_o	deep-water wavelength
M_z	moment about the z axis
n	propeller rotational frequency (rev/s)
$\vec{n}$	$= (n_x, n_y, n_z)$, normal vector
p	pressure, $p = p_{Static} + \rho g z$, where z is the depth
p_{atm}	atmospheric pressure
P_v	vapor pressure of water
$\vec{q}$	$= (q_x, q_y)$, body velocity
$\vec{q_e}, \vec{q_p}, \vec{q_t}$	effective wake, propeller induced and total velocity vector
$\vec{q_i}, \vec{q_r}$	irrotational and rotational velocity vector
Q	propeller torque, or
	mass flow rate
Q	column matrix containing the source terms
Q_M	residual of the continuity equation

R	propeller radius
Re	Reynolds number based on reference length L, $Re = \frac{\rho U_\infty L}{\mu}$
S_{ij}	area of cell in two-dimensional formulation
t	non-dimensional time
T	propeller thrust, or
	time period of motion
$\mathbf{U}$	column matrix for time derivative terms
U_∞	flow velocity at infinity
U_m	amplitude of oscillating velocity function
U_o	amplitude of heave velocity
u, v, w	x, y and z-direction velocities
u_x, u_r, u_θ	axial, radial and circumferential velocities
$\vec{v}$	$= (u, v, w)$ or (u_x, u_r, u_θ), total velocity vector
V_s	ship speed
$\hat{\mathcal{V}}_c$	computational cell volume
w	width of flat plate
$\vec{x}$	$= (x, y, z)$ or (x, r, θ), location vector on the ship fixed
	coordinate system
(x, r, θ)	downstream, radial and circumferential coordinates respectively
(x, y, z)	downstream, upward and port side coordinates respectively
X_e	axial location where effective velocity is determined
X_p	axial location of propeller plane

Greek Symbols

α	angle of roll for FPSO hull, $\alpha = \alpha_o sin\omega t$
α_o	amplitude of roll motion
β	shaft yaw angle, or
	artificial compressibility factor
Δp	pressure difference
Δt	time step size
$(\Delta x, \Delta y)$	cell size in x and y direction
η	vertical coordinate of free surface
Γ	propeller blade circulation
μ	dynamic viscosity of water
ν	kinematic viscosity of water
ω	propeller angular velocity, or
	frequency of periodic heave and roll forcing function
$\vec{\omega}$	$= (\omega_x, \omega_y, \omega_z)$, vorticity vector
ϕ_p	perturbation potential
ρ	fluid density
σ_n	cavitation number based on n, $\sigma_n = (P_o - P_v)/(0.5\rho n^2 D^2)$
θ	phase of the wave, $\theta = kx - \omega t$

Subscripts

$1, 2, 3, 4, ...$	node numbers
$A, B, C, D, ...$	cell indices
(i, j, k)	node or cell indices in each direction;
	i is axial, j is radial, and k is circumferential.
N, W, S, E, T, B	face (in three-dimension) or edge (in axisymmetric) indices
	at north, west, south, east, top, and bottom of a cell
T, I, E	total, propeller induced, and effective wake velocities
	(in some figures)

Superscripts

$*$	intermediate velocity or pressure
$'$	velocity or pressure correction
$n, n+1$	time step indices

Acronyms

BEM	Boundary Element Method
CFD	Computational Fluid Dynamics
CPU	Central Processing Unit (time)
DBC	Dynamic Boundary Condition
DTMB	David Taylor Model Basin
DTNSRDC	David Taylor Naval Ship Research and Development Center
FPSO	Floating, Production, Storage and Offloading (vessels)
FVM	Finite Volume Method
KBC	Kinematic Boundary Condition
MIT	Massachusetts Institute of Technology
RANS	Reynolds Averaged Navier-Stokes (equations)
SIMPLE	Semi-Implicit Method for Pressure Linked Equations
VLM	Vortex Lattice Method

Computer Program Names

DTNS3D	MIT's RANS code
FLUENT	commercial CFD software
GBFLOW-3X	axisymmetric steady Euler solver
GBFLOW-3D	three-dimensional steady Euler solver
MPUF-3A	cavitating propeller potential flow solver based on VLM
NS2D	laminar 2D Navier-Stokes solver developed at U.T. Austin
PBD-14	MIT's propeller lifting line solver
PROPCAV	cavitating propeller potential flow solver based on BEM
WAMIT	panel method based wave-structure interaction analyzer

Chapter 1

Introduction

1.1 Background

This thesis presents work done towards the computational modeling of FPSO hull roll motions as well as modeling of flow around a two-component propulsion system. These two topics, though seemingly disparate, are bound together by the fact that the same equations govern the fluid behavior and therefore the same numerical method can be extended to solve for both problems. The next section gives a general introduction to the two problems.

1.1.1 Multi-Component and Podded Propulsors

Multi-component and podded propulsor systems are becoming increasingly popular options for modern day commercial marine vessels. Multi-component propulsors can offer higher efficiencies due to the cancellation of the flow swirl (rotation) downstream of the propulsor. They can also reduce the overall amount of propeller blade cavitation, as each component carries a fraction of the required thrust. Types of multi-component propulsors include contra-rotating propellers, pre- or post-swirl stator-rotor combinations, and these can be open, ducted, podded, integrated (with the hull), or internal (such as the impeller system of a water-jet). Detailed results for a stator-rotor and podded type of propulsion system are presented in Chapter 4.

1

The last few years have seen a breakthrough in the application of podded propulsors. The concept of an azimuthal, submerged, electrically driven pull propeller provides various advantages in terms of efficiency, controllability, comfort and vessel lay-out. With a continuous rotation angle of 360° about the vertical axis, the pod ensures optimum maneuverability for commercial vessels as well as for offshore dynamic positioning. A podded propulsor such as the Siemens Schottel Propulsor (SSP) [Blenkey 1997] (shown in Figure 1.1) replaces the steering and propulsion systems of vessels; gives optimum maneuverability without additional stern thrusters; lowers noise and vibration thanks to special supports; occupies less space and requires a smaller engine room than a conventional system; can be installed later in the construction stage than the conventional system, saving on construction time and costs. Further advantages claimed for the SSP are: no risk of vibration excitation by gear sets and cooling fans; simple surface-cooled motor; mounting of the lower housing is possible without drydocking.

These new devices still have to prove their long term integrity and reliability. More information is required on the design loads and design specifications for podded propulsors in service as these devices significantly differ from conventional propellers. Extensive CFD (Computational Fluid Dynamics) analysis and model tank tests are required to develop a pod shape with enhanced efficiency and maneuvering characteristics. CFD analysis would also help quantify the improvement in propulsive efficiency offered by podded propulsors and, combined with design tools, can be used to achieve optimum pod shapes. The present work presents the analysis of flow past a simple podded propulsor geometry, for different propeller configurations, in Chapter 4.
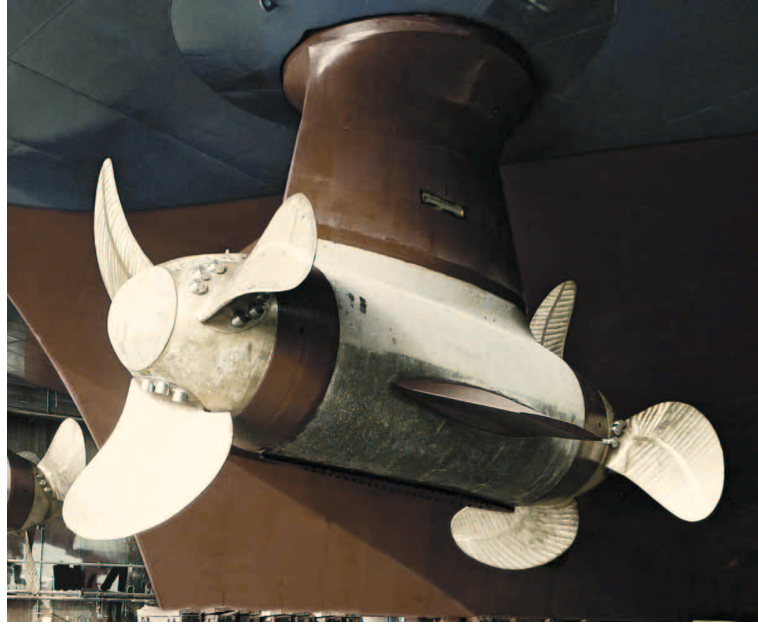
Figure 1.1: Photograph showing details of the Siemens Schottel Propulsor (downloaded from the website *www.is.siemens.de/presse/*)

1.1.2 Prediction of Hull Motions

A floating body subject to a multi-component three-dimensional wave environment has six degrees of motion. The three translational degrees parallel to the (x, y, z) axes are called *surge, heave* and *sway* and the three rotational degrees of freedom about the same axes are called *roll, yaw* and *pitch*, respectively. Of these six motions, the present work deals primarily with roll motion, with the relatively simpler heave motion being used as an intermediate step to validate the method.

Roll motion of a vessel can be specified by certain primary parameters. These include:

- Amplitude of motion (measured in degrees or radians)

- Period of motion (measured in seconds, typical periods range from 20-30 sec-

3

onds)

- Rate of Decay (number of cycles to rest).

Floating, Production, Storage and Offloading (FPSO) vessels operating in deep waters need to maintain their position in order to facilitate proper functioning and hence the modeling and control of roll motions assumes great importance for such vessels. Field observations indicate that FPSO roll motions are larger than expected based on their design and model tests. This can potentially lead to riser fatigue and operational difficulties. The use of suitably located bilge keels (defined as *either of two projecting flanges extending along the bilge of a ship to reduce rolling*) is known to effectively mitigate the extent of these motions. According to [Kasten 2002], for small craft, the long, low aspect ratio bilge keels offer roll reduction of the order of 35% to 55% and their efficacy is independent of the vessel speed. The bilge keels offer additional frictional resistance due to increased wetted surface area. Certain other roll attenuation strategies include Passive Anti-Roll Tanks, Active Fin Stabilizers, etc. However, for large vessels like FPSO's the bilge keels offer a relatively simple and inexpensive option.

One of the most challenging tasks in modern ship design is accurately predicting extreme loads and resulting hull responses while a ship is operating in severe seas. The lack of adequate computational tools for the prediction of ship responses in extreme seas arises primarily due to the complexity of the problem and our limited knowledge of the actual governing physics. Therefore, modeling the complex flow around the sharp-fin like bilge keels in the presence of the hull geometry and a free surface is essential in order to accurately determine the effectiveness of the bilge keels in roll motion mitigation. This thesis presents the development of a numerical

model to determine the hydrodynamic coefficients for a two-dimensional body undergoing heave and roll motions at the free surface of a fluid. Hull geometries with and without bilge keels are modeled and the hydrodynamic coefficients for different bilge-keel depths are compared. The developed tool could, in the long run, serve as a design aid for designing bilge keels fitted to FPSO hulls. It would allow the designer to experiment with various orientations and lengths of the keels, and thus arrive at an optimum bilge keel depth and also allow visualization of the resulting flow characteristics and motion decay.

1.2   Motivation

The inflow at the propeller plane, observed in the absence of the propeller is known as *nominal wake*. This flow field contains strong vorticity generated by the boundary layer along the ship hull upstream of the propeller.

Use of accurate and fast potential flow solvers to model the flow field around a rotating propeller results in the vorticity in the flow-field being neglected. To improve the accuracy in the prediction of the flow-field, the inflow to the propeller is corrected to include the interaction between the propeller and the vorticity in the inflow. This corrected inflow is known as *effective wake*. Accurate knowledge of the effective wake is essential in assessing the propeller design and performance, especially for an unsteady phenomenon such as blade cavitation.

The presence of multiple-blade rows adds to the complexity of the problem. Now the effective wake as "seen" by each component should include the influence of the other component as well. Thus the solver needs to be able to model the three-way interaction between the inflow and the two-components of the propulsion system. This is achieved by coupling a Vortex Lattice Method based potential flow

solver (VLM) [Kinnas et al. 1998] with an axisymmetric and three-dimensional Euler solver [Choi 2000]. An iterative process is performed between the two solvers, with the VLM used to model each component individually and the Euler solver used to determine the total flow field, in the presence of both components. The above described iterative procedure can also be used analyze the flow around podded propulsor geometries. By studying the pressure distribution on the surface of the pod and strut, an optimum design can be chosen so as to minimize pressure drag and flow separation (see [Vartdal et al. 1999]) and this can lead to an improvement in the propulsive efficiency of a podded propulsor.

Hydrodynamic solvers, based on potential flow theory, such as WAMIT (Waves at MIT) are used to determine the added mass and damping coefficients for a ship undergoing motions. Potential flow theory does not allow for lifting or separation effects. In order to improve the accuracy in predicting the hydrodynamic coefficients, an unsteady Euler solver, based on the pressure correction method, is required to capture the vortices shed off the bilge keels.

The primary motivation in using Euler solvers is that they offer a sufficiently accurate and computationally faster alternative to Reynolds Averaged Navier-Stokes (RANS) solvers. The RANS solver has the advantage that the effect of viscosity is included in the computation, but it requires a large number of cells concentrated near the no-slip wall boundaries, for example the hull and the hub. The choice of solver used depends on the nature of the problem being solved, for if viscous effects are important for a problem, an Euler solver can not capture the flow-field accurately. Viscous effects can be neglected when considering the global flow around a propeller, unless one is interested in capturing the boundary layer flow close to the blade and wall surfaces. Similarly, for strongly separated flows such as vortex-

shedding seen off bilge keels, the pressure forces dominate over the viscous effects [Yeung et al. 2000]. Therefore this work aims at using a 2D/3D steady/unsteady Euler solver to determine accurately the flow, be it past the bilge keels on a ship hull or past a multiple-blade row.

1.3 Objective

The objective of the work presented here is to develop a two-dimensional unsteady Euler solver to solve the two-dimensional radiation problem due to the roll motion of a FPSO hull fitted with bilge keels. Visualization of the separated flow and vortex-shedding past the bilge keels as well as prediction of the roll hydrodynamic coefficients would be possible using the developed method.

This thesis also presents results for multi-component and podded propulsors, with the flow-field solved using an earlier developed vortex lattice method based potential flow solver [Kinnas et al. 1998] and axisymmetric/3-D steady Euler solver [Choi 2000].

1.4 Overview

The contents of the remaining chapters are summarized below:

- Chapter 2 presents a literature review of previous work on prediction of hull motions as well as flow past single- and multi-component and podded propulsors.

- Chapter 3 describes in detail the numerical formulation for a two-dimensional unsteady Euler solver, based on the finite volume method and pressure

7

correction scheme. The formulation for a viscous solver and a steady three dimensional solver is also provided, with only the primary differences from the first method being highlighted. For completeness, a brief review of the vortex lattice method based potential flow solver is also provided.

- Chapter 4 details the use of the coupled VLM and Euler solver approach as applied to the stator-rotor couple as well as podded propulsors. The chapter includes sections on grid generation, comparison with experiments as well as numerical convergence tests.

- Chapter 5 includes the numerical validations performed in order to validate the developed 2D unsteady Euler solver. Convergence studies and comparisons with a commercial CFD code, FLUENT [1] are also included in this chapter. The results for a rectangular hull undergoing heave and roll motion, obtained using the unsteady Euler solver, are presented next. Also included is the comparison with past work in roll motion modeling as well as a comparison between results from the viscous and Euler solver for the problem of oscillating flow past a flat plate.

- Chapter 6 presents a summary and conclusions of this thesis. Recommendations for future work are also given.

---

[1] Developed by *Fluent Inc.*

Chapter 2

Literature Review

The first section of this chapter discusses work done in the past on the prediction of propeller flow and propeller blade sheet cavitation using the vortex lattice method. Section 2.2 provides a brief summary of past work done on effective wake prediction for single and multi-component as well as podded propulsors. In Section 2.3, the previous work done in the field of hull motion prediction is reviewed.

2.1 Vortex Lattice Method

A vortex lattice method was introduced for the analysis of fully wetted propeller flows by [Kerwin and Lee 1978]. The method was later extended to treat unsteady sheet cavitating flows by [Lee 1979] and [Breslin et al. 1982]. Vortex and source lattices are placed on the mean camber surface of the blade, and a robust arrangement of singularities and control point spacings was employed to produce accurate results [Kinnas and Fine 1989]. In [Kinnas 1991], a leading edge correction was introduced to account for the defect of linear cavity solution near a round leading edge, and was incorporated into a code named PUF-3A. The method was then extended to treat super-cavitating propellers subjected to steady flow by [Kudo and Kinnas 1995]. Most recently, the method has been re-named MPUF-3A for its added ability to search for mid-chord cavitation [Kinnas et al. 1998]. The latest version of MPUF-

3A also includes wake alignment in circumferentially averaged inflow [Greeley and Kerwin 1982], non-linear thickness-loading coupling [Kinnas 1992], the effect of hub and wake alignment including the effect of shaft inclination [Kinnas and Pyo 1999]. However, details of the flows at the blade leading edge and tip cannot be captured accurately due to the breakdown of either the linear cavity theory or the thickness-loading coupling corrections. In addition, the current version of MPUF-3A does not include the effect of cavity sources in the thickness-loading coupling correction.

2.2   Effective Wake Prediction

Accurate "effective" wake prediction is crucial in determining the cavity extent and volume, as well as the magnitude of the predicted pressure pulse on the hull in the presence of the propeller. Experimental investigations and theoretical studies using steady axisymmetric Euler equations were first presented by [Huang et al. 1976; Huang and Cox 1977] and [Huang and Groves 1980; Shih 1988], respectively. Later, effective wake prediction methods using RANS equations were developed for axisymmetric flow applications [Stern et al. 1988a,b; Kerwin et al. 1994, 1997] and [Stern, 1994] applies the RANS equations to non-axisymmetric applications. In both methods, the propeller is represented by the body force term in the RANS equations.

In [Choi and Kinnas 1998, 2001] a steady 3-D Euler solver, based on a finite volume approach and the artificial compressibility method, was developed for the prediction of the 3-D effective wake of single propellers in unbounded flow or in the presence of a circular section tunnel.

In [Choi and Kinnas 2000a,b; Choi 2000], a fully three-dimensional unsteady Euler solver, based on a finite volume approach and the pressure correction method,

was developed and applied to the prediction of the unsteady effective wake for propellers subject to non-axisymmetric inflows. It was found that the 3-D Euler solver predicted a 3-D effective wake inflow which was very close to the time average of the fully unsteady wake inflow. In the present work the Euler solver developed in [Choi 2000] is extended to include the effects of the presence of multiple-blade rows.

2.2.1 Multi-Component Propulsors

Multi-component propulsors can offer higher efficiencies due to the cancellation of the flow swirl downstream of the propulsor. Since each component carries a fraction of the required thrust, the blade loading and therefore the overall amount of blade sheet cavitation decreases. Types of multi-component propulsors include contra-rotating propellers, pre- or post-swirl stator-rotor combinations, and they can be open, ducted, podded, integrated (with the hull), or internal (such as the impeller system of a water-jet).

There have been several efforts to design or predict the mean performance of two-stage propulsors using a lifting-line model for each one of the components.

The steady or unsteady performance of two-stage propulsors has also been predicted using a lifting-surface model for each one of the components [Tsakonas et al. 1983; Kerwin et al. 1988; Maskew 1990; Hughes 1993; Yang et al. 1992; Hughes and Kinnas 1993, 1991].

The vortex lattice method (applied to each one of the components) has been coupled with Reynolds-Averaged Navier-Stokes solvers in order to predict the performance of multi-component propulsors, including their interaction with the hull flow [Dai et al. 1991; Kerwin et al. 1994], and more recently in [Warren et al. 2000].

11

In the present work, a vortex lattice method (called MPUF-3A, refer Section 2.1) is modified to model the flow around stators. Then MPUF-3A is applied to each one of the two components (the stator and the rotor), and is coupled with an Euler solver (called GBFLOW-3X/-3D)[1], based on a finite volume method, to predict the three-way interaction between the inflow and the two stages of the propulsor.

2.2.2 Podded Propulsors

The last few years have seen a breakthrough in the application of podded propulsors. A podded propulsor is defined as a *steerable pod housing an electric motor which drives an external propeller* (definition taken from *www.sew-lexicon.com*).

A podded propulsor may be a push-type (propeller operates aft of the strut) or a pull-type (propeller operating forward of the strut). At high speeds, the efficiency of the push-type propulsor decreases due to the propeller operating in the wake peak of the vertical strut [Vartdal and Bloch 2001]. In contrast, the pull-type propeller provides various advantages in terms of efficiency, controllability, comfort and vessel lay-out [Blenkey 1997].

In [HYDROCOMP 1999], it is stated that the efficiency of podded propellers decreases on account of the large hub ($\geq$ 30% of propeller radius) and design features such as variable pitch distribution to "off-load" the tip and root areas, and a forward leading rake to increase the distance from the propeller to the pod structure immediately aft. Even though the propeller itself may be a bit less efficient, the amount of improvement of the entire system over a conventional propeller can be significant - on the order of 2%-4%. This observation highlights the need for ac-

---

[1]The latest version of WAKEFF-3X/3D which was developed at UT [Choi and Kinnas 2001; Choi 2000].

curate design and modeling tools to develop complex pod geometries which offer a distinct advantage over the conventional propeller.

Computational modeling of podded propulsors involves adapting computational grids around complex geometries. With the improvement in computer speeds and grid generation techniques, recently several researchers have applied CFD to podded propulsors. [Ghassemi and Allievi 1999] developed a potential flow method to calculate the flow around podded propulsors, and [Sanchez-Caja et al. 1999] applied a viscous code to model the flow around the podded propulsors. More recently [Hsin et al. 2002] developed a design tool for pod geometries based on a coupled potential flow/viscous method solver.

2.3   Hull Motion Prediction

Presently available techniques for the analysis of ship motions and sea loads are mostly based on potential flow assumptions. In these methods viscous effects may be accounted for by empirical, semi-empirical formulations, which limit their applications. On the other hand, a RANS equations based technique, naturally incorporates the effect of viscosity and hence, produces better results in cases where viscosity plays an important role.

Among available techniques to predict vessel motion, the strip theory based "Seakeeper"[2], or the panel method diffraction codes such as WAMIT (Waves at MIT) assume inviscid flow and operate in the frequency domain. [Klaka 2001] observes that viscous forces are important and the non-linear nature of roll response requires time domain modeling. According to [Gentaz, 1997], viscous effects are

---

[2]developed by Formation Design Systems Pvt. Ltd

important for rectangular bodies in sway or roll motion. Therefore numerical simulations based on perfect flow theory can not give satisfactory results. However, the present technique makes use of an unsteady Euler (inviscid) solver to solve for the separated flow past bilge keels because it has been shown in [Yeung and Ananthakrishnan 1992] that for strongly separated flow, the shear stress is of secondary importance. This is illustrated in Section 5.3.2, where the flow past a flat plate is determined using both an Euler and a Navier-Stokes solver. The values of the drag and inertia coefficients from both solvers compare very well with each other as well as with experiment (experimental data presented in [Sarpkaya and O'Keefe 1995]).

Some of the past work done on the subject of roll motions includes an investigation into the eddy-making damping in slow-drift motions performed by [Faltinsen and Sortland 1987]. The authors showed the importance of bilge-keel depth, especially for low Keulegan-Carpenter numbers. [Sarpkaya, 1995] presented experimental results for two- and three-dimensional bilge keels subject to an oscillating flow. The authors conclude that bilge keel damping is affected by the vortex shedding from the edge of the bilge keel and the use of damping coefficients from flat plates in a free stream are not necessarily accurate for wall bounded bilge keels. [Yeung et al. 1998] applied the Free-Surface Random Vortex Method (FSRVM) to a rectangular ship-like section oscillating in roll motion. In [Yeung et al. 2000], the authors extended the work to include modeling of the complex flow around the bilge keels. In the FSRVM, the flow-field is solved by decomposing it into irrotational and vortical parts. The irrotational part is solved using a complex-valued boundary-integral method, utilizing Cauchy's integral theorem for a region bounded by the body, the free surface and the open boundary. The rotational part is solved by solving the vorticity equation using the fractional step method. Results obtained using the solver

14

are compared to experimental data as well as results obtained by [Alessandrini and Delhommeau 1995] for various bilge keel depths and forcing function amplitudes. Most recently, [Miller et al. 2002] demonstrated three-dimensional RANS calculations to simulate roll motions of a circular cylinder with bilge keels. The numerical results are compared with an experiment performed at the Circulating Water Channel at the Naval Surface Warfare Center, Carderock Division.

Other works in this area include [Sturova and Motygin 2002], where the authors solve, using a multipole expansion method, a system of boundary integral equations describing the linear two-dimensional water-wave problem, for a horizontal cylinder undergoing small oscillations at the interface of two layers of different densities.

In this thesis, an Euler solver, based on the finite volume method and using a collocated grid approach, is used to simulate the flow around a heaving or rolling rectangular FPSO hull located at the free surface. Results are compared with existing experimental data and results from other numerical techniques.

Chapter 3

Numerical Formulation

The detailed formulation for an unsteady, two-dimensional Euler solver is presented in this chapter. Extension of the solver to a laminar Navier-Stokes solver in two-dimensions involves inclusion of the viscous terms and this is discussed in Section 3.2. The formulation for a steady axisymmetric and 3D Euler solver is similar to the 2D unsteady formulation, except for the use of the artificial compressibility method to solve the steady problem. This is discussed in Section 3.3. Details of the axisymmetric and 3D formulation as applied to the propeller flow/vortical inflow interaction have been presented in [Choi 2000] and [Choi and Kinnas 2000b].

3.1 Unsteady, 2-D Euler Solver

Consider a two-dimensional (planar), unsteady and incompressible flow confined to the $x - y$ plane. The x-axis extends from left to right, along the lower boundary of the rectangular domain. The y-axis points vertically upward and is located such that the domain is symmetrical about it.

The flow is governed by the Euler equations, and these include the continuity equation and the x- and y-momentum equations. The vector form of the continuity and momentum equations for an inviscid fluid can be written as described in Equations 3.1 and 3.2.

$$\nabla \cdot \vec{\hat{v}} = 0 \tag{3.1}$$

$$\hat{\rho} \, \frac{\partial \vec{\hat{v}}}{\partial \hat{t}} + \hat{\rho} \, \nabla \cdot (\vec{\hat{v}}\vec{\hat{v}}) = -\nabla \hat{p} + \hat{\rho} \vec{\hat{f}} \tag{3.2}$$

where $\vec{\hat{v}}$ is the total velocity; $\hat{f}$ is the body force per unit mass; $\hat{\rho}$ is the density of the fluid; $\hat{p}$ is the pressure; and $\hat{t}$ is the time. In the above equations, the hat (ˆ) implies a dimensional variable.

The above dimensional equations are non-dimensionalized using the following reference variables:

- Length scale, L, which is a representative length in the problem being solved. For example, in the propeller flow problem, the variables are made non- dimensional by a reference length which is chosen as the propeller radius R.

- Velocity scale, U_∞, which is the flow velocity at infinity.

- Density scale, ρ_∞ is the density of the undisturbed fluid.

Combinations of these scales are used to non-dimensionalize the body force and pressure variables. The non-dimensionalization is summarized in Equation 3.3. Note that in Equation 3.3, $\hat{x}$ is dimensional while x is non-dimensional.

$$x = \frac{\hat{x}}{L}, \;\; y = \frac{\hat{y}}{L}, \;\;\;\; u = \frac{\hat{u}}{U_\infty}, \;\; v = \frac{\hat{v}}{U_\infty}, \;\;\;\; t = \frac{\hat{t}}{L/U_\infty},$$

$$p = \frac{\hat{p}}{\rho_\infty U_\infty^2}, \;\;\;\; f_x = \frac{\hat{f}_x}{U_\infty^2/L}, \;\;\; f_y = \frac{\hat{f}_y}{U_\infty^2/L}, \tag{3.3}$$

$\hat{f}_x$, $\hat{f}_y$: body force per unit mass.

17

Introducing the non-dimensional variables into Equations 3.1 and using the fact that for an incompressible flow $\hat{\rho} = \rho_\infty$, we get the non-dimensional differential form of the Euler equations. The Euler equations in the differential form (non-dimensionalized) are shown in Equation 3.4.

$$\frac{\partial \vec{U}}{\partial t} + \frac{\partial \vec{F}}{\partial x} + \frac{\partial \vec{G}}{\partial y} = \vec{Q} \tag{3.4}$$

where the column matrices $\vec{U}, \vec{F}, \vec{G}$, and $\vec{Q}$ are defined as:

$$\vec{U} = \begin{bmatrix} u \\ v \end{bmatrix}, \quad \vec{F} = \begin{bmatrix} u^2 \\ uv \end{bmatrix},$$

$$\vec{G} = \begin{bmatrix} uv \\ v^2 \end{bmatrix}, \quad \vec{Q} = \begin{bmatrix} -\partial p/\partial x + f_x \\ -\partial p/\partial y + f_y \end{bmatrix} \tag{3.5}$$

The derivative of the pressure is moved to the right hand side of the equation and is grouped in Q with the body force terms because the pressure correction method is adopted in the unsteady formulation.

3.1.1 Finite Volume Method

In the finite volume method, the fluid domain is discretized into quadrilateral cells or *volumes*. (*Note*: This is not necessary as the finite volume method is equally applicable to unstructured grids as well. However, the present solver has been developed for quadrilateral cells). The governing momentum equations, represented by Equation 3.4, are integrated over the volume of each cell of the domain. Applying the Gauss divergence theorem to convert all volume integrals to surface integrals, we obtain the following semi-discrete integral equation:

$$\frac{\partial \vec{U}}{\partial t} S_{ij} + \sum_{edges} \left(\vec{F} dy - \vec{G} dx \right) = \vec{Q} S_{ij} \tag{3.6}$$

18

where S_{ij} is the area of cell "ij", i and j are the indices in the x- and y-directions, respectively. For cell "C" (see Figure 3.1) , area of cell S_C is defined as:

$$S_C = \frac{1}{2} \begin{vmatrix} (x_3 - x_1) & (y_3 - y_1) \\ (x_2 - x_4) & (y_2 - y_4) \end{vmatrix} \tag{3.7}$$

In the formulation presented in this section the following notation is used:

- Each cell is represented by either a capital letter or by the indices of the lower left corner node. For example, in Figure 3.1, cell "C" can also be referred to as cell "ij".

- Each node is represented by a number or by the indices. For example, node "1" can also be referred to as node "i,j".

The residual term, defined below, needs to be determined on the edges of the cells.

$$R_{ij} \equiv \sum_{edges} \left(\vec{F} dy - \vec{G} dx \right) = \sum_{e=N,W,S,E} \left(\vec{F}_e \Delta y_e - \vec{G}_e \Delta x_e \right) \tag{3.8}$$

where F_e and G_e are taken as the average of the values of F and G at the nodes forming edge "e". Δx_e and Δy_e represent the difference in the x and y coordinates of the nodes forming edge "e".

The pressure gradients can be expressed in the numerical formulation as shown below:

$$\frac{\partial p}{\partial x} = \frac{1}{S_{ij}} \sum_{e=N,W,S,E} p_e \Delta y_e \tag{3.9}$$

19
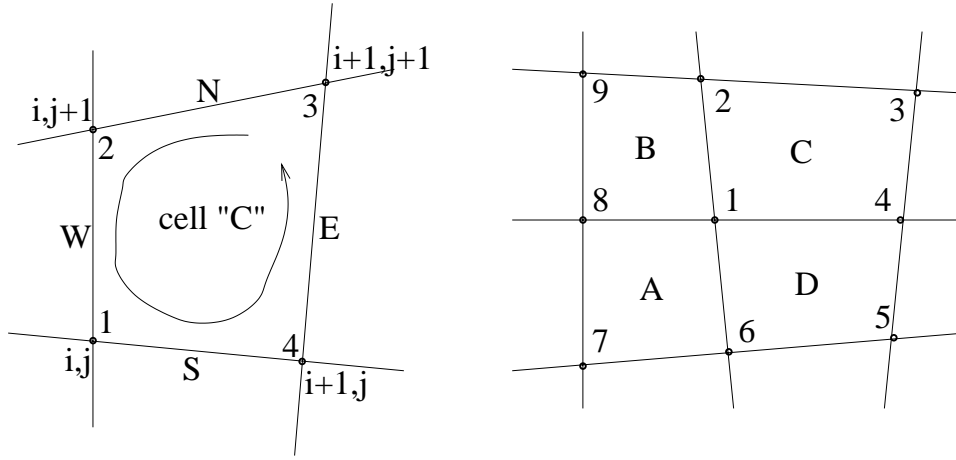
Figure 3.1: A quadrilateral FVM cell (left) and the cells influencing a given node (right) (Figure adjusted from [Kinnas 1999])

and

$$\frac{\partial p}{\partial y} = -\frac{1}{S_{ij}} \sum_{e=N,W,S,E} p_e \Delta x_e \qquad (3.10)$$

In the current scheme, the node based scheme for space is used *i.e.* u, v, p are computed and stored at the computational nodes. This provides the advantage that the boundary conditions can be applied directly at the nodes, without requiring any interpolation.

3.1.2 Ni's Lax-Wendroff Method for Time

A second-order, explicit method in time is used to march in time. At each computational node, the unknown $\vec{U}$ at time step 'n+1' can be expressed in terms of the known $\vec{U}$ at time step 'n' and the first and the second derivatives, computed at time step 'n', by using the Taylor series expansion (Equation 3.11).

20

$$\mathbf{U}_{i,j}^{n+1} \simeq \mathbf{U}_{i,j}^{n} + \left(\frac{\partial \mathbf{U}}{\partial t}\right)_{i,j}^{n} \Delta t + \left(\frac{\partial^2 \mathbf{U}}{\partial t^2}\right)_{i,j}^{n} \frac{(\Delta t)^2}{2} \qquad (3.11)$$

where Δt is the time step size, the superscript 'n' represents the value of the current time step and the subscript (i, j) refers to the node. In order to evaluate the $\vec{U}$ at time step 'n+1' $\left(\frac{\partial \mathbf{U}}{\partial t}\right)_{i,j}^{n}$ and $\left(\frac{\partial^2 \mathbf{U}}{\partial t^2}\right)_{i,j}^{n}$ are evaluated as shown in Equations 3.12 and 3.13.

$$
\begin{aligned}
\left(\frac{\partial \mathbf{U}}{\partial t}\right)_{i,j}^{n} &\simeq \frac{1}{4} \sum_{cells} \left(\frac{\partial \mathbf{U}}{\partial t}\right)_{cell}^{n} \\
&= \frac{1}{4} \sum_{c=A,B,C,D} \left(-\frac{\mathbf{R}_c^n}{S_c} + \mathbf{Q}_c^n\right) \qquad (3.12)
\end{aligned}
$$

Equation 3.12 implies that the value of $\left(\frac{\partial \mathbf{U}}{\partial t}\right)_{i,j}^{n}$ is the average of the four cells that share node (i, j). The second derivative can be computed by taking the derivative of Equation 3.12 with respect to time. This gives us:

$$
\begin{aligned}
\left(\frac{\partial^2 \mathbf{U}}{\partial t^2}\right)_{i,j}^{n} &\simeq \frac{1}{4} \sum_{c=A,B,C,D} \frac{\partial}{\partial t} \left(-\frac{\mathbf{R}_c^n}{S_c} + \mathbf{Q}_c^n\right) \\
&= \frac{1}{4\Delta t} \sum_{c=A,B,C,D} \left(-\frac{\Delta \mathbf{R}_c^n}{S_c} + \Delta \mathbf{Q}_c^n\right) \qquad (3.13)
\end{aligned}
$$

where $\Delta(\mathbf{R_c^n})$ and $\Delta(\mathbf{Q_c^n})$ are the changes in the values of $\mathbf{R_c^n}$ and $\mathbf{Q_c^n}$ between time steps 'n' and 'n-1'

The value of the variable at any node is influenced by four adjoining cells (see Figure 3.1) and the distribution formula shown below shows how the value of the variable at time step 'n+1' is determined from the value at the previous time step and the contributions of the adjoining cells.

$$\vec{U}_1^{n+1} = \vec{U}_1^n + (\delta\vec{U}_1)_A + (\delta\vec{U}_1)_B + (\delta\vec{U}_1)_C + (\delta\vec{U}_1)_D \qquad (3.14)$$

where, for example, the influence of cell "C" on node "1" can be expressed as:

$$(\delta\vec{U}_1)_C = \frac{1}{4}(\Delta\vec{U}_C - \Delta f_C - \Delta g_C) \qquad (3.15)$$

where,

$$\Delta\vec{U}_C = -\frac{\Delta t}{S_{ij}}R_{ij} + \Delta t Q_{ij} \qquad (3.16)$$

$$\Delta f_C = \frac{\Delta t}{S_{ij}}(\Delta F_C \Delta y^l - \Delta G_C \Delta x^l) \qquad (3.17)$$

$$\Delta g_C = \frac{\Delta t}{S_{ij}}(\Delta G_C \Delta x^m - \Delta F_C \Delta y^m) \qquad (3.18)$$

In the above equations, R_{ij} is defined according to Equation 3.8 and Q_{ij} represents the body force term over cell ij (assumed constant over cell area).

$$\Delta F_C = \begin{bmatrix} 2u\Delta u \\ \Delta uv + u\Delta v \end{bmatrix} \qquad (3.19)$$

$$\Delta G_C = \begin{bmatrix} \Delta uv + u\Delta v \\ 2v\Delta v \end{bmatrix} \qquad (3.20)$$

where Δu and Δv represent the average change in the variables u and v for a given cell *i.e.* the average of the variable values at the four nodes forming the cell.

22

The artificial dissipation (or viscosity) is applied to improve the stability of the numerical method [Anderson 1995]. The second and fourth order dissipations, respectively μ_2 and μ_4, are scaled by Δt and added to Equation (3.14).

$$\mathbf{U}_1^{n+1} = \mathbf{U}_1^n + \sum_{c=A,B,C,D} (\delta \mathbf{U}_1)_c^n + \Delta t \left(\mu_2 - \mu_4\right) \qquad (3.21)$$

with

$$\mu_2 = \sigma_2 \left(\delta_{ii}\mathbf{U}_1^n + \delta_{jj}\mathbf{U}_1^n\right) \qquad (3.22)$$

$$\mu_4 = \sigma_4 \left(\delta_{iiii}\mathbf{U}_1^n + \delta_{jjjj}\mathbf{U}_1^n\right) \qquad (3.23)$$

where, the artificial dissipation coefficients, σ_2 and σ_4, are user specified constant parameters that control the amount of the dissipation.

The finite central difference operators, δ_{ii} and δ_{iiii}, for example, are defined as follows (for a constant j).

$$\delta_{ii} = (\ )_{i-1} - 2(\ )_i + (\ )_{i+1} \qquad (3.24)$$

$$\delta_{iiii} = (\ )_{i-2} - 4(\ )_{i-1} + 6(\ )_i - 4(\ )_{i+1} + (\ )_{i+2} \qquad (3.25)$$

Note that the artificial dissipation coefficients should be adjusted appropriately according to the grid resolution because the finite differences, given by Equations (3.24) and (3.25), depend on the cell size. For most of cases, the second order dissipation coefficient, σ_2, is set equal to zero, and the fourth order artificial dissipation coefficient, σ_4, is determined for each case by trial and error so that it has the smallest value for which the Euler solver converges.

For the numerical scheme, a convergence criteria needs to be specified in order to stop the computation when the desired degree of accuracy is achieved. In

the current scheme convergence is achieved by requiring the following equations to be satisfied.

$$\max_{i,j}(|\Delta p|) < \epsilon, \tag{3.26}$$

$$\max_{i,j}(|\Delta u|) < \epsilon, \tag{3.27}$$

$$\max_{i,j}(|\Delta v|) < \epsilon \tag{3.28}$$

$$\left(\text{e.g. } \epsilon = 10^{-6}\right) \tag{3.29}$$

where $|\Delta u|$, $|\Delta v|$, and $|\Delta p|$ are the changes in the values of the variables from one time step to another, for all nodes in the domain.

3.1.3   Pressure Correction Method for Continuity Equation

As there is no independent equation to determine the pressure, the pressure correction method or the SIMPLE (Semi-Implicit Method for Pressure Linked Equations) method [Patankar 1980; Rhie and Chow 1983] is used in order to solve for the pressure. This method is based on the fact that the velocity components should satisfy the continuity equation at all times. Therefore, the new pressure is determined by applying a 'correction' to the pressure at the previous time step and this 'new' pressure is such that the corresponding velocity components satisfy the continuity equation. The idea of SIMPLE method is followed, but *the collocation scheme in which all variables are defined and stored at nodes* is kept.

The intermediate velocity field (denoted with the superscript *) is determined at an intermediate time step using an intermediate (or guessed at first) pressure field, p^*. Since the method is iterative, to find the correct (within a given tolerance) velocity and pressure fields for time step '$n + 1$', the intermediate fields are updated

24

repeatedly. Thus, the intermediate velocity and pressure are not marked with the time step index, understanding that they are between the time steps $'n'$ and $'n+1'$.

$$\mathbf{U}^*_{i,j} = \mathbf{U}^n_{i,j} + \sum_{c=A,B,C,D} (\delta \mathbf{U}_{i,j})^*_c + \Delta t \left(\mu^*_2 - \mu^*_4 \right) \tag{3.30}$$

In Equation 3.30, $(\delta U_{i,j})^*_c$ is determined by an equation similar to Equation 3.15, but by using the intermediate pressure field, p^*. Also, the artificial dissipations, μ^*_2 and μ^*_4 are evaluated based on the intermediate velocity field, U^*.

The pressure and corresponding velocity corrections (represented by prime $'$) are determined using the Poisson equation and are defined as follows:

$$p^{n+1}_{i,j} = p^n_{i,j} + p'_{i,j} \tag{3.31}$$

$$\mathbf{U}^{n+1}_{i,j} = \mathbf{U}^*_{i,j} + \mathbf{U}'_{i,j} \tag{3.32}$$

where $p'_{i,j}$ and $\mathbf{U}'_{i,j}$ are the corrections to the pressure and the velocity fields, respectively.

From the definition of the velocity correction given by Equation (3.32), the expression for $U'_{i,j}$ can be obtained by subtracting $\mathbf{U}^*_{i,j}$ of Equation (3.30) from $\mathbf{U}^{n+1}_{i,j}$ of Equation (3.14) as shown next.

$$\mathbf{U}'_{i,j} \equiv \mathbf{U}^{n+1}_{i,j} - \mathbf{U}^*_{i,j}$$

$$= \sum_{c=A,B,C,D} (\delta \mathbf{U}_{i,j})'_c + \Delta t \left(\mu^n_2 - \mu^*_2 - \mu^n_4 + \mu^*_4 \right) \tag{3.33}$$

where, $(\delta \mathbf{U}_{i,j})'_c$ is defined as $(\delta \mathbf{U}_{i,j})^n_c - (\delta \mathbf{U}_{i,j})^*_c$.

As is done in the SIMPLE method, only the terms which include the pressure gradient are assumed to be non-zero in Equation (3.33). That is,

$$\mathbf{U}'_{i,j} = \frac{\Delta t}{4} \sum_{c=A,B,C,D} \left[\begin{array}{c} -\partial p'/\partial x \\ -\partial p'/\partial y \end{array} \right]. \tag{3.34}$$

The pressure correction $p'_{i,j}$ is found by solving the pressure correction Equation (3.35). The following pressure correction equation for p'_1 can be derived from the continuity over the block of volume around the node "1", with the substitution of the velocity correction expressed as the pressure weighted interpolation. (*Note: In the next equation, node numbers are used instead of the indices*)

For node "1", we have:

$$g_1 p'_1 + g_2 p'_2 + g_4 p'_4 + g_6 p'_6 + g_8 p'_8 = g_o \tag{3.35}$$

The terms in the above equation are defined below:

$$g_o = \frac{Q_M}{\alpha \Delta t} \tag{3.36}$$

where Q_M is the residual of the continuity equation, α is the velocity under-relaxation factor and Δt is the time step.

$$g_2 = -\frac{\xi_2}{J} \Delta y_N - \frac{\xi_1}{J} \Delta x_N \tag{3.37}$$

$$g_4 = \frac{\eta_2}{J} \Delta y_E + \frac{\eta_1}{J} \Delta x_E \tag{3.38}$$

26

$$g_6 = \frac{\xi_2}{J}\Delta y_S + \frac{\xi_1}{J}\Delta x_S \tag{3.39}$$

$$g_8 = -\frac{\eta_2}{J}\Delta y_W - \frac{\eta_1}{J}\Delta x_W \tag{3.40}$$

$$g_1 = -g_2 - g_4 - g_6 - g_8 \tag{3.41}$$

with the subscripts N, S, E, W are defined as in Figure 3.1 and J, ξ_1, η_1 etc. defined in Equations 3.50 and 3.51.

The pressure correction equation is solved iteratively, as shown in Equation 3.42, using the following explicit expression for p_1' with the under-relaxation, α_{pp}.

$$\begin{aligned} (p_1')_{new} &= (1 - \alpha_{pp}) \cdot (p_1')_{old} \\ &+ \alpha_{pp} \cdot \frac{1}{g_1}\Big\{g_o - (g_2 p_2' + g_4 p_4' + g_6 p_6' + g_8 p_8')\Big\} \end{aligned} \tag{3.42}$$

The $\mathbf{U}_{i,j}^{n+1}$ determined according to Equation 3.32 satisfies the continuity equation.

Sequence of Operations (SIMPLE)

The following operations are performed at each time step:

1. Guess the pressure field p^*.

2. Solve the momentum equation by Equation (3.30), to obtain intermediate velocities u^*, v^*.

3. Solve pressure correction equation, Equation (3.35) for p'.

4. Calculate (correct) pressure p and velocities u, v by Equation.(3.43).

$$p = p^* + p', \quad u = u^* + u', \quad v = v^* + v' \tag{3.43}$$

5. Treat the corrected pressure p as a new guessed pressure p^*, return to step 2, and repeat until either Q_M is small enough or a prescribed number of iterations is reached.

For each time step, the following convergence criterion is checked:

$$\max_{all\ cells} (|Q_M|) < \varepsilon \tag{3.44}$$

Q_M = residual of the continuity equation

3.2   Unsteady, 2-D Navier-Stokes Solver

The formulation for the 2-D Navier-Stokes solver is similar to that of the 2-D Euler solver, except for the additional viscous terms that enter the equations. The dimensional vector form of the Navier-Stokes equations can be written as described below:

$$\nabla \cdot \vec{\tilde{v}} = 0 \tag{3.45}$$

$$\rho \frac{\partial \vec{\tilde{v}}}{\partial \hat{t}} + \rho \nabla \cdot (\vec{\tilde{v}}\vec{\tilde{v}}) = -\nabla \hat{p} + \rho \vec{\hat{f}} + \mu \nabla^2 \vec{\tilde{v}} \tag{3.46}$$

where μ is the coefficient of dynamic viscosity.

Non-dimensionalizing the above equation, using the reference parameters as described in Equation 3.3, we obtain an equation similar to Equation 3.4, but with the column matrices $\vec{U}, \vec{F}, \vec{G}$, and $\vec{Q}$ redefined as:

28

$$
\vec{U} = \begin{bmatrix} u \\ v \end{bmatrix}, \quad \vec{F} = \begin{bmatrix} u^2 - \frac{2}{Re} \frac{\partial u}{\partial x} \\ uv - \frac{1}{Re} \left(\frac{\partial u}{\partial y} + \frac{\partial v}{\partial x} \right) \end{bmatrix},
$$

$$
\vec{G} = \begin{bmatrix} uv - \frac{1}{Re} \left(\frac{\partial u}{\partial y} + \frac{\partial v}{\partial x} \right) \\ v^2 - \frac{2}{Re} \frac{\partial v}{\partial y} \end{bmatrix}, \quad \vec{Q} = \begin{bmatrix} -\frac{\partial p}{\partial x} + f_x \\ -\frac{\partial p}{\partial y} + f_y \end{bmatrix} \tag{3.47}
$$

where Re is the Reynolds number for the flow, defined as $Re = \frac{\rho U_\infty L}{\mu}$.

The terms $\dfrac{\partial u}{\partial x}, \dfrac{\partial u}{\partial y}, \dfrac{\partial v}{\partial x}$, and $\dfrac{\partial v}{\partial y}$ in $\vec{F}$ and $\vec{G}$ (Equation 3.47) need to be calculated at each node. In order to do this, viscous stresses are first computed in the grid coordinate (ξ, η), and transformed to (x, y)-system by using tensor transformation.

$$
\left\{ \begin{array}{c} \left(\dfrac{\partial u}{\partial x} \right) \\ \left(\dfrac{\partial u}{\partial y} \right) \end{array} \right\} = \frac{1}{J} \begin{bmatrix} \eta_2 & -\xi_2 \\ -\eta_1 & \xi_1 \end{bmatrix} \left\{ \begin{array}{c} \left(\dfrac{\partial u}{\partial \xi} \right) \\ \left(\dfrac{\partial u}{\partial \eta} \right) \end{array} \right\} \tag{3.48}
$$

$$
\left\{ \begin{array}{c} \left(\dfrac{\partial v}{\partial x} \right) \\ \left(\dfrac{\partial v}{\partial y} \right) \end{array} \right\} = \frac{1}{J} \begin{bmatrix} \eta_2 & -\xi_2 \\ -\eta_1 & \xi_1 \end{bmatrix} \left\{ \begin{array}{c} \left(\dfrac{\partial v}{\partial \xi} \right) \\ \left(\dfrac{\partial v}{\partial \eta} \right) \end{array} \right\} \tag{3.49}
$$

$$
J = \xi_1 \eta_2 - \xi_2 \eta_1 \tag{3.50}
$$

$$
\xi_1 = x_{i+1,j} - x_{i-1,j}, \quad \eta_1 = x_{i,j+1} - x_{i,j-1}
$$

$$
\xi_2 = y_{i+1,j} - y_{i-1,j}, \quad \eta_2 = y_{i,j+1} - y_{i,j-1} \tag{3.51}
$$

The remaining formulation is developed as described for the Euler solver, with the terms modified appropriately to include the viscous effects. For example, the terms ΔF_C and ΔG_C in Equation 3.16 now become:

$$\Delta F_C = \left[\begin{array}{c} 2u\Delta u + \Delta p \\ \Delta uv + u\Delta v \end{array} \right] - \frac{1}{Re} \left[\begin{array}{c} 2\Delta(\partial u/\partial x) \\ \Delta(\partial u/\partial y) + \Delta(\partial v/\partial x) \end{array} \right] \qquad (3.52)$$

$$\Delta G_C = \left[\begin{array}{c} \Delta uv + u\Delta v \\ 2v\Delta v + \Delta p \end{array} \right] - \frac{1}{Re} \left[\begin{array}{c} \Delta(\partial u/\partial y) + \Delta(\partial v/\partial x) \\ 2\Delta(\partial v/\partial y) \end{array} \right] \qquad (3.53)$$

3.3   Steady Euler Solver

The steady Euler solver is used to solve the propeller flow problem. The axisymmetric and the 3-D formulations are presented in the next two sections. Numerical details can be found in [Choi 2000] and [Choi and Kinnas 2001]. While the axisymmetric version has been used for the stator-rotor problem, the 3-D version has been used for the non-axisymmetric podded propulsor as well as to model cavitation on the rotor blade in the presence of the stator modified non-axisymmetric wake.

The Euler equations are discretized using the finite volume method. As these equations are steady, the artificial compressibility method [Chorin 1967] is adopted. Apart from the use of the artificial compressibility method the same numerical methods, as have been discussed for the 2-D unsteady Euler solver, are used for the axisymmetric and 3-D solvers.

A ship-fixed coordinate system, as shown in Figure 3.2, is used for the steady axisymmetric and 3-D formulations . The origin of the coordinate system is at the center of the propeller disk, with the x-axis pointing downstream along the propeller shaft axis. A Cartesian coordinate system is used for the three-dimensional formulation, while a cylindrical coordinate system is used in the axisymmetric formulation. In the Cartesian coordinate system, the positive y points vertically upward, and the
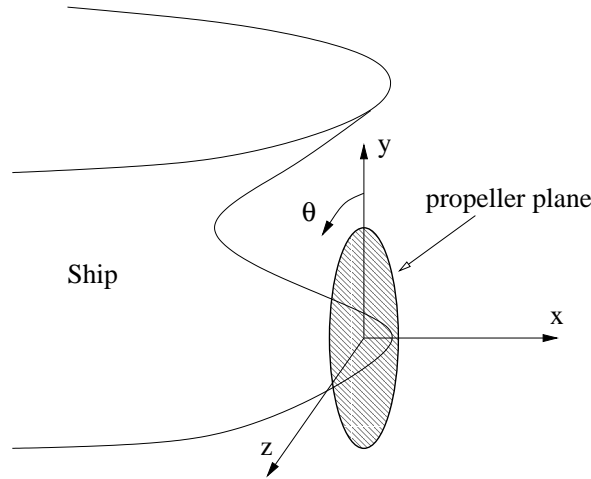
Figure 3.2: Ship-fixed Cartesian coordinate system (taken from [Choi 2000])

positive z axis towards the port side (left) of the ship. In a cylindrical system, the positive r is outward, and the angle θ is measured around the x-axis starting from the top (y-axis), as shown in Figure 3.2.

3.3.1 Axisymmetric Steady Euler Solver

The axisymmetric Euler solver is used to solve for flow around axisymmetric hull appendages and also in preliminary propeller design under axisymmetric (circumferentially averaged) inflow. The most advantageous characteristic of the axisymmetric Euler solver is that it takes less time to run than the three-dimensional solver.

The dimensionless governing equations can be written in the cylindrical coordinate system (x, r, θ) with the corresponding velocity components (u_x, u_r, u_θ). In cylindrical coordinate system, the steady Euler equations can be written as follows:

$$\frac{\partial \mathbf{F}}{\partial x} + \frac{\partial \mathbf{G}}{\partial r} + \frac{\partial \mathbf{H}}{\partial \theta} = \mathbf{Q} \tag{3.54}$$

In equation (3.54), the column matrices $\mathbf{F}$, $\mathbf{G}$, $\mathbf{H}$, and $\mathbf{Q}$ are defined as fol-

31

lows:

$$
\mathbf{F} = \begin{bmatrix} ru_x \\ r(u_x^2 + p) \\ ru_x u_r \\ ru_x u_\theta \end{bmatrix}, \quad \mathbf{G} = \begin{bmatrix} ru_r \\ ru_x u_r \\ r(u_r^2 + p) \\ ru_r u_\theta \end{bmatrix},
$$

$$
\mathbf{H} = \begin{bmatrix} u_\theta \\ u_x u_\theta \\ u_r u_\theta \\ u_\theta^2 + p \end{bmatrix}, \quad \mathbf{Q} = \begin{bmatrix} 0 \\ rf_x \\ (u_\theta^2 + p) + rf_r \\ -u_r u_\theta + rf_\theta \end{bmatrix} \tag{3.55}
$$

For the axisymmetric flow, the following assumption is also made. This implies axisymmetry *i.e.* **H** does not vary in the circumferential direction.

$$
\frac{\partial \mathbf{H}}{\partial \theta} = 0 \tag{3.56}
$$

For the steady Euler solver, the pressure correction approach cannot be used. Instead, the artificial compressibility method [Chorin 1967] is adopted. In the artificial compressibility method, the following pseudo-unsteady terms are added to the left hand side of the steady incompressible Euler equation (3.54). Now these equations resemble the unsteady compressible Euler equations and can be solved similarly.

$$
\frac{\partial \mathbf{U}}{\partial t^*} \equiv \frac{\partial}{\partial t^*} \begin{bmatrix} r\tilde{\rho} \\ ru_x \\ ru_r \\ ru_\theta \end{bmatrix} \tag{3.57}
$$

It should be noted that the use of pseudo time does not allow us to use the method to solve for unsteady problems. t^* is a pseudo-time and should be regarded just as an iteration parameter.

32

Following Chorin [Chorin 1967], the artificial density, $\tilde{\rho}$, is related to the pressure, p, through the following artificial equation of state.

$$p = \frac{\tilde{\rho}}{\beta} \tag{3.58}$$

In equation (3.58), β is the artificial compressibility factor which is a controllable constant. The solution does not depend on the value of the artificial compressibility factor, β, which is analogous to a relaxation parameter. The method requires that the artificial Mach number,

$$M = \frac{\sqrt{u_x^2 + u_r^2 + u_\theta^2}}{c}, \tag{3.59}$$

is less than 1.0, where the artificial speed of sound is defined as

$$c = \frac{1}{\sqrt{\beta}}. \tag{3.60}$$

The addition of the pseudo-unsteady terms (3.57) to the steady incompressible Euler equation (3.54), with the use of equation (3.56), brings the axisymmetric governing equations to the following form.

$$\frac{\partial \mathbf{U}}{\partial t^*} + \frac{\partial \mathbf{F}}{\partial x} + \frac{\partial \mathbf{G}}{\partial r} = \mathbf{Q} \tag{3.61}$$

with

$$\mathbf{U} = \begin{bmatrix} rp \\ ru_x \\ ru_r \\ ru_\theta \end{bmatrix}, \quad \mathbf{F} = \begin{bmatrix} ru_x/\beta \\ r(u_x^2 + p) \\ ru_x u_r \\ ru_x u_\theta \end{bmatrix}, \quad \mathbf{G} = \begin{bmatrix} ru_r/\beta \\ ru_x u_r \\ r(u_r^2 + p) \\ ru_r u_\theta \end{bmatrix}, \tag{3.62}$$

$$\mathbf{Q} = \begin{bmatrix} 0 \\ rf_x \\ (u_\theta^2 + p) + rf_r \\ -u_r u_\theta + rf_\theta \end{bmatrix}$$

33

As the boundary conditions and body forces are steady, the solution converges to the steady state in the limit $t^* \rightarrow \infty$. When steady state is reached, the pseudo-unsteady term, $\partial \mathbf{U}/\partial t^*$, becomes zero, and equations (3.61) and (3.62) are equivalent to those of the incompressible flow. In this way, the artificial compressibility method guarantees that the steady incompressible solution is obtained at the end (i.e. at large pseudo-times).

The formulation of the finite volume method for equation (3.61) is similar to that for a two-dimensional planar problem since the meridional coordinate system (x, r) can be regarded as a two-dimensional coordinate system (x, y). The details of the numerical implementation of the two-dimensional Euler equations (3.61) have already been discussed in detail in Section 3.1.

3.3.2 Three-dimensional Steady Euler Solver

The method of artificial compressibility [Chorin 1967] is applied again in the three-dimensional steady Euler solver.

The dimensionless governing equations can be written in the following three-dimensional Cartesian form using non-dimensional variables.

$$\frac{\partial \mathbf{U}}{\partial t^*} + \frac{\partial \mathbf{F}}{\partial x} + \frac{\partial \mathbf{G}}{\partial y} + \frac{\partial \mathbf{H}}{\partial z} = \mathbf{Q} \qquad (3.63)$$

The terms $\mathbf{U}$, $\mathbf{F}$, $\mathbf{G}$, $\mathbf{H}$, and $\mathbf{Q}$ are defined as follows.

$$\mathbf{U} = \begin{bmatrix} p \\ u \\ v \\ w \end{bmatrix}, \ \mathbf{F} = \begin{bmatrix} u/\beta \\ u^2 + p \\ uv \\ uw \end{bmatrix}, \ \mathbf{G} = \begin{bmatrix} v/\beta \\ uv \\ v^2 + p \\ vw \end{bmatrix}, \ \mathbf{H} = \begin{bmatrix} w/\beta \\ uw \\ vw \\ w^2 + p \end{bmatrix}, \ \mathbf{Q} = \begin{bmatrix} 0 \\ f_x \\ f_y \\ f_z \end{bmatrix}$$

34
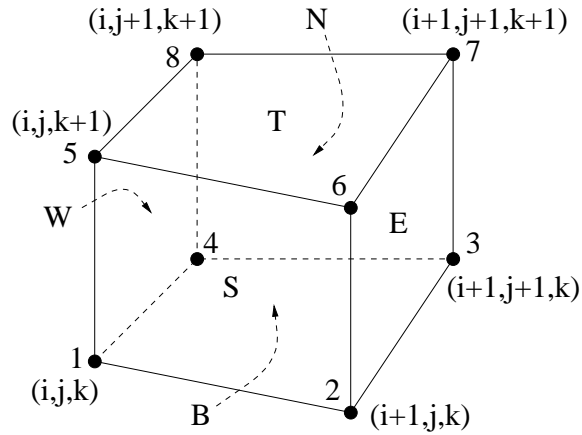
Figure 3.3: Cell (i, j, k) on which the finite volume method is applied (taken from [Choi 2000])

When steady state is reached, the first term in equation (3.63) vanishes and the incompressible steady flow solution is obtained.

For the finite volume formulation, the Euler equations (3.63) are integrated over a cell of volume $\mathcal{V}$, such as the one shown in Figure 3.3. The formulation is similar to the 2-D solver formulation, but a lot more involved.

The time step size is determined so that the Courant Friedrichs Lewy (CFL) condition [Courant et al. 1967] is satisfied.

$$\Delta t < \min_{i,j,k} \left\{ \min \left(\frac{\Delta x}{u}, \frac{\Delta y}{v}, \frac{\Delta z}{w} \right) \right\} \tag{3.64}$$

The iteration in time is continued until the maximum change of variables is less than a certain specified tolerance (for example $\epsilon = 10^{-6}$).

3.4 Vortex Lattice Method for Propeller Potential flow

The present section presents a broad overview of the vortex lattice method. The complete formulation of the potential flow solver and the vortex lattice method may be found in chapter 6 of Ohkusu [Ohkusu 1996]. The *vortex lattice method* which solves numerically for the unsteady potential flow field around a cavitating propeller has been used successfully since the method was first developed by Kerwin and Lee [Kerwin and Lee 1978], Lee [Lee 1979] and Breslin et. al. [Breslin et al. 1982]. This method is classified as a lifting surface method because the singularities (vortices and sources) are distributed on the blade mean camber surface, as opposed to the other class of methods, the surface panel methods, in which the singularities are distributed on both sides of the blade surface.

In the vortex lattice method, a special arrangement of line vortex and source lattice is placed on the blade mean camber surface and its trailing wake surface. The three effects being modeled by these singularities are (a) a vortex lattice on the blade mean camber surface and the trailing wake surface to represent the blade loading and the trailing vorticity in the wake, (b) a source lattice on the blade mean camber surface to represent the blade thickness, and (c) a source lattice throughout the predicted sheet cavity domain to represent the cavity thickness.

The unknown strengths of the singularities are determined so that the kinematic and the dynamic boundary conditions are satisfied at the control points on the blade mean camber surface. The kinematic boundary condition requires that the flow velocity is tangent to the mean camber surface, and is applied at all control points. On the other hand, the dynamic boundary condition requires that the pressure on the cavitating part of the blade mean camber surface is equal to the vapor pressure, and is applied only at the control points that are in the cavitating region. One of the

complexities in the analysis of the cavitating propeller is that the extent of cavitation changes continuously as the blade rotates, and thus the domain in which the dynamic boundary condition is satisfied must be determined in an iterative way.

Chapter 4

The Stator-Rotor and Podded Propulsor

4.1 The Coupled Solver

In this chapter, the coupled vortex lattice method and Euler solver approach is discussed. Details can be found in, [Choi 2000] and [Choi and Kinnas 2000b]. Next, the application of the above method to the stator-rotor and podded propulsor system is presented. The purpose of using this approach is to determine the effective wake (modified due to the presence of the other component or the strut in the case of the podded propulsor) and evaluate the performance of each component under this modified inflow.

4.1.1 Decomposition of the Flow Field

The total unsteady flow field around a propeller is a function of both space and time. This flow field can be decomposed into two parts; one rotational and one irrotational component:

$$\vec{q}_t(\vec{x}, t) = \vec{q}_r(\vec{x}, t) + \vec{q}_i(\vec{x}, t) \tag{4.1}$$

where, the subscripts "t", "r" and "i" stand for total, rotational and irrotational, respectively.

38

In the present method, the *propeller induced velocity* field, $\vec{q}_p$, is used in place of the irrotational velocity field, $\vec{q}_i$. From potential flow theory, the propeller induced velocity, $\vec{q}_p$, can be expressed in terms of the perturbation potential, ϕ_p, by the following relation [Choi 2000].

$$\vec{q}_p(\vec{x}, t) = \nabla \phi_p(\vec{x}, t) \tag{4.2}$$

The vortex lattice method (VLM) is used to solve for this perturbation potential on the propeller as shown on the left side of Figure 4.1.

The perturbation potential as defined by equation (4.2) with respect to a coordinate system which rotates with the blade at a constant angular velocity, $\vec{\Omega}$, should satisfy the Laplace equation,

$$\nabla^2 \phi_p = 0. \tag{4.3}$$

The *Kinematic Boundary Condition* (KBC) applied on the blade mean camber surface results in the following equation [Choi 2000]:

$$\frac{\partial \phi_p}{\partial n} = - \left(\vec{q}_e + \vec{\Omega} \times \vec{x} \right) \cdot \vec{n} \tag{4.4}$$

where, $\vec{n}$ is the unit vector normal to the mean camber surface, and $\vec{q}_e$ is the effective wake as defined in the next paragraph. In addition, a Kutta condition must be applied at the trailing edge of the blades with the assumed trailing wake geometry.

Then, the rotational part, $\vec{q}_r$, can be obtained by subtracting this irrotational field, $\vec{q}_p$, from the total velocity field, $\vec{q}_t$. The rotational part determined in this way is defined as the effective wake velocity or, simply, the effective wake. The word

39
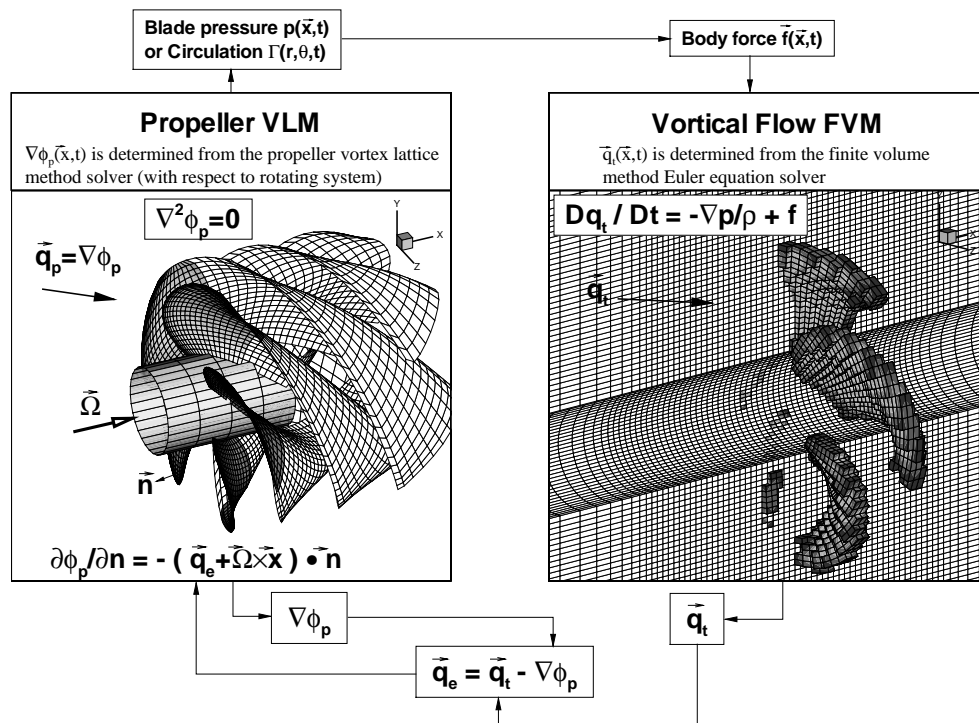
Figure 4.1: Interaction between the potential flow vortex lattice method (VLM) and the finite volume method (FVM) based Euler solver (taken from [Choi and Kinnas 2000b])

"wake" comes into the name because the propeller inflow is also the ship's wake. The effective wake, $\vec{q}_e$, is thus given as follows:

$$
\begin{aligned}
\vec{q}_e(\vec{x}, t) &\equiv \vec{q}_t(\vec{x}, t) - \vec{q}_p(\vec{x}, t) \\
&= \vec{q}_t(\vec{x}, t) - \nabla \phi_p(\vec{x}, t)
\end{aligned}
\tag{4.5}
$$

The effective wake, $\vec{q}_e$, is used as the inflow, when solving for the propeller perturbation potential, ϕ_p. The total velocity, $\vec{q}_t$, is evaluated from the Euler solver, as described in the next paragraphs. Once the potential ϕ_p is found, two things can be calculated; (a) the pressure on the propeller blade surface as a function of space and time, and (b) the propeller induced velocity $\vec{q}_p$, or equivalently $\nabla \phi_p$. The propeller blade pressure is needed to determine the body force distribution in the Euler solver, and the propeller induced velocity is needed when the effective wake is calculated. If unsteady sheet cavitation exists on the blade, then the extent and the thickness of the cavities are also determined as part of the solution. On the other hand, the global flow field is rotational and is solved by the finite volume method Euler solver, as shown on the right side of Figure 4.1.

The propeller loading obtained from the VLM is converted into the body force $\vec{f}$, and this body force is distributed over the cells corresponding to the blade location.

When the Euler equations,

$$
\frac{D\vec{q}_t}{Dt} = -\frac{\nabla p}{\rho} + \vec{f},
\tag{4.6}
$$

are solved, the total velocity $\vec{q}_t$ is obtained. The effective wake can then be computed by equation (4.5) using the propeller induced velocity, $\vec{q}_p$, already known from the

41
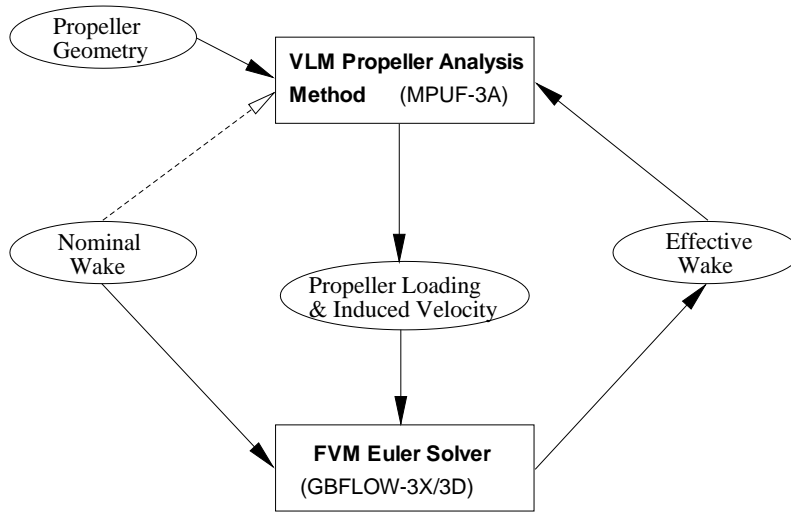
Figure 4.2: Flow chart showing the overall iterative process to compute the effective wake (the dashed arrow implies that the nominal wake is used as the propeller inflow only in the initial iteration) (taken from [Choi 2000])

propeller VLM. The overall process is iterative, between the potential flow solution of the propeller and the Euler equation solution of the global flow field, as shown in Figure 4.1.

4.1.2 Iterative Process to Compute the Effective Wake

Since the effective wake and the propeller loading depend on each other, the overall process must be iterative. The two components in the iterative process are the propeller solver (MPUF-3A) and the Euler equation solver (GBFLOW-3X/3D) as shown in Figure 4.2. The iterative process can start with the propeller analysis using the nominal wake as inflow. Using the computed propeller loading, the body force representing the propeller in the Euler equations can be calculated. The Euler solver computes the total velocity field using the body force found earlier. The effective wake can then be computed by subtracting the propeller induced velocity from the

42

total velocity field. Finally, the VLM solver uses the effective wake as the inflow to compute the updated propeller loading. The iterative process continues until convergence is reached. It has been found that the iterative process usually converges within three to five iterations depending on the convergence criterion specified (see Section 4.2.2).

4.1.3 Propeller Induced Velocity

Since the total velocity field is obtained as a solution of the Euler equations, the propeller induced velocity field should be known first to compute the effective wake by equation (4.5). The propeller induced velocity is computed by an indirect two step method. After the propeller solution is obtained, the propeller induced potential is computed at a vertical plane just upstream of the propeller. The location of the vertical plane should be chosen so that the plane is not too close to the singularities distributed over the propeller blade so that the local discretization errors are minimized. Usually this plane is located one panel size away from the blade. The plane also should not be too far from the propeller, because there could be some variation in the predicted effective wake between this plane and the propeller plane. Once the induced potentials are determined at all points located on the plane, the three components of the induced velocity vector can then be computed by numerically differentiating the induced potentials.

4.1.4 Propeller Body Force

In order to obtain the body force distribution on the finite volume cells which correspond to the location of the blade, the pressure difference across the blade surface, Δp, is integrated over the area of the lifting surface intersected by the finite volume
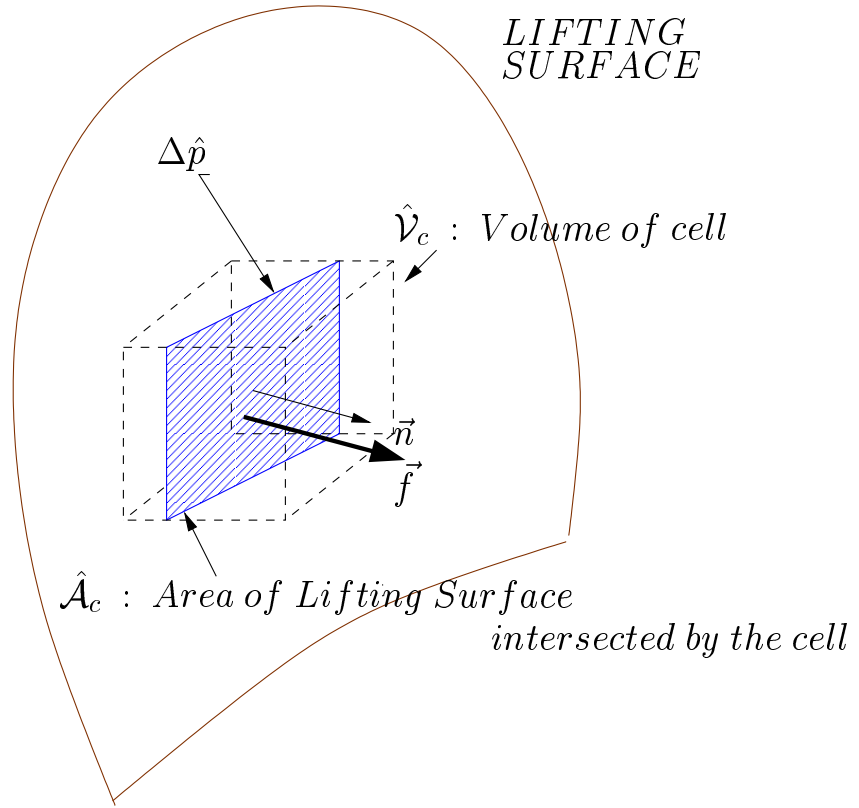
Figure 4.3: Body force determination in the Euler solver

cell, as shown in Figure 4.3.

The three-dimensional body force-pressure relation can be written in *dimensional* terms as follows.

$$\hat{\mathcal{V}}_c \hat{\rho} \vec{\hat{f}} = \Delta \hat{p} \hat{A}_c \vec{n} \tag{4.7}$$

where $\hat{\mathcal{V}}_c$ is the cell volume; $\Delta \hat{p}$ is the pressure difference across the blade surface (evaluated in MPUF-3A); $\hat{A}_c$ is the area of the mean camber surface contained in the cell; and $\vec{n}$ is the normal vector to the mean camber surface. To obtain the

44

corresponding expression for the axisymmetric body force, the cell volume, $\mathcal{V}_c$, in Equation 4.7 must be changed to the volume of the ring that is created by rotating the area of the side of the cell along the meridian plane, $\mathcal{A}_{cell}$, about the shaft axis. Thus, the corresponding dimensionless relation becomes as follows.

$$\left(\frac{2\pi\hat{r}\hat{\mathcal{A}}_{cell}}{R\ R^2}\right)\left(\frac{\vec{\hat{f}}}{U_\infty^2/R}\right)\left(\frac{U_\infty^2}{4n^2D^2}\right) = \left(\frac{\Delta\hat{p}\hat{A}_c\vec{n}}{\hat{\rho}n^2D^4}\right) \tag{4.8}$$

$$\text{or}$$

$$2\pi r\mathcal{A}_{cell} \qquad \vec{f} \qquad \frac{J_s^2}{4} \qquad = \qquad \vec{F}_P \tag{4.9}$$

where, the dimensionless pressure force $\vec{F}_P$ can be obtained from the propeller potential flow solver (MPUF-3A), $\hat{r}$ is the radius of the centroid of the cell, R and D are the propeller radius and diameter, J_s is the advance ratio based on ship speed, and n is the rotational frequency of the propeller.

As a result, the dimensionless *axisymmetric* body force can be evaluated using the following formula:

$$\vec{f} = \left(\frac{2}{\pi r\mathcal{A}_{cell}J_s^2}\right)\vec{F}_P \tag{4.10}$$

4.1.5   Method for Handling Two Components

For multi-component propulsors it is essential that the solver capture the interaction between the various components. The above described method can be easily extended for two- or more component propulsors.

A schematic diagram for the axial velocity distribution along the shaft axis is shown in Figure 4.4. The propulsion system consists of two components, which
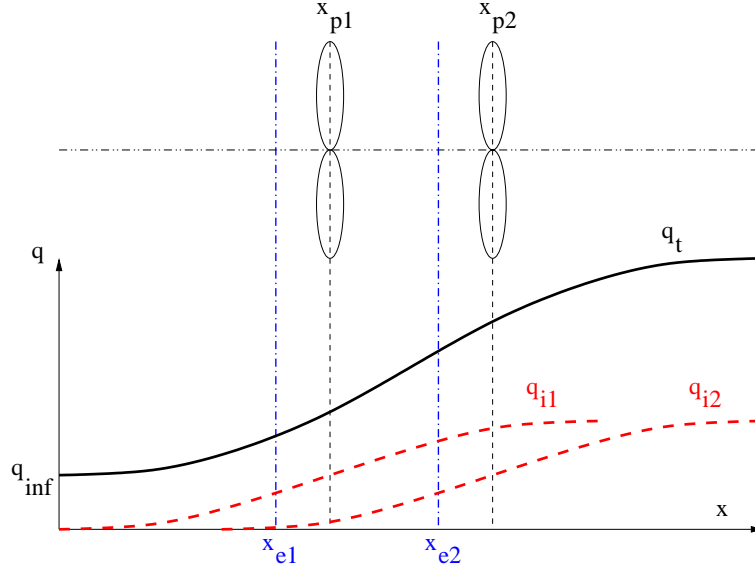
Figure 4.4: Schematic diagram showing the axial velocity distribution along the shaft axis; the total velocity q_t, the induced velocities of each components, q_{p1} and q_{p2}

are located at $x = x_{p1}$ and $x = x_{p2}$. At each component locations x_{p1} and x_{p2}, the total velocity can be considered as

$$\vec{q}_t(x_{p1}) = \vec{q}_a(x_{p1}) + \vec{q}_{p1}(x_{p1}) + \vec{q}_{p2}(x_{p1}) \tag{4.11}$$

$$\vec{q}_t(x_{p2}) = \vec{q}_a(x_{p2}) + \vec{q}_{p1}(x_{p2}) + \vec{q}_{p2}(x_{p2}) \tag{4.12}$$

where, $\vec{q}_a(x_{p1})$ and $\vec{q}_a(x_{p2})$ include the inflow and all the effects of the interaction. At these locations, the effective inflow to each component can be written as follows.

$$\vec{q}_{e1}(x_{p1}) \equiv \vec{q}_t(x_{p1}) - \vec{q}_{p1}(x_{p1})$$

$$= \vec{q}_a(x_{p1}) + \vec{q}_{p2}(x_{p1}) \tag{4.13}$$

$$\vec{q}_{e2}(x_{p2}) \equiv \vec{q}_t(x_{p2}) - \vec{q}_{p2}(x_{p2})$$

$$= \vec{q}_a(x_{p2}) + \vec{q}_{p1}(x_{p2}) \tag{4.14}$$

Since it is difficult to evaluate velocities accurately at the propeller locations,

46

the effective wake at the propeller is assumed to be equal to that which is evaluated at a plane just upstream of the propeller.

$$\vec{q}_{e1}(x_{p1}) \simeq \vec{q}_{e1}(x_{e1}) = \vec{q}_t(x_{e1}) - \vec{q}_{i1}(x_{e1}) \tag{4.15}$$

$$\vec{q}_{e2}(x_{p2}) \simeq \vec{q}_{e2}(x_{e2}) = \vec{q}_t(x_{e2}) - \vec{q}_{i2}(x_{e2}) \tag{4.16}$$

This assumption works very well in predicting the effective wake for single component cases. However, in the case of two-components, the difference in the induced velocity due to the other component between the two locations x_p and x_e is neglected. The effect of this assumption can be assessed by evaluating the effective wake at different locations upstream of each component and by comparing the resulting values of the inflow and the predicted forces [Kinnas 2001].

The overall procedure is shown in Figure 4.5. The iteration between the Euler solution and the two potential flow solutions (one for each component) is performed in a way that the new loadings on the two components are updated simultaneously. The steps within one global iteration can be summarized as follows.

1. Calculate the loading of each component based on the previous or the best guess of the effective inflow to each component. Nominal wake inflow can be used as the initial guess for most cases.

2. Apply the loadings to each component as body forces and solve the Euler equations to obtain the total velocity field.

3. Compute the next prediction of the effective inflow for each component by using Equations 4.15 and 4.16.

Body Force Distribution from Axisymmetric Euler solver
GBFLOW-X

Qbx

Effective
Inflow to Stator

Effective Inflow
to Propeller

Potential Flow Solver MPUF-3A

STATOR

Stator Blade
Loading

Potential Flow Solver MPUF-3A

PROPELLER

Propeller Blade
Loading
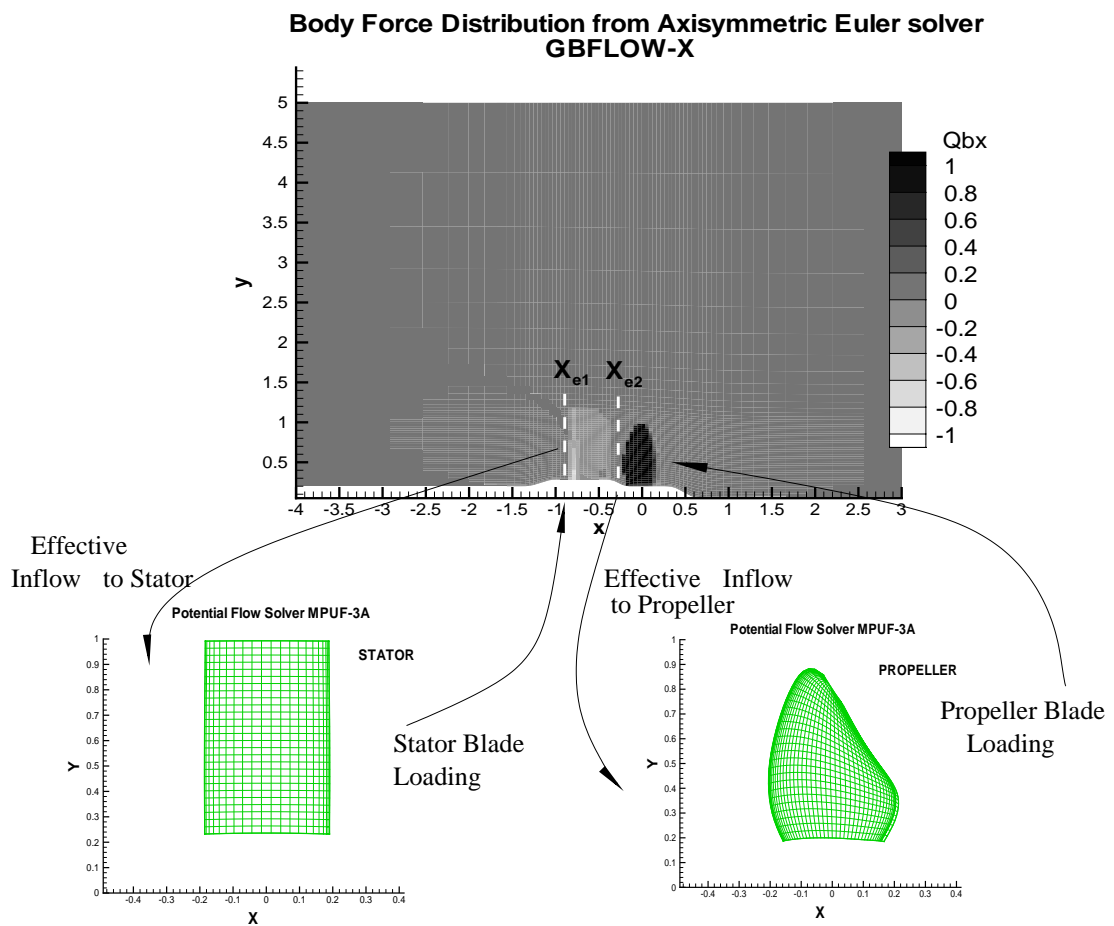
Figure 4.5: Overall procedure for the analysis of two-component propulsion system

The above procedure is repeated until convergence of the predicted forces is within a specified tolerance. As will be shown in later sections usually 3-5 iterations suffice depending on the convergence criterion specified.

4.2   The Stator-Rotor Propulsor

This section deals with the analysis technique used for solving the effective wake problem for a stator-rotor couple, using a vortex lattice based potential solver and an Euler solver.

A non-rotating stator blade is placed upstream or downstream of the rotating propeller (and accordingly called the pre- or post-swirl stator) for the purpose of swirl cancellation. The stator blade-system allows a partial recovery of the rotational energy by cancelling the swirl generated by the rotor, and therefore the stator serves as an efficiency increasing device. This gain outweighs the loss that occurs due to the stator blocking the flow and inducing a drag opposing the rotor's thrust. The combined system offers a higher performance efficiency as compared to a single-component system.

The treatment of a stator by the potential solver is similar to that of a propeller. The stator is analyzed as a propeller with zero angular frequency. The wake from the stator is considered to have a large pitch, resulting in a wake that goes straight back from the blades, as shown in Figure 4.6. The stator thrust and torque coefficients, which need to be defined in terms of the ship speed, are specified below.

$$\text{The torque coefficient } C_Q \;=\; \frac{Q}{0.5\rho V_s^2 \pi R^3} \tag{4.17}$$

STATOR AND WAKE
GEOMETRY

Ultimate
wake

Transition wake

Hub
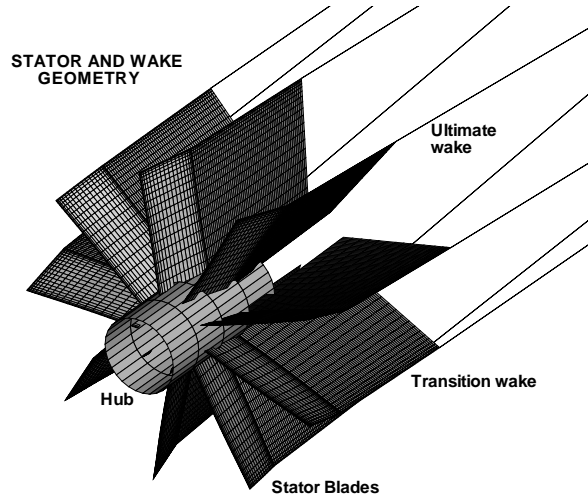
Stator Blades

Figure 4.6: Stator blade and wake geometry

$$\text{The thrust coefficient } C_T \; = \; \frac{T}{0.5\rho V_s^2 \pi R^2} \qquad (4.18)$$

The flow-field developed in the presence of the stator-rotor couple is solved for using the coupled approach discussed in the previous section. The potential flow solver solves for the panel singularity strengths and blade pressure forces for each component subject to a given inflow. The pressure forces obtained are input into the Euler solver, and are used to determine the body forces. The Euler equations are solved for the given body forces and the total velocity flow-field is determined. Using known blade and wake panel strengths, the propeller induced velocities can be determined at a given axial location upstream of the component. The effective velocity, defined in Equation 4.15, can then be obtained. The next potential solver run uses this modified effective inflow. The iteration process continues till convergence is achieved. The zeroth iteration corresponds to each component subject to a uniform inflow.

In the Euler solver, the stator is represented by body force cells, akin to a propeller. The axial component of the body force for a stator is negative (corresponding

to drag) and that of the propeller is positive, as shown in Figure 4.7. Also the tangential body force components are opposite in direction for the two components, resulting in the cancellation of rotational velocities.

Body Force Distribution in GBFLOW-X
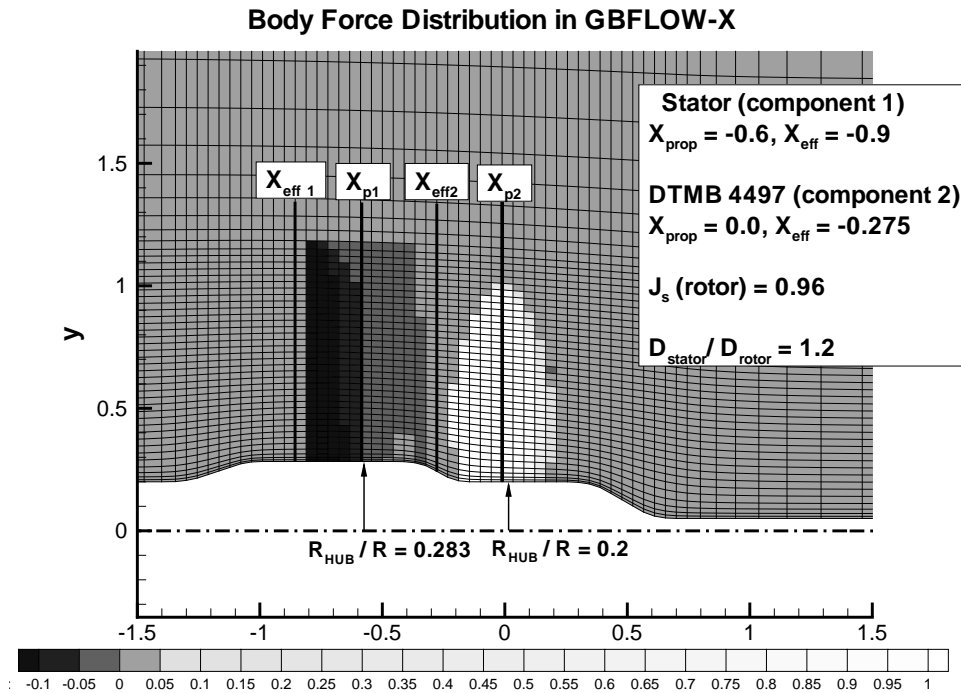
Figure 4.7: Two-dimensional grid showing hub geometry and the stator-rotor body force distribution

In the potential solver the hub is modeled using the image method [Kinnas 1996]. In the Euler solver, the hub is modeled by specifying the lower boundary of the grid to conform to the hub geometry. Separation of flow at the transition zones is avoided by smoothing out sharp corners in the hub geometry.

4.2.1 Convergence Studies

The loading or the circulation distribution of a propeller is a measure of the thrust provided by the propeller. The following figures show plots of the circulation dis-

Table 4.1: Variation in thrust and torque coefficients for different chord- and span-wise spacings, obtained using MPUF-3A for the Bowling stator

Span- & Chord-wise spacing	C_T	$10\,C_Q$
half-cosine & full-cosine	-0.0721	-1.866
uniform & full-cosine	-0.0716	-1.868
uniform & half-cosine	-0.0706	-1.824

Table 4.2: Convergence of thrust and torque coefficients with increasing values of the wake P/D, obtained using MPUF-3A for the Bowling stator

P/D	C_T	$10\,C_Q$
5	-0.0700	-1.818
20	-0.0714	-1.854
50	-0.0718	-1.8639

tribution as a function of radius, obtained by varying various run parameters in the VLM solver. The results presented are for a nine-bladed stator [Bowling 1987]. In order to validate the performance of the potential solver for a stator, convergence studies were performed by varying several input parameters such as panel spacing on the blade (see Figure 4.8) and pitch of the wake (see Figure 4.8 (b)). In Figure 4.8, Γ is the propeller blade circulation distribution; R is the propeller radius; and P/D refers to the non-dimensional pitch of the helical propeller wake, made non-dimensional by the propeller diameter, D. A more detailed explanation of these parameters can be found in [Lee et al. 2001].

The convergence of the thrust and torque coefficients for the two convergence studies performed is summarized in Tables 4.1 and 4.2.

The circulation distribution obtained from the current potential solver scheme,
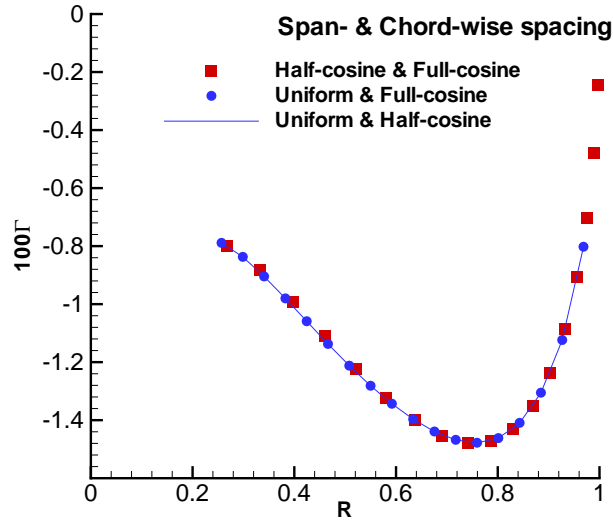
Figure (a)
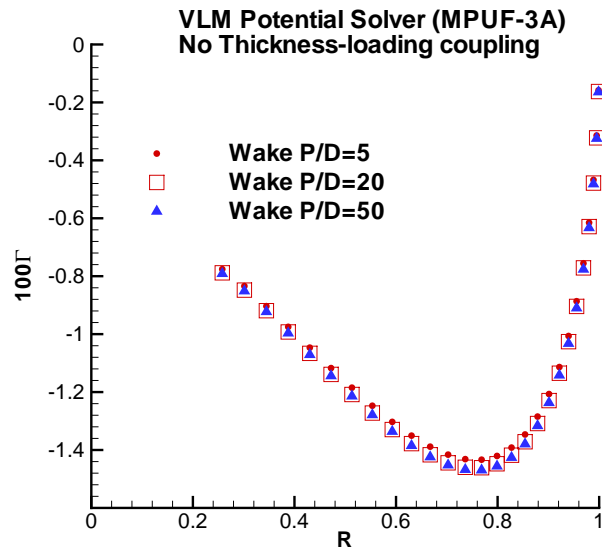
Figure (b)

Figure 4.8: Convergence of circulation distribution for (a) different span-wise and chord-wise spacing combinations - uniform, half-cosine and cosine spacing (b) increasing wake P/D ratios
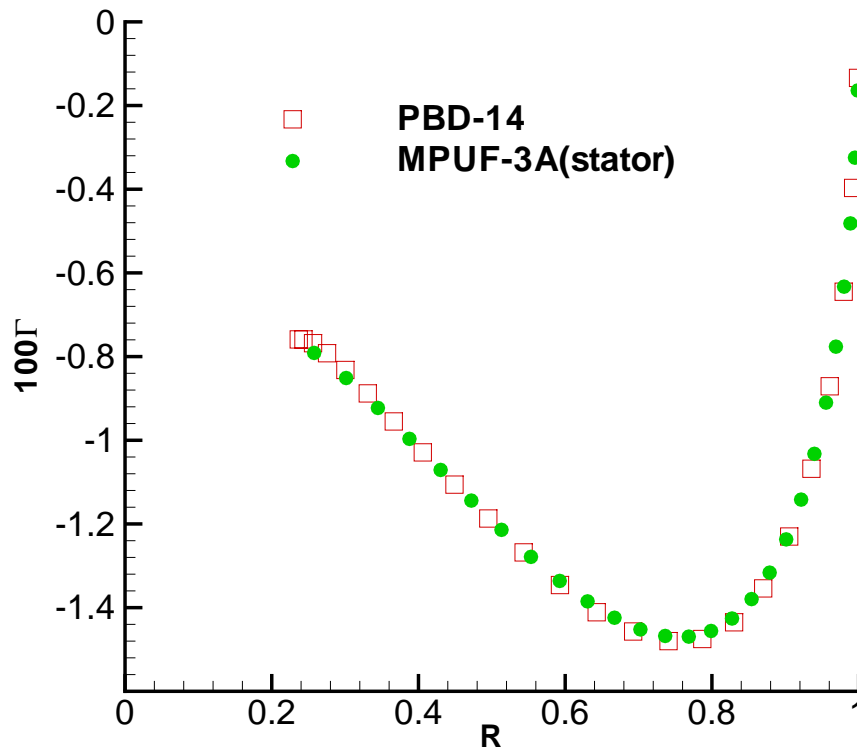
Figure 4.9: Comparison of circulation distributions obtained using MPUF-3A (based on lifting surface method) and PBD-14 (based on lifting line method)

with thickness loading coupling disabled, shows a good correspondence with results from PBD-14 [1]. For the MPUF-3A run, the blade was represented by 20 chord-wise panels and 27 span-wise panels; the thickness loading coupling and the viscous pitch correction were disabled; the hub image effect was included; the panels were distributed using a half-cosine spacing in the span-wise direction and a full cosine spacing in the chord-wise direction.

---

[1] MIT's Lifting Line code

4.2.2 Comparison of Numerical results with Experiment

Forces on a stator and rotor combination were observed experimentally in the MIT water tunnel and the present results were validated against the experimental data as well as the results presented in [Warren 1999]. The stator, 1.2 feet in diameter, was designed to operate with DTNSRDC (David Taylor Naval Ship Research and Development Center) model propeller 4497, which is one foot in diameter. The stator and rotor geometry are described in [Bowling 1987]. The grid geometry used for the coupled analysis is shown in Figure 4.7.

It usually takes three to five iterations for the values of the thrust and torque coefficients to converge. Figure 4.10 shows the convergence of these coefficients with the number of iterations. The flow-field obtained is shown in Figure 4.11. Within the propeller radius, the axial velocity increases due to the rotor action. The inflow velocity remains unchanged as we move radially away from the propeller. A cancellation of the tangential (swirl) component of the velocity is seen in Figure 4.11 (b). The velocity profile upstream of the stator (see Figure 4.12 (a)) shows an accelerated axial component and almost zero swirl. The rotor (Figure 4.12 (b)) sees a strong swirl component and a retardation of the axial velocity (due to the stator blocking the flow).

In spite of the inviscid flow assumptions made by the Euler solver, the circulation distribution obtained compares well (except at the hub) to the blade loading predicted by the viscous solver (results for a two-component system in [Warren 1999] are obtained using a coupled lifting line/RANS solver). Results from both methods are off the experimental values, the VLM under-predicting the results (compared to the experimental results, the thrust and torque coefficients are lower by 2.5 and 6.6 %, respectively) while the Lifting line method over-predicts (Table
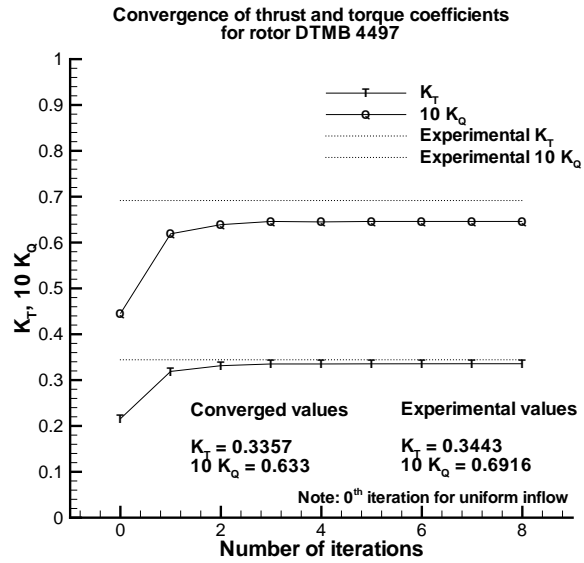
Figure 4.10 (a)
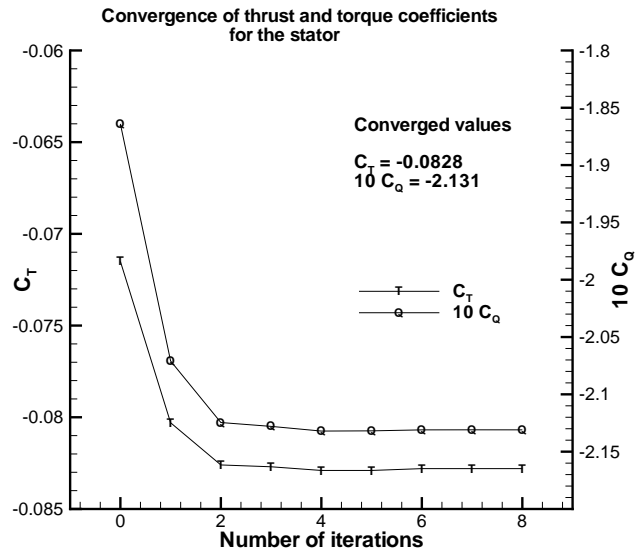
Figure 4.10 (b)

Figure 4.10: Convergence of thrust and torque coefficients with number of iterations for the (a) rotor and (b) stator
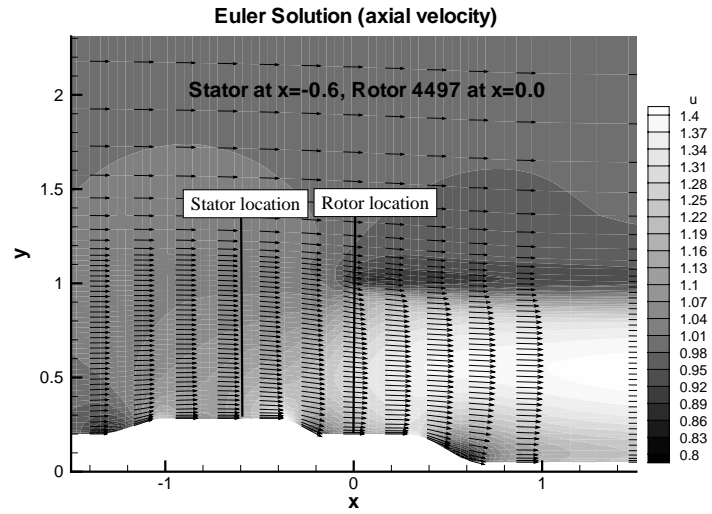
Figure 4.11 (a)
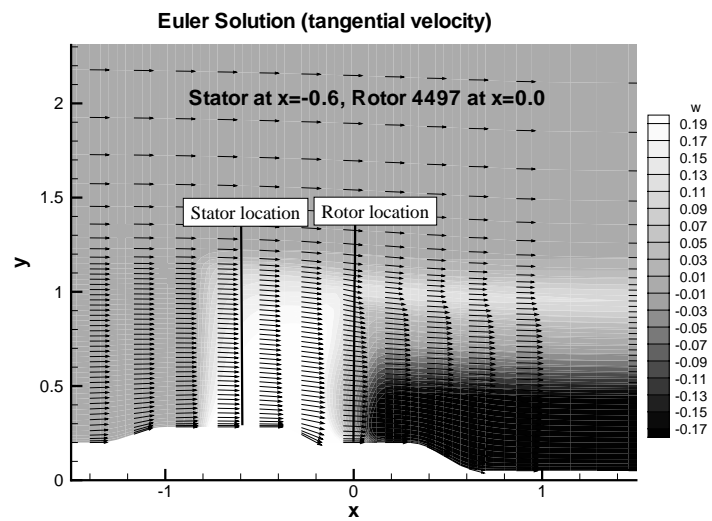
Figure 4.11 (b)

Figure 4.11: Contour plots showing (a) axial and (b) tangential velocity components
for the stator-rotor couple

57
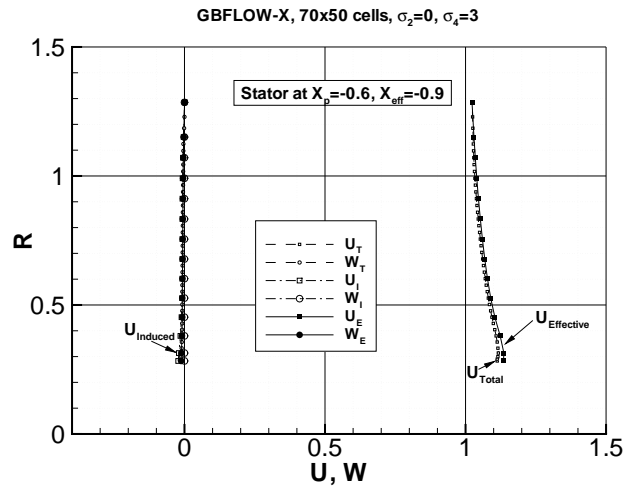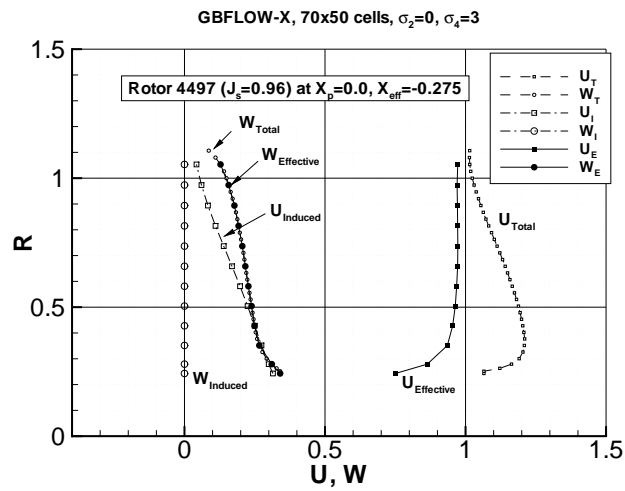
Figure 4.12-(a)

Figure 4.12-(b)

Figure 4.12: Total, induced and effective velocity profiles upstream of the (a) stator (b) rotor

Comparison of circulation distributions

	K_T	$10K_Q$
MPUF-3A/GBFLOW-3X	0.3357	0.646
PBD-14/DTNS3D	0.3694	0.7316
Experiment	0.3443	0.6916
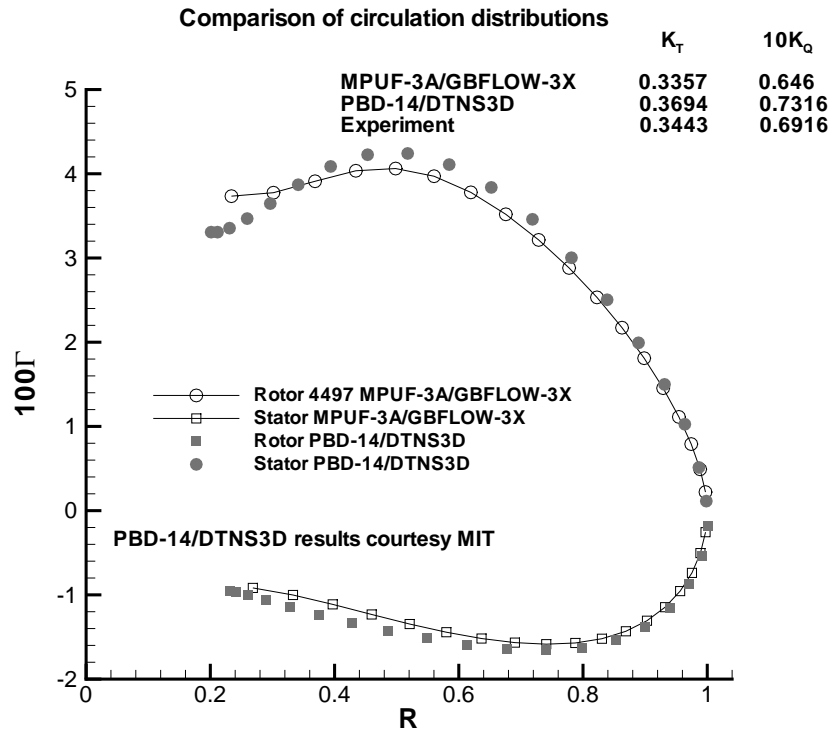
Figure 4.13: Comparison of rotor and stator circulation distributions obtained using MPUF-3A/GBFLOW-3X and MIT's PBD-14/DTNS3D

4.3).

The rotor and stator blade cavitation results presented next are hypothetical and are not compared with any experimental data. Comparison with experiments on cavitating stator-rotor couple is required in order to further validate the method. Due to the presence of the stator, the rotor sees a non-axisymmetric decelerated inflow which affects the cavitation pattern on the rotor blade. In order to obtain the non-axisymmetric wake, the stator-rotor couple is solved for using a 3D Euler solver. Figure 4.14 shows the 3D stator-rotor geometry and corresponding FVM body force distribution used in the 3D solver. The stator is represented by cells fixed in space, while the body force for the rotor is circumferentially averaged. Finally, the rotor is solved subject to the stator-modified effective wake (see Figure 4.15). In Figure 4.15,

59

Table 4.3: Comparison of thrust and torque coefficients for propeller DTMB 4497, obtained using MPUF-3A/GBFLOW-3X and MIT's PBD-14 and DTNS3D

	C_T	$10\, C_Q$	K_T	$10\, K_Q$
MPUF-3A & GBFLOW-3X (70x50 cells)	-0.0828	-2.131	0.3357	0.646
PBD-14 and DTNS3D [2]	-0.0839	-2.1138	0.3694	0.7316
Experimental	-	-	0.3443	0.6916
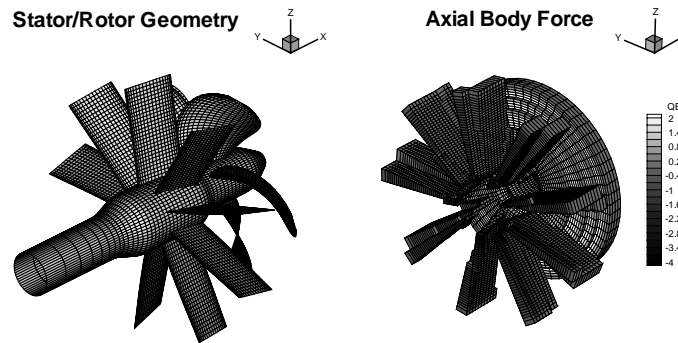
Figure 4.14: 3D stator-rotor geometry and body force cells

the propeller effective velocity field on a plane 0.3 radius upstream of the propeller plane is shown. A deceleration of the flow is observed at angles corresponding to the stator blade locations. The gray scale shade represents the axial effective velocity and the vectors represent the transverse components of the effective velocity. The blade cavitation pattern, shown in Figure 4.16, has been obtained for a cavitation number, $\sigma_n = 1.6$.

The unsteady thrust coefficients clearly show the influence of the nine bladed stator and a corresponding number of peaks are observed (Figure 4.17). The ninth harmonic dominates the axial force and torque, as shown in Figure 4.18.

Effective velocity as seen by the rotor
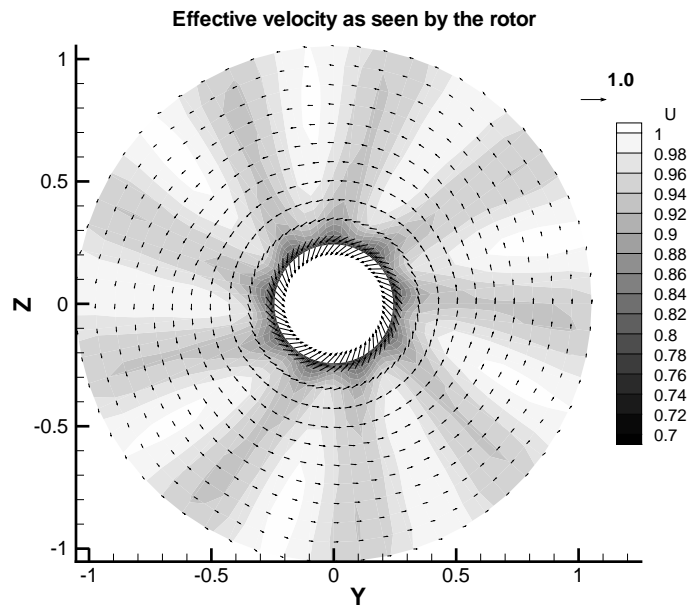
Figure 4.15: Effective wake to the rotor, in the presence of a pre-swirl stator

Rotor Blade Cavitation for Blade angle = 0°

Cavitation no., σ_n = 1.6

Froude no., F_n = 9.0

Advance ratio, J_s = 0.96
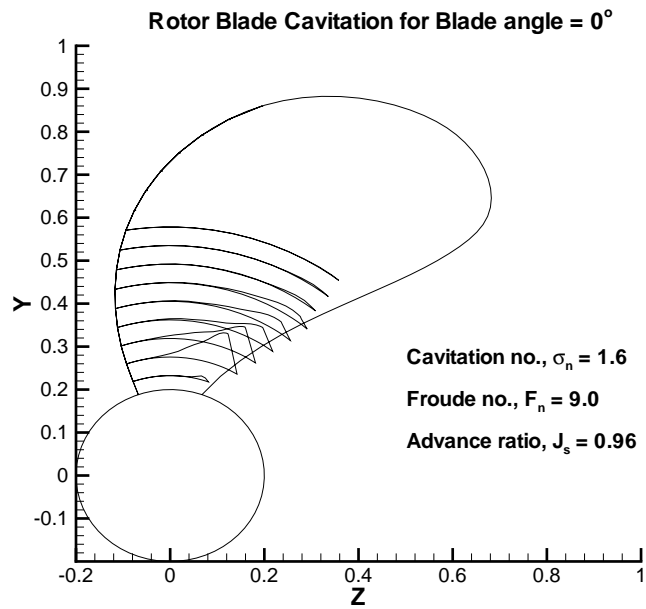
Figure 4.16: Rotor blade cavitation for $\sigma_n = 1.6$, Froude number, $Fn = 9.0$ and advance coefficient $J_s = 0.96$
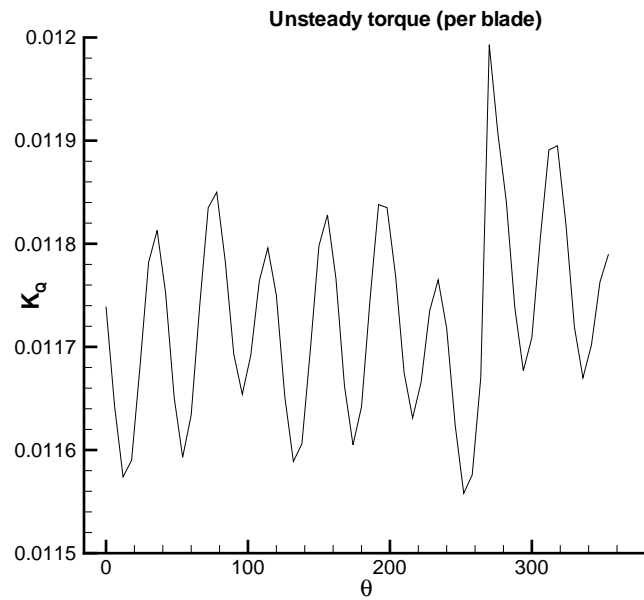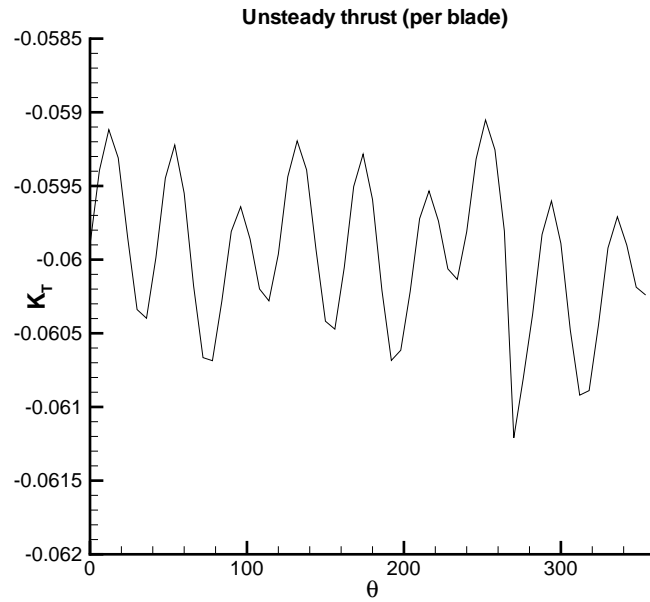
Figure 4.17: Unsteady wetted thrust and torque coefficients for propeller DTMB 4497
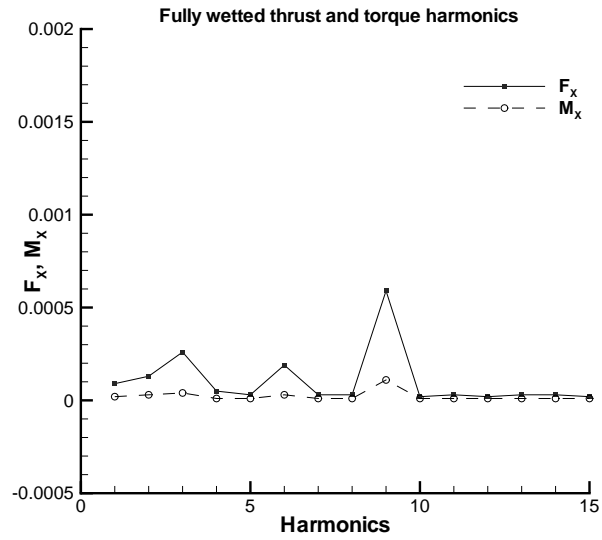
Figure (a)
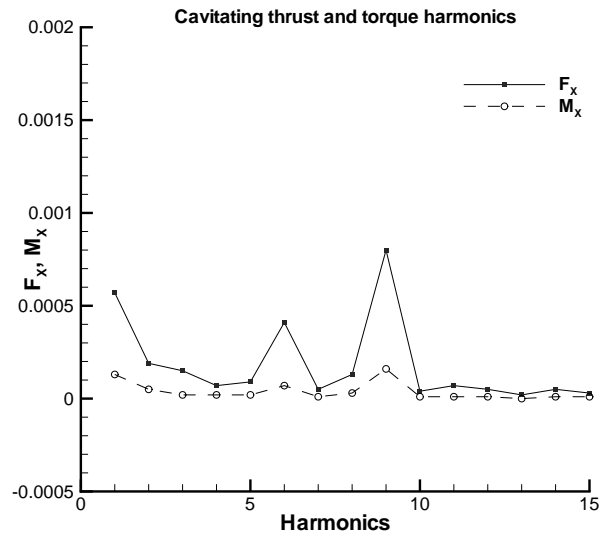
Figure (b)

Figure 4.18: Thrust and Torque Harmonics for propeller DTMB 4497 (a) before and (b) after cavitation.

The stator blade also experiences cavitation in the presence of the effective inflow upstream of the stator, as shown in Figure 4.19 (a), modified due to the action of the rotor. The cavitation developed on the blade (at 0° position) is primarily mid-chord cavitation, and is shown in Figure 4.19 (b).

4.3   Podded Propulsors

Podded propulsors are gaining wide acceptance in commercial ships. The podded propulsor has a higher propulsive efficiency and enables higher maneuverability. Besides these reasons, podded propulsors can lead to an increase in cargo and passenger space and also offer the added advantage of being able to be installed late in the ship building process.

A typical, though simplified, pod geometry is shown in Figure 4.20. As the pod geometry (including the strut) is non-axisymmetric, the axisymmetric version of GBFLOW cannot be used and instead the three-dimensional version is used iteratively with MPUF-3A.

GBFLOW-3D allows the user to provide a two-dimensional grid, which when rotated circumferentially gives a three-dimensional grid. This option requires that the geometry be axisymmetric. The other option is that the user generates an entirely three-dimensional grid. The latter option is used to generate the grid for a podded propulsor. The grid is cylindrical around the geometry and non-cylindrical beyond a specified radius. Figure 4.21 shows half of the domain used to model the geometry as well as a magnified view of the cell distribution near the pod. The cells are concentrated near the geometry and their size increases linearly far upstream and downstream.

Effective wake seen by the stator

Figure4.19 (a)

Stator cavitation for $\sigma_v = 0.25$, Fr=9.0

**Cavitation shown for
key blade
(Blade angle = 0°)**
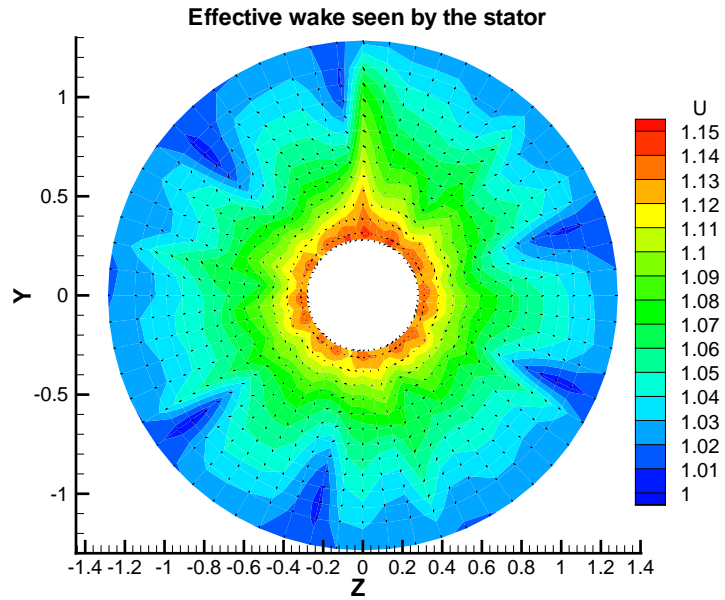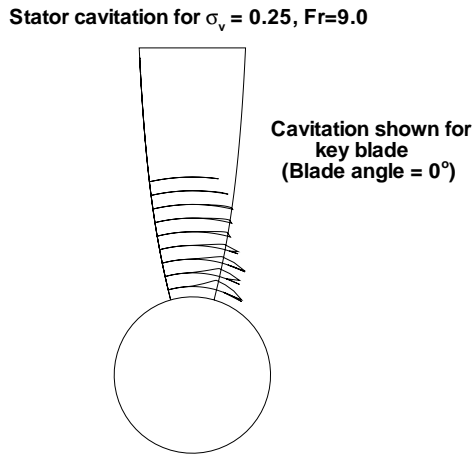
Figure4.19 (b)

Figure 4.19: (a) Effective inflow to the stator (b) Cavity pattern developed on stator blades
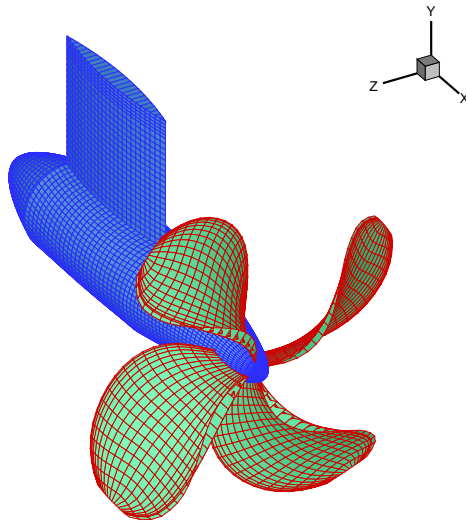
Figure 4.20: Podded propeller geometry

The hub radius for a podded propeller is no longer constant and the blade needs to follow the pod geometry. Therefore, MPUF-3A is modified to handle blades fitted within a specified hub and/or duct geometry. This is done by finding the intersection of the propeller blade with the duct/hub and re-paneling the modified blade geometry, keeping the number of panels the same. Also, the image method is modified to include the effect of the varying hub radius (details of scheme can be found in [Kinnas 2002]).

4.3.1   Results for Podded Propulsors

This section describes the results obtained from an iterative run between MPUF-3A and GBFLOW-3D for a push-type podded propulsor geometry. The solution requires 7 such iterations for the convergence of the axial force. This requires a CPU time of 13 hours on a Compaq Professional Workstation XP1000.

The effective inflow to the propeller, determined at an upstream axial loca-
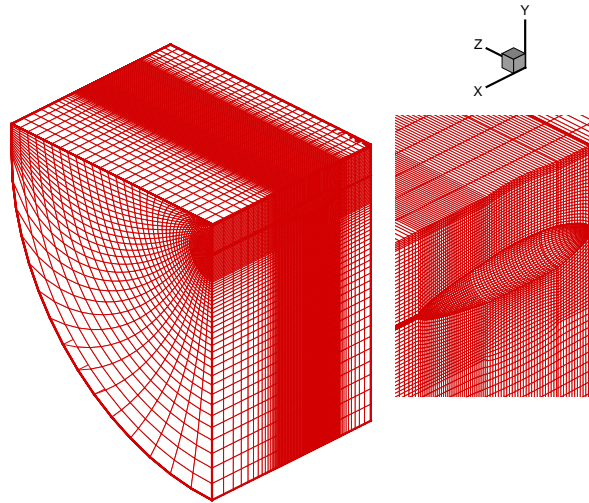
Figure 4.21: Three-dimensional grid used to model the podded propeller

tion, clearly shows the effect of the strut. The presence of the strut causes a decrease in the axial velocity (see Figure 4.22 (a)). In Figure 4.22 (b), the contour plot of the propeller induced velocity shows the influence of the four blades. Figures 4.23 and 4.24 show the axial velocity and pressure contours at the center plane of the grid, respectively. The expected acceleration and the pressure jump is seen across the propeller plane (located at $X_p = 1.34$). The integration of pressure on the pod geometry gives the axial force developed in the presence of the propeller. This is particularly useful to capture the beneficial effects of a strut located aft of the propeller. Figure 4.25 shows the convergence of the circulation distribution with number of iterations as well as the convergence of the axial force on the pod.

4.3.2   Various Podded Propulsor Configurations

In this section, results are presented for various possible podded propulsor configurations. These include the pull-type pod (where the propeller is located forward of the strut), the push-type pod (where the propeller is located aft of the strut, as

67
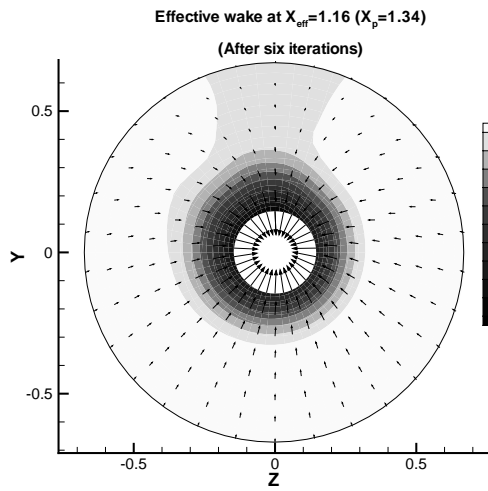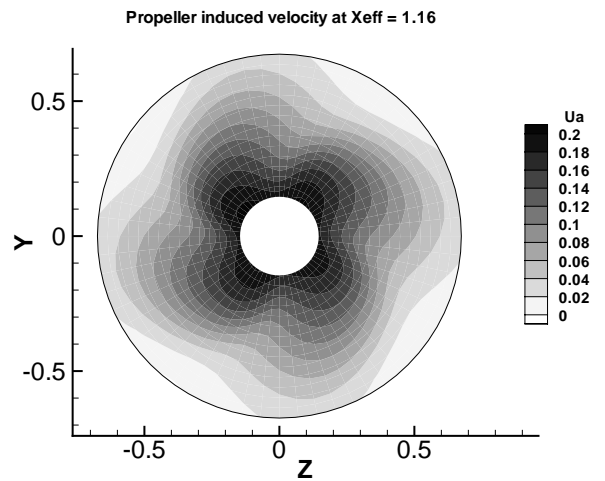
Figure 4.22 (a)

Figure 4.22 (b)

Figure 4.22: (a) Effective velocity and (b) Propeller induced velocity at an axial plane upstream of a push-type podded propeller

Axial Velocity contours on the Center plane
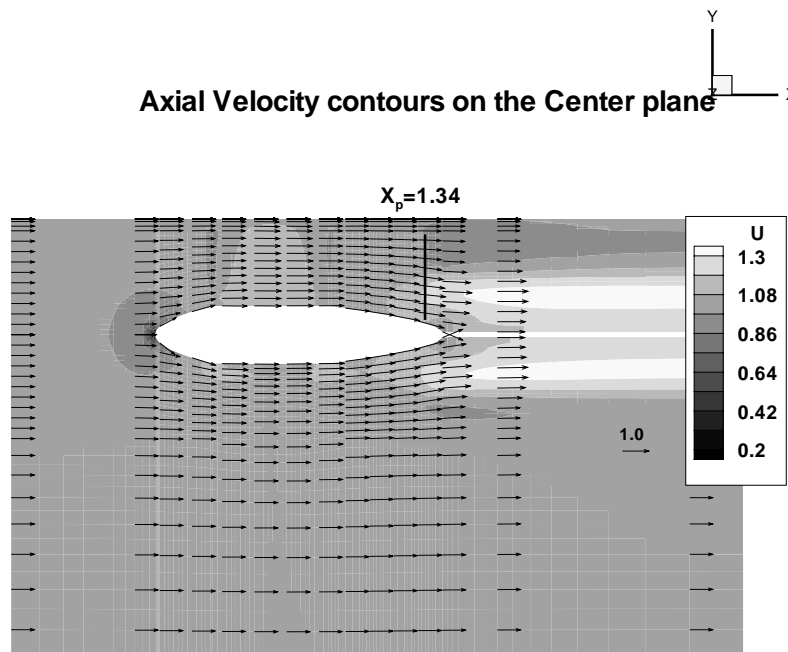
Figure 4.23: Axial velocity contours on the center plane of a push-type podded propulsor

Pressure Contours on the Center Plane
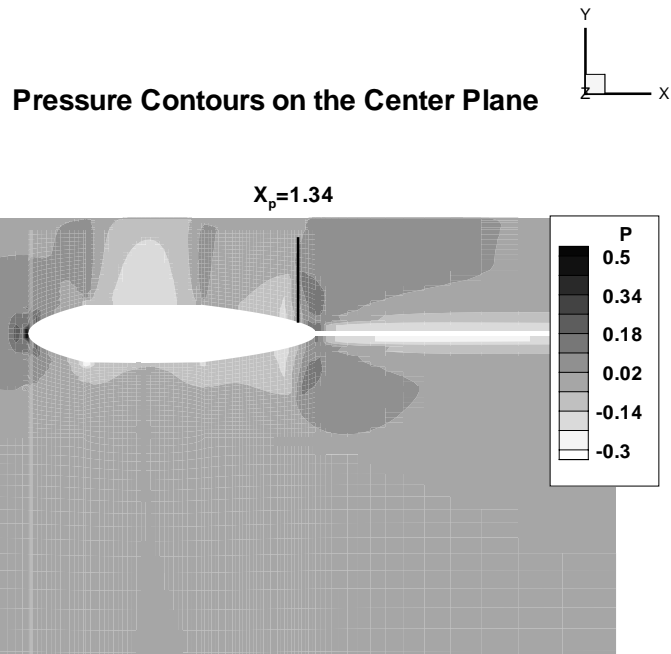
Figure 4.24: Pressure contours on the center plane of a push-type podded propulsor
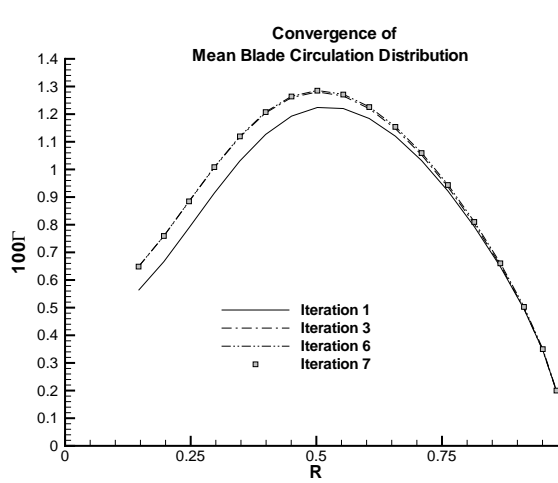
Figure 4.25 (a)
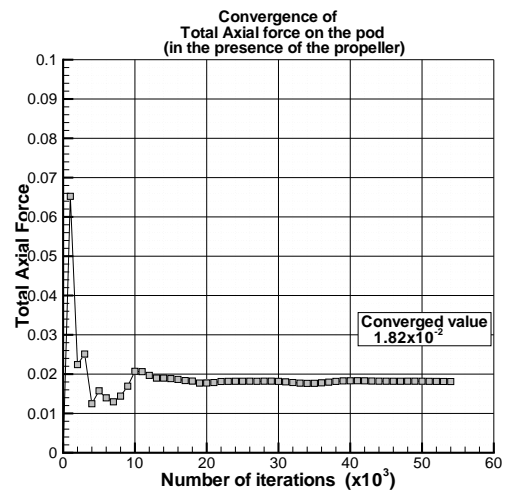
Figure 4.25 (b)

Figure 4.25: Convergence of (a) Mean circulation distribution and (b) Axial force acting on the pod, for a push-type podded propulsor

was shown in the previous section) and pod fitted with a pair of contra-rotating propellers. The results from these cases are compared to a case with the propeller absent i.e. the pod geometry placed in uniform open flow.

Figure 4.26 shows the axial velocity contours and total velocity vectors for the four configurations considered. The propeller location is shown by the variable X_p. In Figure 4.26 (a), as the propeller is absent the flow remains unaltered in most of the domain, though the presence of the pod alters the flow to some extent. For the push-type pod, an acceleration is observed aft of the propeller. Flow upstream of the propeller is unaffected (see Figure 4.26 (b)). In Figure 4.26 (c), the propeller is located upstream of the strut and the entire pod sees an accelerated flow. This effect is more pronounced for the contra-rotating pair due to the presence of two propellers.

Figure 4.27 shows the pressure contours for the different configurations. The pressure jump is observed across the propeller plane. Figure 4.28 shows the tangential velocity contours for the contra-rotating podded propulsor. Along the strut, the tangential velocity varies from positive to negative due to the changing slope of the strut section.

Figure 4.29 compares the total axial force acting on the strut for the four different configurations. As expected the force on the strut in the absence of the propeller converges to a value close to zero. The force on the strut is highest for the push-type pod and decreases for the contra-rotating pod and is lowest for the pull-type pod. The presence of the strut downstream of the propeller aids the thrust (similar to a post-swirl stator), and this is seen by the negative force acting on the strut (negative drag $\equiv$ thrust).

70

Axial velocity contours for a podded geometry (no propeller)

U
1.15
1.04
0.93
0.83
0.72
0.61
0.51
0.40
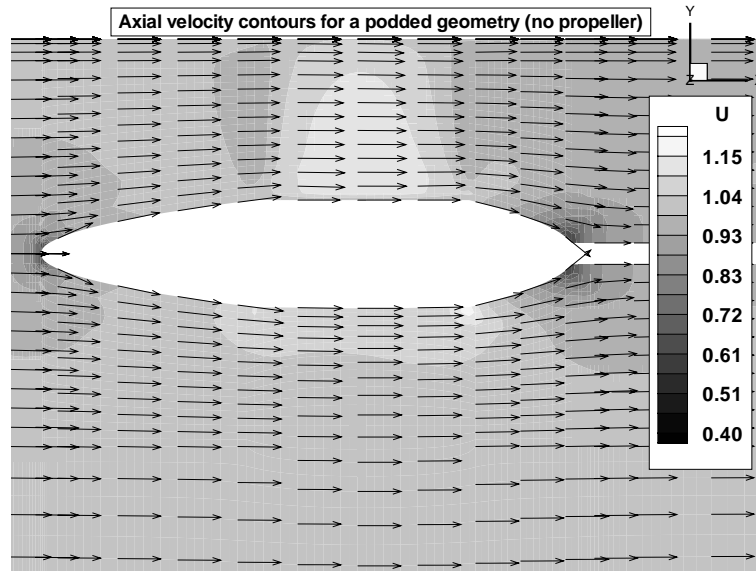
Figure 4.26 (a) No propeller

Axial velocity contours for a push type podded propulsor

X = 0.86

1.0

U
1.15
1.04
0.94
0.83
0.72
0.61
0.51
0.40
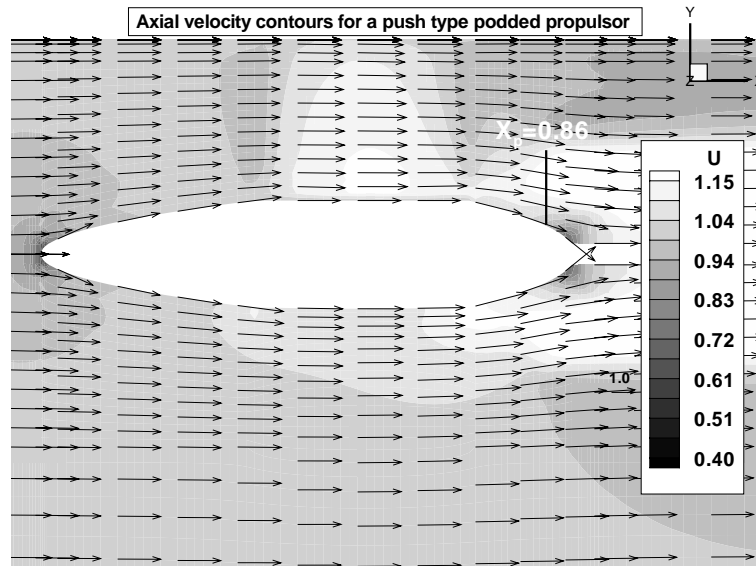
Figure 4.26 (b) Push-type pod

71

Axial velocity contours for a pull type podded propulsor

$X_p = 1.26$

U
1.15
1.04
0.93
0.83
0.72
0.61
0.51
0.40
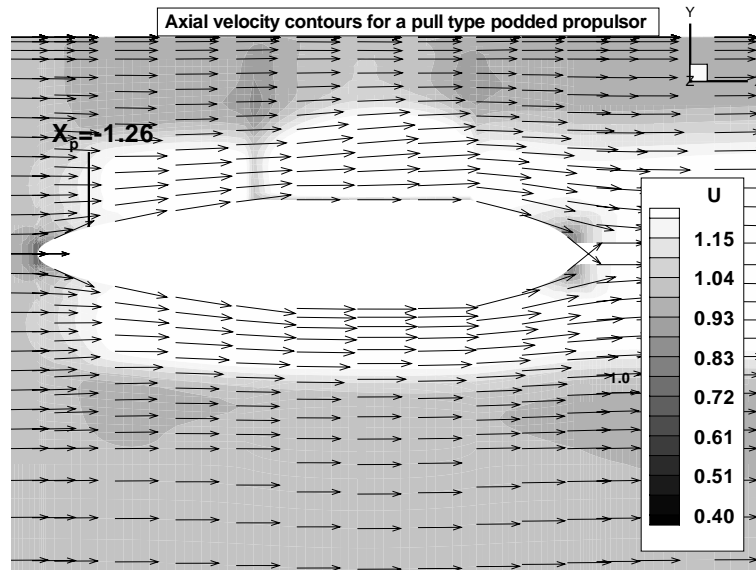
Figure 4.26 (c) Pull-type pod

Axial velocity contours for a contra-rotating type podded propulsor

$X_p = 1.26$ $X_{p2} = 0.86$

U
1.15
1.04
0.94
0.83
0.72
0.61
0.51
0.40
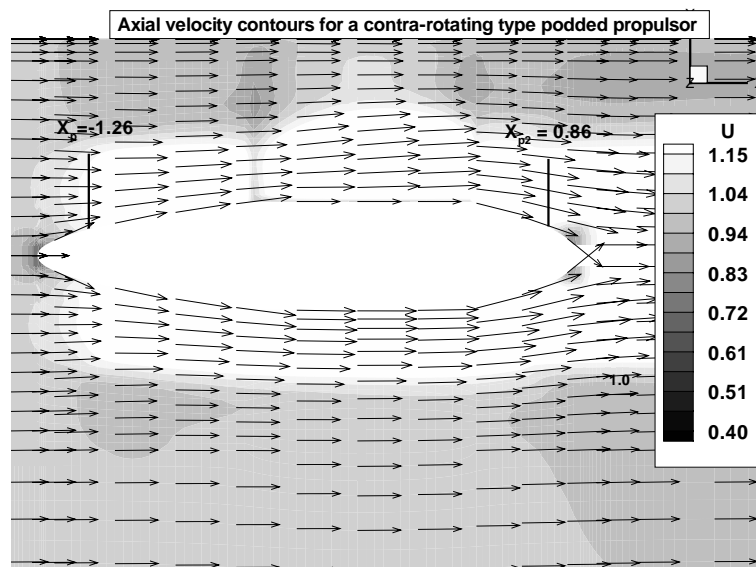
Figure 4.26 (d) Contra-rotating pod

Figure 4.26: Axial velocity contours and velocity vectors for four different podded propulsor configurations (a) No propeller (b) Push-type podded propulsor (c) Pull-type podded propulsor (d) Contra-rotating podded propulsor
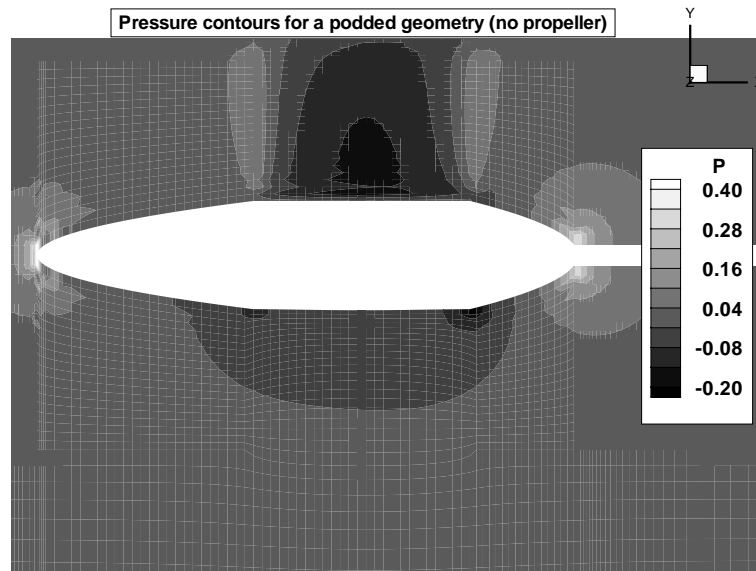
Figure 4.27 (a) No propeller
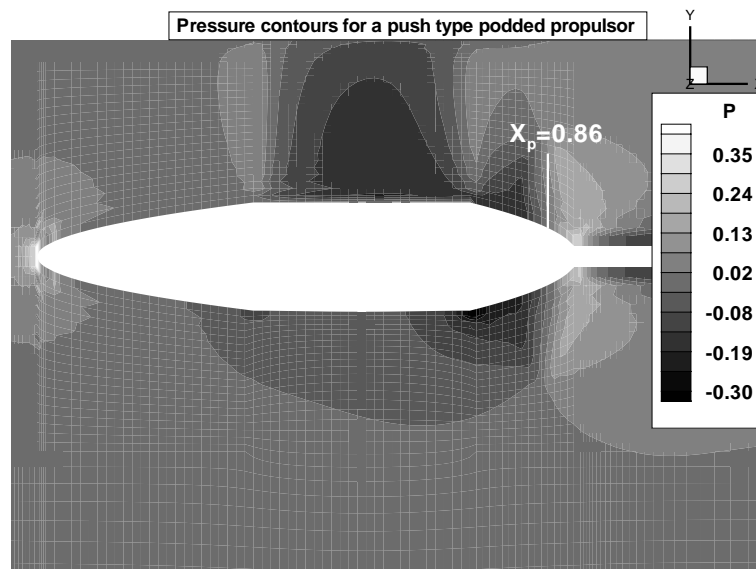
Figure 4.27 (b) Push-type pod
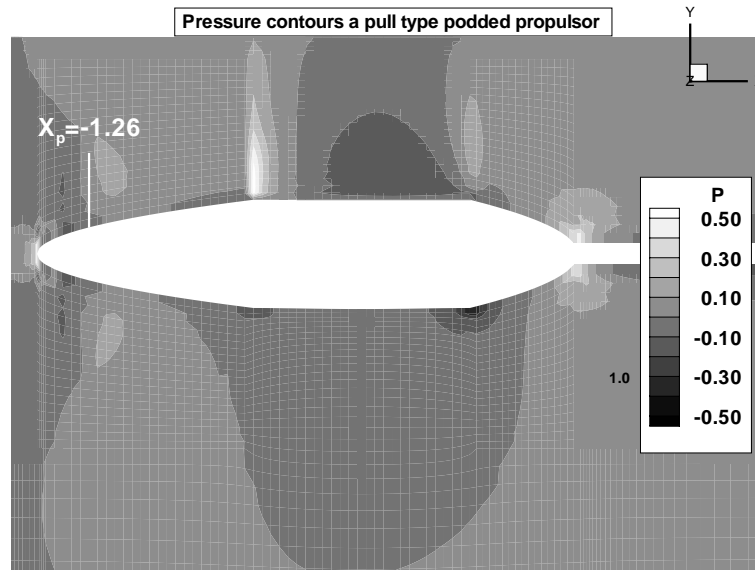
Figure 4.27 (c) Pull-type pod
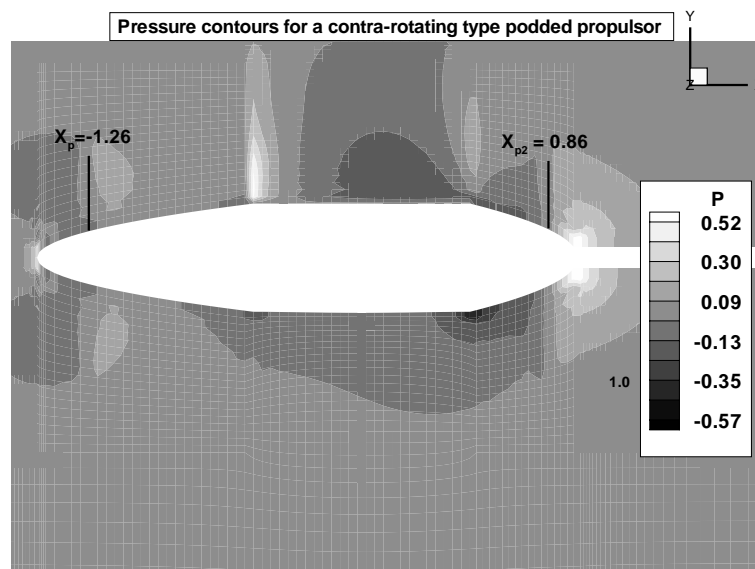
Figure 4.27 (d) Contra-rotating pod

Figure 4.27: Pressure contours and velocity vectors for four different podded propulsor configurations (a) No propeller (b) Push-type podded propulsor (c) Pull-type podded propulsor (d) Contra-rotating podded propulsor
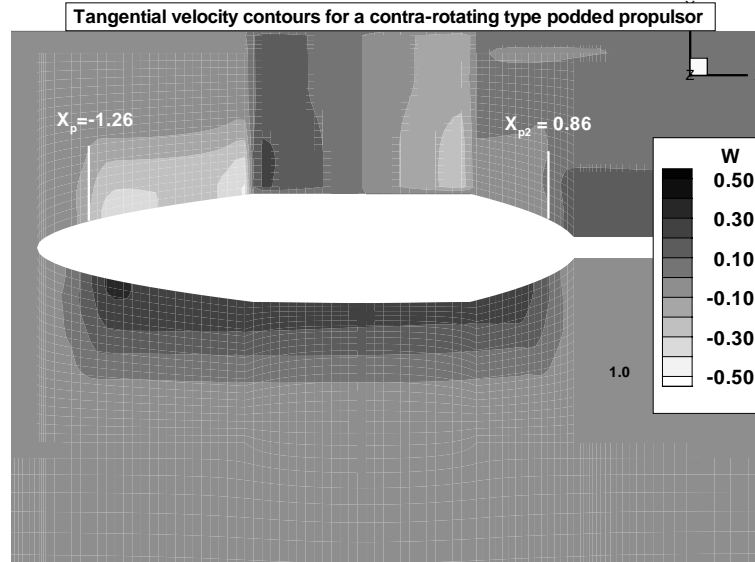
Figure 4.28: Tangential velocity contours for the contra-rotating podded propulsor

4.3.3 Comparison with Experimental Results

The coupled approach developed has been used for various simplified podded propulsor configurations. In order to validate the approach completely, it is essential to compare the method by applying it to a realistic geometry for which experimental data is available. One such experiment was performed by [Szantyr 2002]. A comparison to this work has been recently presented in [Hsin et al. 2002], where the flow past a podded propulsor has been calculated using both the boundary element method and a coupled viscous/potential flow code.

Geometry Details

The details of the experimental setup can be found in [Szantyr 2002]. Results for three different configurations, namely a single pull-type propeller, a single push-type propeller and a twin propeller system have been documented. The experiments were performed in the cavitation tunnel of the Technical University of Gdansk and
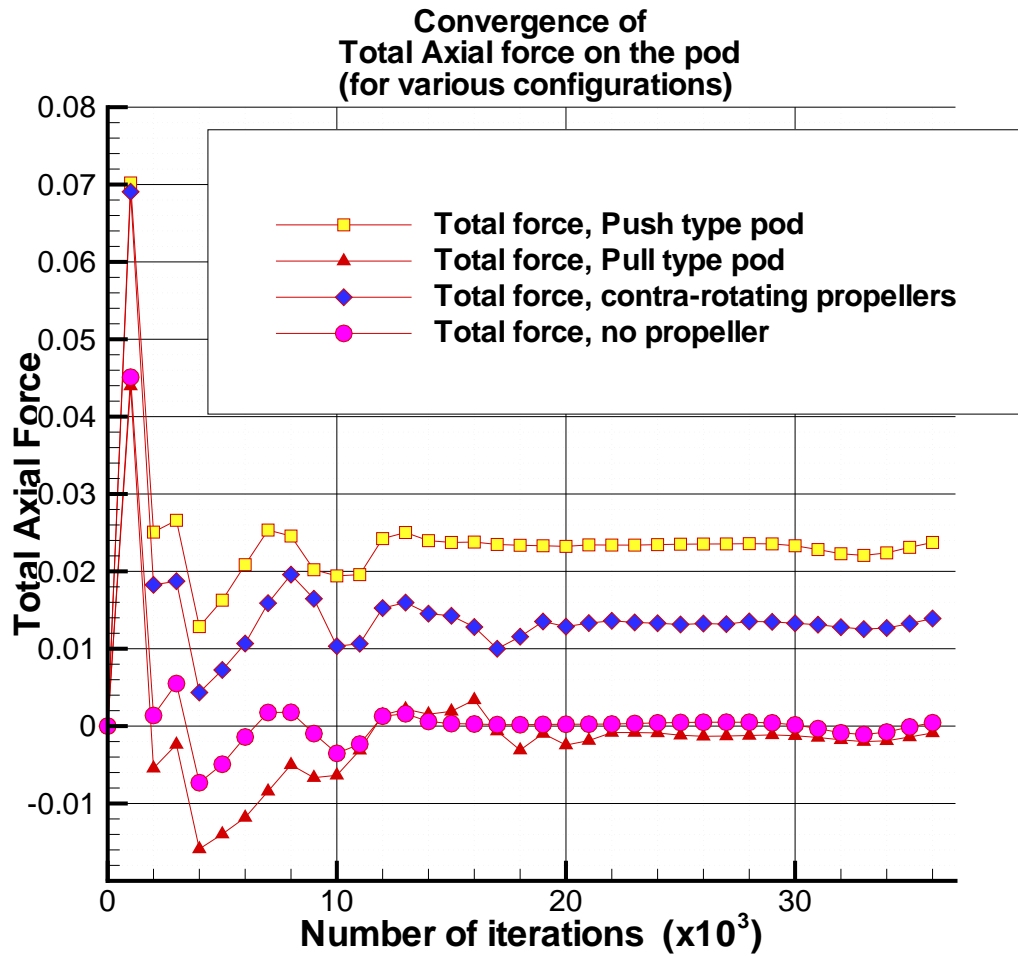
Figure 4.29: Convergence of total axial force acting on the pod for the four different podded propulsor configurations

the longitudinal and transverse components of the resultant hydrodynamic forces were measured for different advance coefficients and drift angle values. In order to validate the present method the single pull-type propeller case is considered, because apart from the experimental results, numerical results from [Hsin et al. 2002] are also available for the same configuration.

The principal dimensions of the pod are presented below.

- Length of pod propulsor model: $16.22in.\ (0.412\ m)$

- Maximum pod diameter: $2.91in.\ (074\ m)$

- Length of vertical strut: $5.51in.\ (0.140\ m)$

- Chord of strut: $4.29in.\ (0.109\ m)$

- Thickness of strut: $1.85in.\ (0.047\ m)$

The propeller used was a modified KCA 110, chosen from the series presented by [Gawn and Burrill 1957]. The propeller geometry was modified for a higher hub radius and the ratio $A/A_o = 0.8$ was maintained. The details of the propeller are presented below.

- Propeller KCA 110 (modified) Gawn-Burrill series

- Propeller diameter: $7.166in.\ (0.182\ m)$

- Hub diameter: $2.52in.\ (0.064\ m)$

- Number of blades: 3

- Blade area ratio $A/A_o = 0.8$

- Pitch of pull-type propeller (radially constant) P/D: 0.8

All dimensions are made non-dimensional with the propeller radius.

Results

First, the values of the thrust and torque coefficients for a range of advance coefficient values are compared to experimental data for the *unmodified* propeller geometry. These are open water results that are obtained in the absence of the pod, for a given uniform inflow. Figure 4.30 shows the comparison. As can be seen from the figure, the values of K_T and K_Q compare well with the experimental results, except for the low values of $J_s = 0.5$ and $J_s = 0.6$.

The numerical results for a single pull-type propeller placed in zero drift angle are compared to experimental results as well as results from [Hsin, 2002]. The longitudinal force acting on the pod is compared for three different values of the advance coefficient, J_s. The friction effect is included by obtaining the frictional force using the friction coefficient described below.

$$C_F = \frac{0.075}{(log_{10} Re - 2)^2} \tag{4.19}$$

where C_F is the friction coefficient, made non-dimensional by $\frac{1}{2}\rho U^2 S$; S is the surface area of the pod; U is the flow velocity; ρ is the fluid density. For a given value of the advance coefficient, the Reynolds number and therefore the friction coefficient can be determined. The friction coefficient when multiplied by the area of the pod gives the non-dimensional friction force, which is added to the result from the Euler solver. Figure 4.31 shows a comparison of the axial force obtained using the present method, results from [Hsin et al. 2002] and data from [Szantyr

78
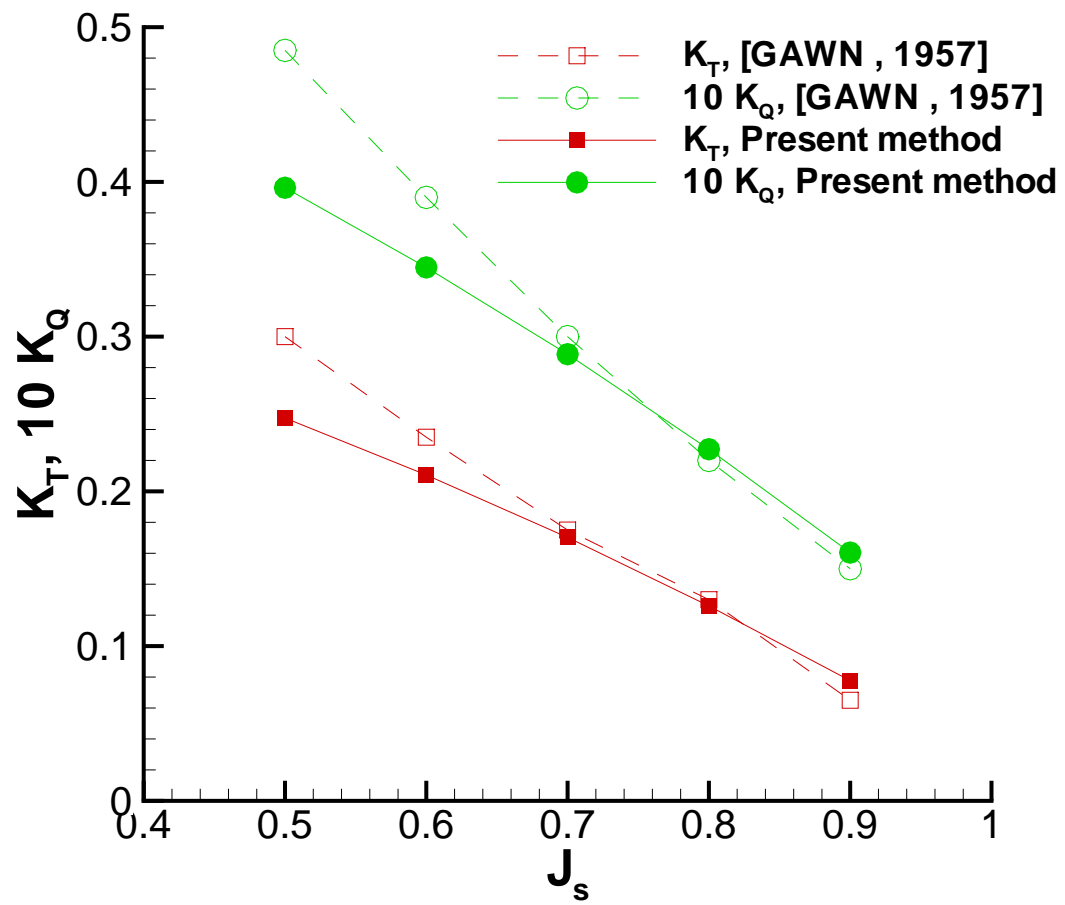
Figure 4.30: K_T and $10K_Q$ values from present method and from [Gawn and Burrill 1957], for propeller KCA 110

2002]. The values obtained from the present method compare well with values from [Hsin et al. 2002], and both the numerical results under predict compared to the experimental data.
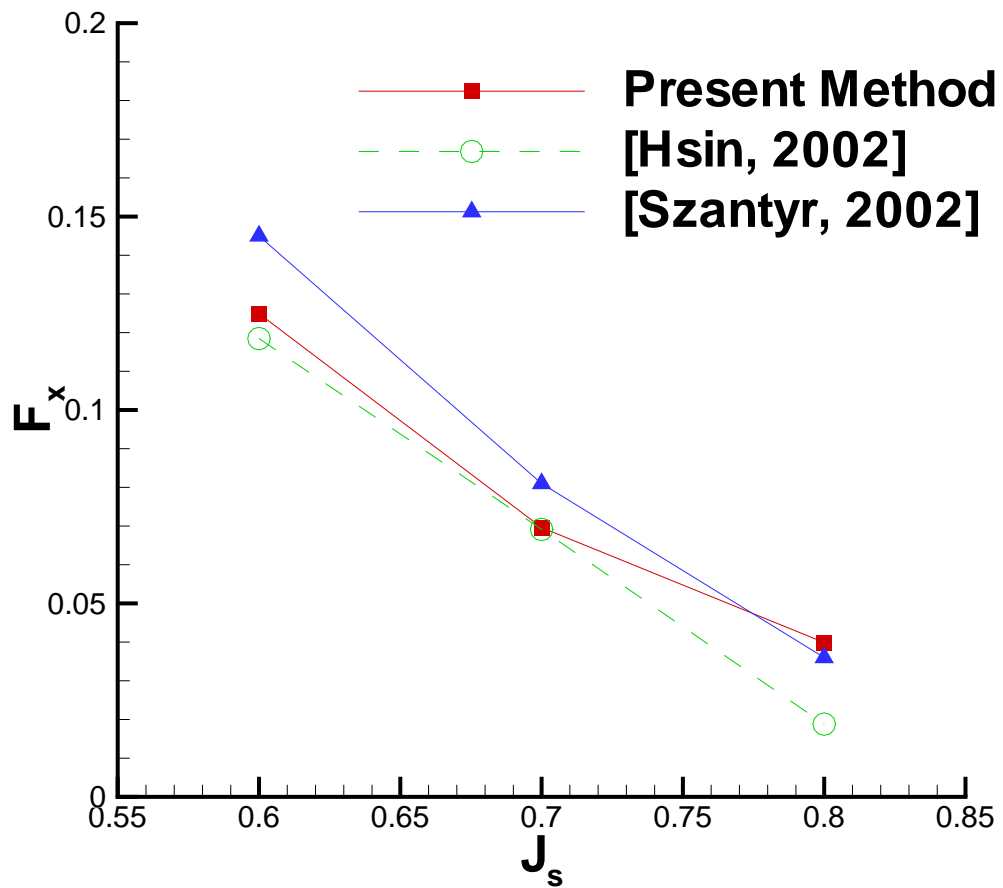
Figure 4.31: Comparison of axial force acting on pod, results from the present method, [Hsin et al. 2002] and [Szantyr 2002]

Chapter 5

FPSO Hull Motions: Heave and Roll

This chapter discusses the application of the two-dimensional unsteady Euler solver to the problem of a two-dimensional body moving at the free surface of a fluid. The motivation for studying the two-dimensional problem is to perform a rigorous treatment of the interaction between a body and a fluid with a free surface. Results of in-depth validation tests and convergence studies are presented in the first section. Next, the solver is applied to the problem of a flat plate placed normal to an oscillating flow and the results obtained are compared to experimental results presented in [Sarpkaya and O'Keefe 1995]. Finally, the results for the two-dimensional FPSO hull undergoing heave and roll motions are presented. A detailed study on the effect of the presence of the bilge keels, the bilge keel depth (as a fraction of the ship beam) and the effect of varying the forcing function is performed.

5.1   Validation Tests

Unlike work presented in Chapter 4, where most of the results were obtained by modifying and extending past work ([Choi 2000],[Kinnas et al. 1998]), the method presented in this chapter needs to be sufficiently validated before applying it to the intended problem.

The underlying principle behind all the tests described in the next few sec-

tions is their simplicity. Specific problems, for which the analytical results are known or can be easily determined, have been chosen as benchmarks. Besides validating the method, going through this process also provides a clearer understanding of the intricacies of the numerical scheme and this insight was useful when working on the hull motion problem.

5.1.1 Checkerboard Pressure Distribution

The first such test described is the checkerboard distribution. Certain numerical schemes allow a checkerboard pressure distribution (1 and 0 on adjoining grid points) to propagate, thus leading to a result which satisfies the numerical scheme but is entirely erroneous. An initial checkerboard distribution is applied to a rectangular grid (50×30 cells) in the presence of a uniform x-direction flow. The initial pressure is specified at all the nodes as $p_{i,j} = mod(i, 2) \times mod(j, 2)$, where i and j are the x- and y-direction indices, respectively. This results in an initial pressure distribution, as shown in Figure 5.1, such that the pressure is '1' at all nodes with even 'i' and 'j' values and zero on all other grid points. The solution is allowed to develop and the converged results are studied to check if the error has been propagated over subsequent time steps.

Boundary Conditions

Before going into the results, it would be worthwhile to explain the boundary conditions specified at the four boundaries of the grid. In any numerical problem, the solution is as good and accurate as the boundary conditions specified. The conditions are summarized below:

- Inlet: A uniform x-direction velocity was specified on the nodes along the

left boundary of the rectangular domain. Both pressure and the y-direction velocity are specified as zero. Specifying the pressure at one of the boundaries provides a reference pressure relative to which the pressure values on the other boundaries and within the domain are obtained. These conditions are expressed in Equation 5.1.

$$u = 1, \quad v, \, p = 0 \tag{5.1}$$

- Outlet: The first derivatives of the three variables are specified to be zero on the right hand side boundary of the rectangular domain (Equation 5.2).

$$\frac{\partial(p, u, v)}{\partial x} = 0 \tag{5.2}$$

If $u_{ni,j}$ represents the value of the x-direction velocity at the outlet boundary, and $u_{ni-1,j}$ the value of the variable on the node next to the boundary, then from the finite difference formula for the first derivative we have:

$$\frac{\partial u}{\partial x} = \frac{u_{ni,j} - u_{ni-1,j}}{x_{ni,j} - x_{ni-1,j}} \tag{5.3}$$

Applying the condition of the derivative being equal to zero, this reduces to

$$u_{ni,j} = u_{ni-1,j} \tag{5.4}$$

Thus by having collocated variables (having the variables unknown at the grid points), the application of boundary conditions becomes easier.

- Top: The top boundary condition is the same as specified at the inlet boundary.

$$u = 1, \quad v, \, p = 0 \tag{5.5}$$

- Bottom: At the bottom boundary, the y-direction velocity (v) is specified as zero, while the first derivatives of pressure and the x-direction velocity (u) with respect to y are specified as zero.

$$\frac{\partial(p, u)}{\partial y} = 0, \quad v = 0 \tag{5.6}$$

Numerically, this is treated in a similar fashion as described for the outlet boundary condition.

- Checkerboard pressure distribution (at t=0): Initially, the pressure distribution is specified as given in Equation 5.7.

$$p_{i,j} = mod(i, 2) \times mod(j, 2) \tag{5.7}$$

where i and j are the x- and y-direction indices. This results in an initial pressure distribution such that the pressure is '1' at all nodes with even 'i' and 'j' values and zero on all other grid points.

Results

The initial checkerboard distribution specified is shown in Figure 5.1. As is seen from the figure, the pressure is one at alternate grid points and zero in between. Figure 5.2 shows the convergence history for the above run. The solution converges when the difference in the values of all the variables between two successive iterations falls below a prescribed limit. The converged solution is shown in Figure

85

Initial Checkerboard Distribution for Pressure

t = 0.0
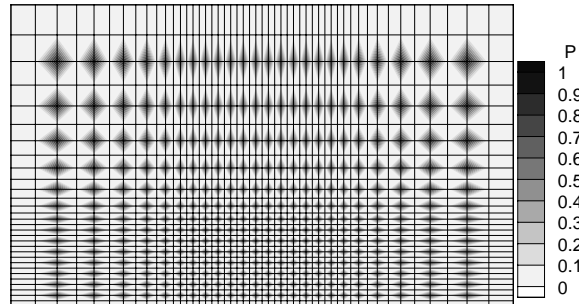
Figure 5.1: Initial checkerboard distribution specified on the rectangular domain

5.3. As is expected from a correct numerical scheme, the initial checkerboard distribution is replaced by a uniform pressure distribution, as should be the case for a uniform flow-field.

5.1.2 Oscillating Flow in a Rectangular Domain

Next the solver is applied to a problem for which the analytical result is known. The problem can be defined as follows. Consider a rectangular domain. A sinusoidal axial velocity ($u = U_o sin(\omega t)$) is specified at the four boundaries of the domain. For this situation, the momentum equation in the x-direction reduces to

$$\frac{\partial u}{\partial t} = -\frac{\partial p}{\partial x} \qquad (5.8)$$

86
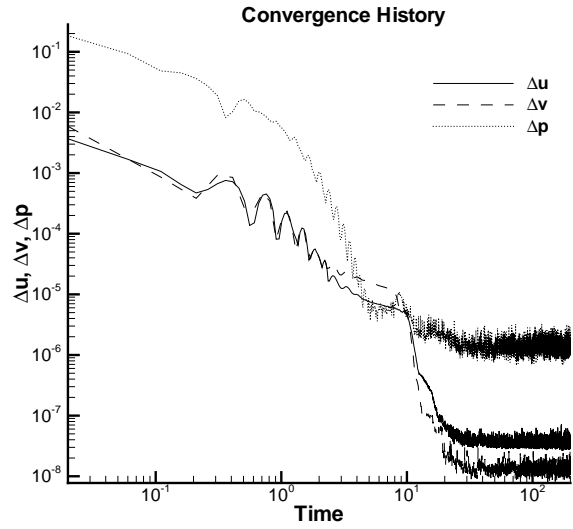
Figure 5.2: Convergence history for the checkerboard validation test
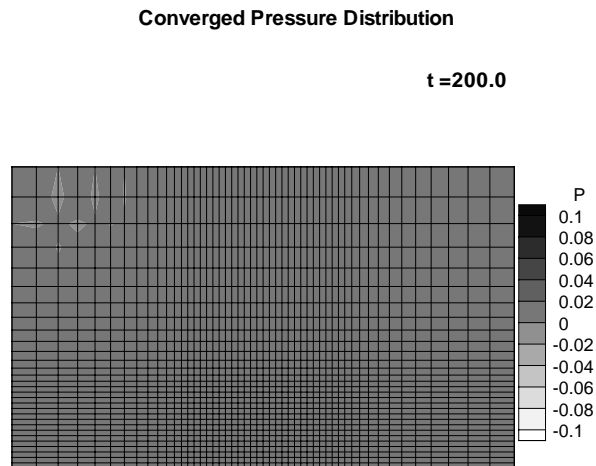
Figure 5.3: Converged solution obtained, after starting from an initial checkerboard pressure distribution

Boundary and Run conditions

The boundary and run conditions for the above problem are described below. A rectangular grid with 120×60 cells (domain: $-6 \leq x \leq 6, 0 \leq y \leq 6$) is used. A time step, $\Delta t = 0.001$ sec is used with 100000 of time steps, giving a total run time of 100 seconds.

- On all four boundaries a sinusoidal x-direction velocity is specified, i.e. $u = U_o sin(\omega t)$ on all boundaries, where $U_o = 1.0$ is the velocity amplitude, $T = 8secs$ is the time period and $\omega = \frac{2\pi}{T}$ is the corresponding frequency.

- Upstream and Downstream: On these boundaries, the second derivative of pressure with respect to x is specified as zero. Also the vertical velocity is zero on these boundaries.

$$\frac{\partial^2 p}{\partial x^2} = 0, \quad v = 0 \tag{5.9}$$

In order to numerically implement the pressure boundary condition, we once again resort to the known finite difference formula for the second derivative. This is given in Equation 5.10 for any point (ni, j) on the downstream boundary and for a uniform grid (spacing Δx).

$$\frac{\partial^2 p}{\partial x^2} = \frac{p_{ni,j} + p_{ni-2,j} - 2p_{ni-1,j}}{(\Delta x)^2} \tag{5.10}$$

Applying the condition of the derivative being equal to zero, this reduces to a simple extrapolation expression:

$$p_{ni,j} = 2p_{ni-1,j} - p_{ni-2,j} \tag{5.11}$$

88

The pressure at the boundary can thus be easily determined in terms of known pressures in the interior of the domain. It can be seen that this is the only boundary condition that will work for this problem. As we expect to see a pressure gradient ($\frac{\partial p}{\partial x}$) in the x-direction, specifying the pressure or a zero first derivative on the vertical boundaries would result in a divergent result.

- Top and Bottom: At the top and bottom boundaries, v velocity is explicitly specified as zero, while the first derivative of pressure with respect to y is taken to be zero. This also is also evident from the nature of the problem. As we do not expect to see any variation in pressure in the y-direction, this implies that the derivative of pressure with respect to y should be zero. These conditions are summarized in Equation 5.12.

$$\frac{\partial p}{\partial y} = 0, \quad v = 0 \tag{5.12}$$

Results

The solution is allowed to develop and the resulting pressure gradient is compared with the expected analytical value of the acceleration ($\frac{\partial u}{\partial t} = U_o \omega cos(\omega t)$), according to Equation 5.8. The numerical and the analytical values for the pressure gradient are presented in Table 5.1, and show an excellent correspondence. The Table also shows the % error observed in the vertical, v, velocity. Figures 5.4 and 5.5 shows the pressure contours obtained for two different time instants, separated by half a time period. The complete reversal of the pressure distribution corresponds with the change in the direction of the u velocity.

Time (sec)	$\frac{\partial u}{\partial t}$	$-\frac{\partial p}{\partial x}$	Error in v velocity
t=0	0.785398	0.78586667	0.06 %
t=T/4	-0.0493	-0.0491754	0.002 %
t=T/2	-0.785398	-0.78588750	0.06 %

Table 5.1: Comparison of the analytical and numerical values of $-\frac{\partial p}{\partial x}$ for the oscillating flow problem

Pressure Contours for time=88.0 secs
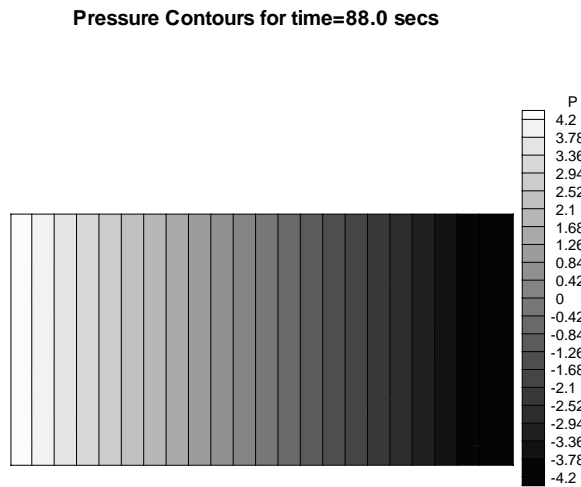
Figure 5.4: Pressure contours at $t = 0$ secs, for the oscillating flow problem
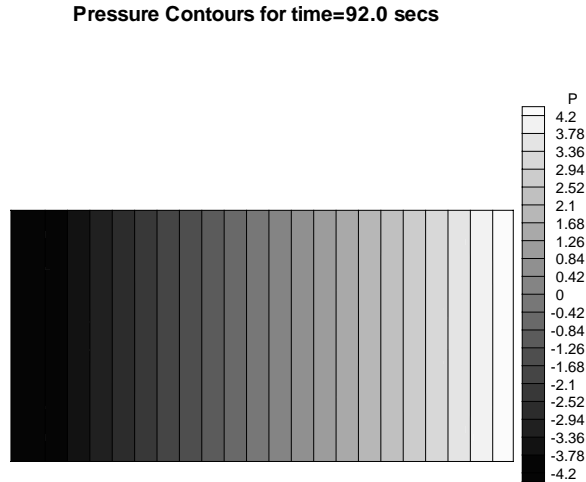
Figure 5.5: Pressure contours at $t = \frac{T}{2}$ secs, for the oscillating flow problem

'F=ma' check

In order to validate the numerical integration scheme, the force acting on the square body is determined by two approaches (grid shown in Figure 5.6). The run conditions are same as that described in Section 5.1.2. Firstly, the force is determined by integrating the pressure on the vertical sides of the square. This is compared with the expected value of force obtained as a product of the mass and acceleration. The mass of the square is simply the area of the body, for a unit density and depth. The acceleration is known as the first derivative of the sinusoidally varying velocity. A comparison of the forces obtained by the two approaches is shown in Figure 5.7. As seen in the plot, the pressure integration scheme gives an accurate estimate of the actual force.

**Transparent square located in the center
of the domain**
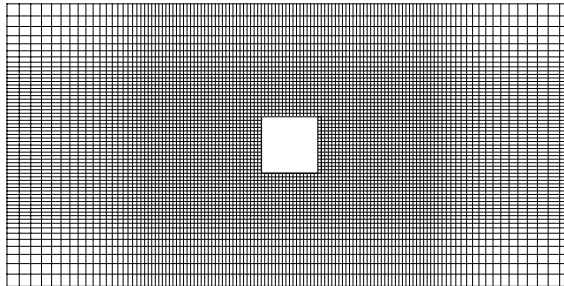
Figure 5.6: Rectangular grid, with transparent square boundary outlined, used to verify the numerical pressure integration scheme
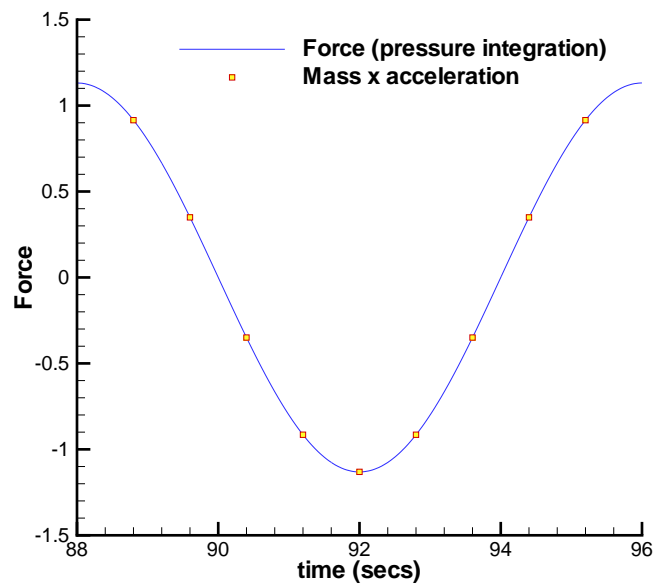
Figure 5.7: Comparison of forces determined by the pressure integration technique and the $F = ma$ approach

5.1.3 Oscillating Flow over a Circular Bump

Another problem that was used to validate the method developed was that of a circular cylinder subject to an oscillating flow. A semi-circular bump was used to model half a cylinder, and was subject to a sinusoidal axial velocity. The nodal pressure on the cylinder surface is integrated to determine the total axial force acting on the body (the force on the full cylinder is twice this force). Knowing the variation of the force over one time period, the least square approach can be used to determine the added mass and drag coefficients (these are the unknown constants in the Morison's equation (see [Newman 1977])). A description of the run and boundary conditions is provided below:

- Semi-circular cylinder with center at (x, y)=(0,0), Diameter = 1.0

- Domain size: -6 $\leq x \leq$ 6, 0 $\leq y \leq$ 6 (100 $\times$ 60 cells)

- Boundary conditions:

  - Upstream and Downstream: $\frac{\partial(p,v)}{\partial x} = 0; u = 0.1sin(\omega t)$

  - Bottom: $\frac{\partial(u,p)}{\partial y} = 0, \quad v = 0$

  - Top: $\frac{\partial(p,v)}{\partial y} = 0, \quad u = 0.1sin(\omega t)$

  - On the cylinder: $\frac{\partial(u,p)}{\partial n} = 0, \; q.n = 0$

- $\Delta t = 0.01$ sec, Number of time steps = 10000

Figure 5.8 shows the grid that was used for the computation. The pressure on the bump surface is numerically integrated to obtain the force on the cylinder surface. The added mass coefficient is then determined using the Morison's Equation

94
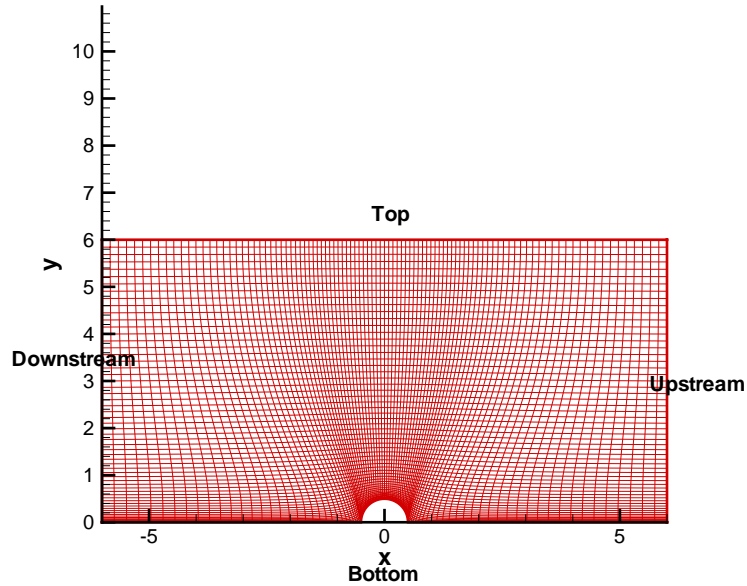
Figure 5.8: Rectangular grid with circular bump on bottom boundary

and least square approach. The determined inertia coefficient, C_m=2.063, while the analytical inertia coefficient, C_m=2.0. Figure 5.9 shows the force acting on the cylinder surface over one period of oscillation.

5.1.4 Numerical Wavemaker

Surface-waves, arising due to a moving body located at the free surface of a fluid, are one of the components responsible for providing damping. Therefore, it is important to ensure that the a surface-wave profile can be captured by the solver. It is important to note here that, though a surface-wave profile is seen at the free surface, the top boundary of the computational domain is not a moving boundary. The wave profile can be visualized by studying the velocity vectors at the free surface or by computing and plotting the wave elevation.
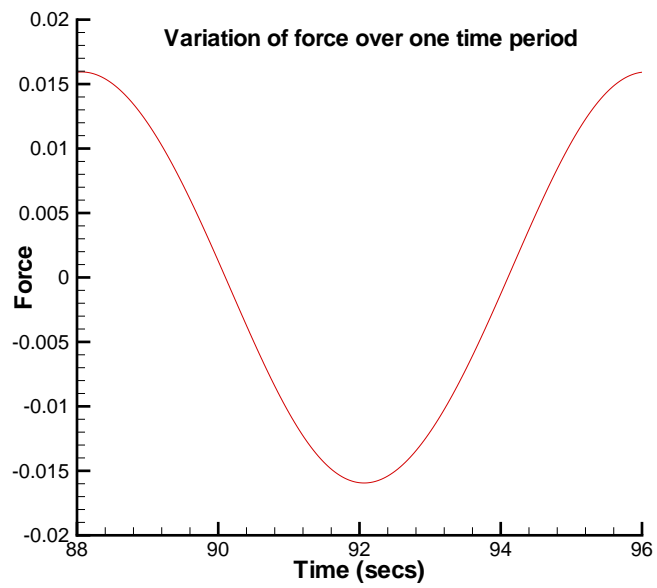
Figure 5.9: Axial force, over one time period, on the surface of a circular bump subject to an oscillating flow

The waves are assumed to be governed by linear wave theory, and the analytical expressions for the particle velocity components and the pressure below the free surface are shown below:

$$u = a\omega e^{kz} cos\theta \tag{5.13}$$

$$v = a\omega e^{kz} sin\theta \tag{5.14}$$

$$p = \rho g(\eta e^{kz} - z) \tag{5.15}$$

where u, v and p are the horizontal velocity component, vertical velocity component and the pressure respectively. In the above expressions, a is the amplitude of the wave; ω is the angular frequency, which is related to the time period T by $\omega = \frac{2\pi}{T}$; k is the wave number related to the wavelength L_o as $k = \frac{2\pi}{L_o}$; and $\theta = kx - \omega t$; x is the horizontal coordinate and z the vertical coordinate ($z = 0$ on the free surface); t is the time; ρ is the density of the fluid and η, the wave elevation is a function of both x and t and is related to them as $\eta = acos\theta$. It should be noted here that though all the formulation has been expressed in terms of the vertical coordinate y, z is the usual notation used to denote the vertical coordinate in wave theory. From our definitions, we have $z = -d$ when $y = 0$.

As is evident from the above equations, for negative z, the velocity components die down exponentially. Also, for deep water ($\frac{d}{L_o} \geq 0.5$), the particles move in circular paths with radius $r_o = ae^{kz}$.

A rectangular domain (2×1; 100×50 cells) is used for the computation. The velocities and pressure are specified explicitly, using Equation 5.13 at the inflow boundary. Knowing the analytical expressions for u, v and p, their derivatives with respect to x can be determined. At the outflow boundary, the derivatives are specified

equal to the analytical values. The velocities are assumed to be zero at the bottom boundary and the pressure at the bottom is extrapolated from the inner nodes.

The boundary condition on the free surface is described in detail in the section below.

Free surface boundary condition

Two conditions need to be satisfied at the free surface boundary. Firstly, the velocities of the free surface and fluid particles are equal. This condition is known as the *Kinematic Boundary Condition* [Newman 1977] and can be expressed as shown in Equation 5.16. In the equation, η refers to the wave elevation. Another condition that needs to be satisfied is that pressure is equal to atmospheric pressure at the free surface. This is known as the *Dynamic Boundary condition* [Newman 1977] and is shown in Equation 5.17 (with ϕ being the velocity potential). These represent the linearized free surface boundary conditions in the most general form, and are applicable under the assumptions that higher order terms and the surface tension are ignored.

$$v = \frac{\partial \eta}{\partial t} \tag{5.16}$$

$$\rho \frac{\partial \phi}{\partial t} + \rho g \eta = 0 \tag{5.17}$$

Solving the Euler equations using the Finite Volume Method requires that boundary conditions be specified for the three variables i.e. u, v and p at each boundary. Conditions for u, v and p at the free surface are obtained by manipulating the above described equations.

Differentiating the DBC once with respect to time and applying the KBC, we obtain the following equation:

$$\frac{\partial^2 \phi}{\partial t^2} + gv = 0 \tag{5.18}$$

Differentiating the above equation further with respect to y, we get:

$$\frac{\partial^2}{\partial t^2}\left(\frac{\partial \phi}{\partial y}\right) + \rho g \frac{\partial v}{\partial y} = 0 \tag{5.19}$$

Using the definition that $v = \frac{\partial \phi}{\partial y}$, and exploiting the fact that for a wave, the velocity v is of the form $v = Ae^{i\omega t}$ (where A is a parameter independent of time and ω is the frequency of the wave), we obtain the final form of the boundary condition for the vertical velocity at the free surface:

$$\frac{\partial v}{\partial y} = \frac{\omega^2}{g}v \tag{5.20}$$

This gives us a mixed-type boundary condition for the first derivative of v in terms of the wave frequency (ω). The unknown velocity is present on both sides of the equation, i.e. in the backward difference approximation of the first derivative as well as explicitly on the right hand side.

Similarly, we can obtain the following condition for the first derivative of u velocity with respect to y.

$$\frac{\partial u}{\partial y} = \frac{\omega^2}{g}u \tag{5.21}$$

In order to get a boundary condition for pressure, we start with the fact that the pressure at the free surface is zero. Pressure at a depth z would be $p = p_{Static} + \rho g z$. For $z = \eta$, we get $p = \rho g \eta$. From linear theory, for a small values of η, this condition can be applied at $z = 0$. Therefore, at $z = 0^1$, we have:

$$p = \rho g \eta \tag{5.22}$$

Differentiating the above equation with respect to time, we have:

$$\frac{\partial p}{\partial t} = \rho g v \tag{5.23}$$

Therefore knowing the vertical velocity and pressure at a previous time step, the pressure at the next time step can be determined.

In the problem, the wavelength of the wave, L_o, is the characteristic length; the time period T is the characteristic time; and the wave velocity, c given by $c = \frac{L_o}{T} = \sqrt{\frac{g L_o}{2\pi}}$ is the characteristic velocity. The Euler equations as well as the boundary conditions are made non-dimensional with respect to these references.

Solution

Figure 5.10 shows the velocity distribution at the free surface. It is confirmed that a wavelength of 1.0 non-dimensional units is obtained (as the wavelength, L_o is used to non-dimensionalize the Euler equations). Figure 5.11 shows the exponential decay of the velocity with depth.

---

[1] This can be verified by using the expression for the pressure under a wave, $p = \rho g(\eta e^{kz} - z)$, where k is the wave number. For $z = 0$, this reduces to the above form

Wave profile and Axial velocity contours

t = 0

L_o=1.0
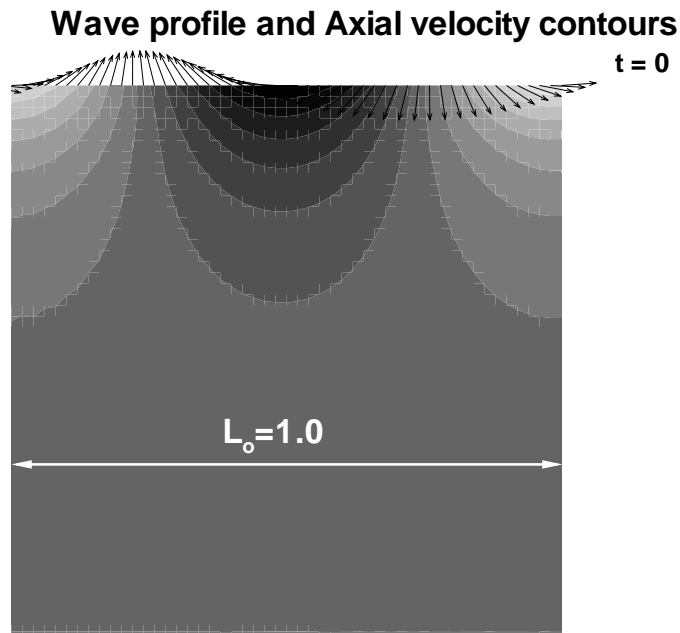
Figure 5.10: Free surface velocity distribution obtained using the numerical wave-maker

5.1.5 2D Straight Channel flow: Comparison with FLUENT

The 2D straight channel flow problem is used in order to validate the unsteady viscous solver developed. This is known as the pressure driven Couette Flow problem. Flow through a straight 2D channel is considered, with a uniform inflow specified at the inlet. For the problem, $L/H = 5$, where L is the length of the channel and H is the channel height. The Reynolds number is defined in terms of the inflow velocity and the height of the channel ($Re = \frac{U_{Inflow}H}{\nu}$). The results presented here are for a run with $Re = 100$.

The boundary conditions applied on the four boundaries are summarized below.

101

Decay of velocity with depth
t = 0

u ~10^{-2}
v ~10^{-4}
at depth = $L_o/2$
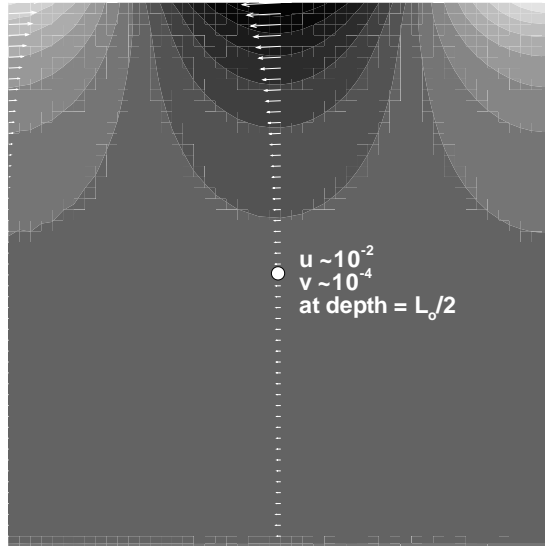
Figure 5.11: Decay of velocity with depth

- Inlet: At the inlet, the inflow is specified as a uniform x-direction velocity[2] The same boundary condition is applied in FLUENT, and a consistency is maintained. The vertical velocity is specified as zero at the inlet, and the pressure is obtained from the inner nodes.

$$\frac{\partial^2 p}{\partial x^2} = 0, \quad v = 0 \tag{5.24}$$

- Outlet: Both the velocity components are obtained from the inner nodes. The condition of the first derivative with respect to x being zero implies that the

---

[2]This can lead to some convergence problems, and a better approximation would be to specify a parabolic velocity profile (fully developed flow through a pipe, see [Panton 1996]). This problem is overcome by having finer grid spacing close to the entrance.

flow profile is no longer changing in the x- direction, which is true for a long channel. A reference pressure ($p = 0$) is also specified.

$$\frac{\partial u}{\partial x} = 0, \ \frac{\partial v}{\partial x} = 0, \ \ p = 0 \tag{5.25}$$

- Walls: The pressure on the walls is determined from the inner nodes. The first derivative is treated in the same manner as shown in Equation 5.3. A no slip condition is specified at the wall boundaries as a Navier-Stokes solver is being used.

$$\frac{\partial p}{\partial y} = 0, \ \ u, \ v = 0 \tag{5.26}$$

The results from the unsteady Navier-Stokes solver are compared to those from NS2D, a steady 2D Navier-Stokes solver (as this is essentially a steady problem, we obtain the steady-state solution by allowing the unsteady solver run for a sufficient period of time) and unsteady results from FLUENT (a commercial CFD code). The FLUENT run conditions are summarized below:

- 2D, unsteady, 1st order implicit in time, SIMPLE

- $\Delta t = 0.1, \ 100$ time steps

- Re=100

The grid used in the problem is shown in Figure 5.12. Finer cells are used near the inlet as ideally a parabolic profile needs to be specified at the inlet (while a uniform inflow is actually specified).

The converged solution obtained from the unsteady Navier-Stokes solver is shown in Figure 5.13. As is seen from the velocity vectors, a parabolic profile is

$\frac{\Delta p}{L}_{Analytical}$	$\frac{\Delta p}{L}_{Computational}$
0.02 (for Re=100	0.0204322

Table 5.2: Comparison of the analytical and computed values of $\frac{\Delta p}{L}$ for the 2-D channel flow problem

obtained at the outlet. This means that the channel is long enough for the flow to fully develop. In Figure 5.14 and 5.15, the axial velocity profile at the boundary and the pressure at the bottom wall as obtained from the three methods are compared. These match very well for the three solvers.

Another check that is performed is comparing $\frac{\Delta p}{L}_{Analytical}$ with $\frac{\Delta p}{L}_{Numerical}$. In fully developed Couette flow, the pressure gradient is constant and is related to the mass flow rate, Q, by the Equation 5.27 (refer [Panton 1996] for derivation). In this problem a parabolic profile $u(y) = y - y^2$ is specified at the inflow. The flow rate, Q can be determined by integrating the velocity over the height ($Q = \int_0^1 u(y)dy$). Knowing Q and Re, the analytical value of $\frac{\Delta p}{L}$ can be determined. The analytical and computed values are compared in Table 5.2. These values match very well.

$$Q = \frac{Re}{12}\frac{\Delta p}{L} \qquad (5.27)$$

5.2 Convergence Studies

Convergence studies are performed for the developed numerical scheme. The two important parameters in this problem are cell size and time step size. These tests help in ascertaining appropriate values of various parameters, i.e. parameter values which give the expected level of accuracy for minimum run time. The convergence

Grid used for 2D straight channel problem
(50x20 cells)
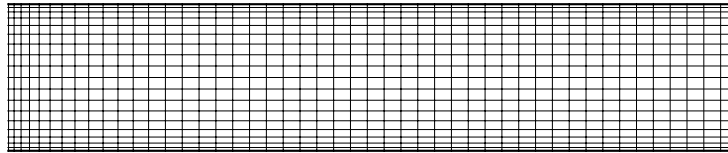
Non-uniform cell spacing near the inlet

Figure 5.12: Grid used for the 2D straight channel problem (50×20 cells)

NS Solver, Unsteady, Re=100

σ_4=1.0, 50x20 cells (non-uniform)
Δt=0.001, 20000 timesteps
L/H=5

Inlet
   u=1
   v=0
   ∂^2p/∂x^2=0

P: 0   1   2   3   4   5
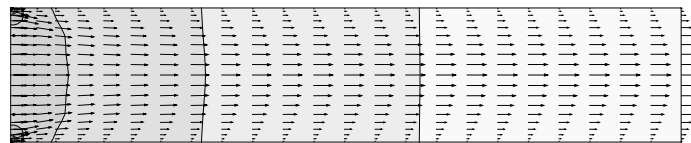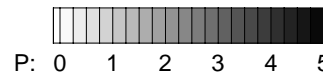
Top and Bottom walls
   u=0
   v=0
   ∂p/∂y = 0
Outlet
   ∂u/∂x=0
   ∂v/∂x=0
   p=0

Figure 5.13: Converged solution for the 2-D channel problem obtained using the unsteady N-S solver
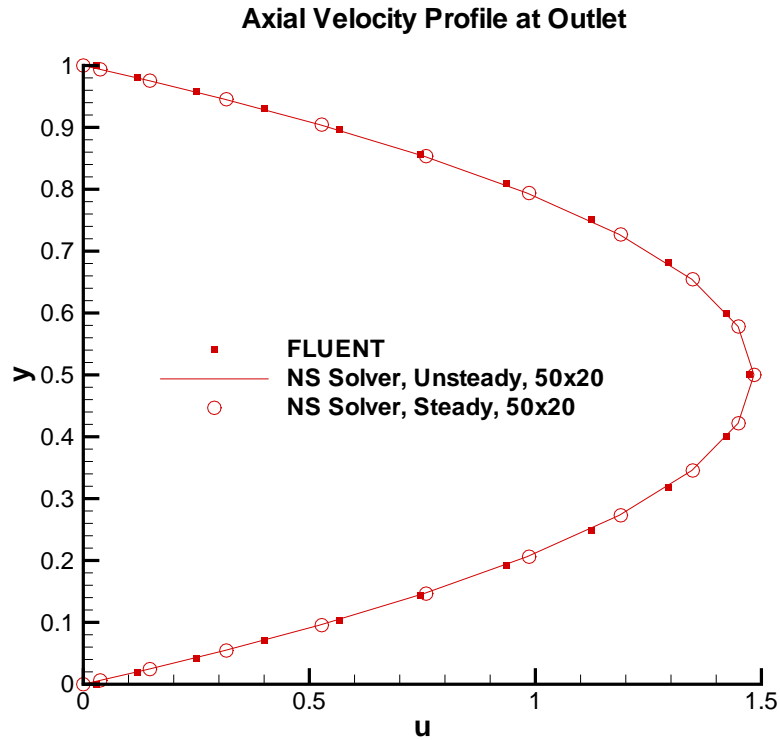
Figure 5.14: Comparison of 2D channel outlet velocity profile for three different methods - the steady N-S solver, the unsteady N-S solver and FLUENT

studies are performed using the oscillating flow problem as described in Section 5.1.2.

5.2.1 Convergence with Δt

In order to study the convergence with Δt, all other parameters are kept fixed and the value of Δt is varied. The convergence study is performed using a rectangular domain (120×60 cells). The total time for the run is kept fixed as $100T$. For $\Delta t = 0.01$, this would mean 10000 iterations while for $\Delta t = 0.001$, 100000 iterations.
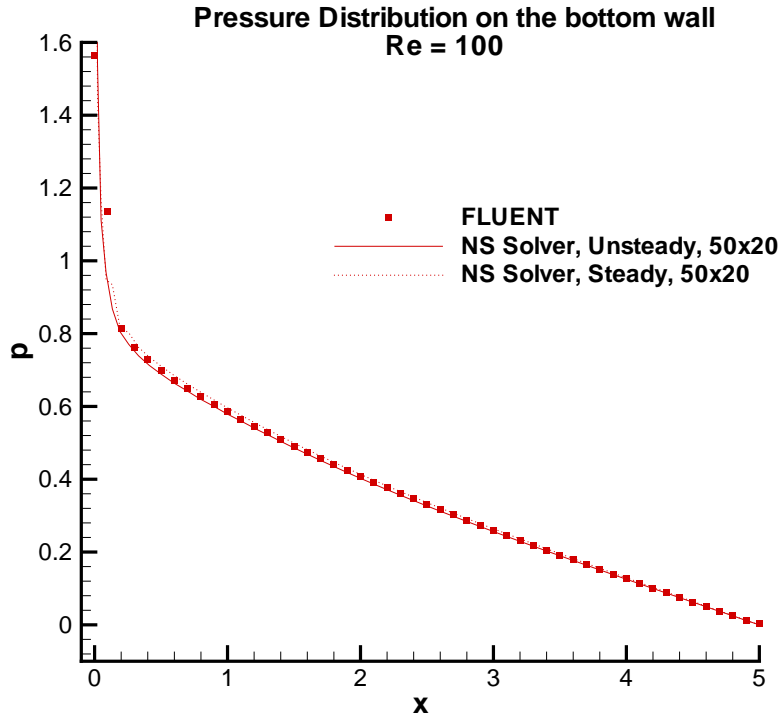
Figure 5.15: Comparison of 2D channel bottom pressure for three different methods - the steady N-S solver, the unsteady N-S solver and FLUENT

The value of the partial derivative of the pressure with respect to x is compared for time $t = 88T$ seconds (see Table 5.3). It should be noted that for the specified time instant, the expected value of $\frac{\partial u}{\partial t} = 0.785398$.

5.2.2 Convergence with Number of Cells

A similar convergence study is performed for the number of computational cells. For this study, Δt is kept fixed as 0.001 and a comparison of the $-\frac{\partial p}{\partial x}$ is shown in Table 5.4.

107

Δt	$-\frac{\partial p}{\partial x}$	Error in v velocity
0.01	0.80113	12 %
0.001	0.785052	0.0017 %

Table 5.3: Convergence of computed values of $-\frac{\partial p}{\partial x}$ and the error in v velocity for different values of Δt

Number of cells	$-\frac{\partial p}{\partial x}$	Error in v velocity
60x30	0.78324	0.00015 %
60x30 (uniform)	0.7791	0.09 %
120x60	0.785052	0.0017 %

Table 5.4: Convergence of computed values of $-\frac{\partial p}{\partial x}$ and the error in v velocity for different grid sizes

5.3 Flow past a Flat Plate

This section discusses the use of the developed two-dimensional unsteady Euler solver to model the oscillating flow past a flat plate. Modeling of the separated flow past the flat plate would provide a simplified visualization of separated flow past bilge keels. The strongly separated flow past bilge keels results in improved mitigation of the roll motions. Yeung, in [Yeung et al. 2000], concludes that the viscous shear stress is found to be of secondary importance in strongly separated flow and the pressure force dominates.

The results are obtained for different values of the Keulegan-Carpenter number. The drag and inertia coefficient values are compared to those presented in [Sarpkaya and O'Keefe 1995]. For a Keulegan-Carpenter number of 1.0, the Euler equation results are compared to the Navier Stokes solver results. Comparison of results from the viscous solver with those from an Euler solver would help quantify

the error introduced by using an inviscid solver to model the separated flow.

5.3.1 Oscillating Flow past a Flat Plate

In order to analyze the flow past a flat plate, an oscillating flow is specified and the separated flow that develops is studied. A domain size of $0 \leq x \leq 12$, $0 \leq y \leq 6$ with 120x60 uniform cells and $\Delta t = 0.001$ sec is used for this run. The flat plate is taken to be one computational cell thick and the height of the plate is taken to be the reference length used to non-dimensionalize the equations. The grid used and the boundaries are described in Figure 5.16. The domain boundary conditions are summarized below:

- Upstream and Downstream boundaries: A sinusoidal x-direction velocity is specified at the left and right boundary of the domain. The second derivative of pressure and the first derivative of the y-direction velocity are specified to be zero i.e the values of these variables on the boundary are obtained from the inner nodes.

$$u = -U_m cos(\omega t), \quad \frac{\partial v}{\partial x} = 0, \quad \frac{\partial^2 p}{\partial x^2} = 0 \qquad (5.28)$$

- Top boundary: On the top boundary of the domain, the first derivative of p with respect to y is specified to be zero. In other words, the value of the pressure on the boundary is the same as the pressure value on the inner node. The vertical velocity is specified as zero and the horizontal velocity as the sinusoidal function.

$$\frac{\partial p}{\partial y} = 0, \quad u = -U_m cos(\omega t), \quad v = 0 \qquad (5.29)$$

109

- Bottom boundary: The symmetry boundary condition is applied on the bottom boundary, with the first derivative of the u velocity with respect to y taken to be zero and the vertical velocity specified as zero. The first derivative of pressure with respect to y is taken to be zero.

$$\frac{\partial u}{\partial y} = 0, \ \frac{\partial p}{\partial y} = 0, \quad v = 0 \tag{5.30}$$

- On the plate: Applying the Kinematic boundary condition on the plate surface, we get the boundary conditions shown below. In the Euler solver, the free-slip condition is applied i.e. only flow parallel to the plate is allowed (that is the vertical velocity) while the velocity component normal to the plate (u velocity) is specified as zero. On the other hand, for the Navier-Stokes solver, the no-slip boundary condition is applied. This requires that both velocity components are zero on the nodes on the plate surface. The pressure on the disk is obtained by extrapolating from two adjoining nodes. For the nodes representing the tip of the plate, the pressure is taken as the average of the pressure obtained from extrapolating the pressure from the two adjoining nodes in the x- and y-directions.

  - Euler solver - free-slip boundary condition

$$u, \ \frac{\partial v}{\partial x} = 0, \quad \frac{\partial^2 p}{\partial x^2} = 0$$

  - Navier-Stokes solver - no-slip boundary condition

$$u, \ v = 0, \quad \frac{\partial^2 p}{\partial x^2} = 0$$

110
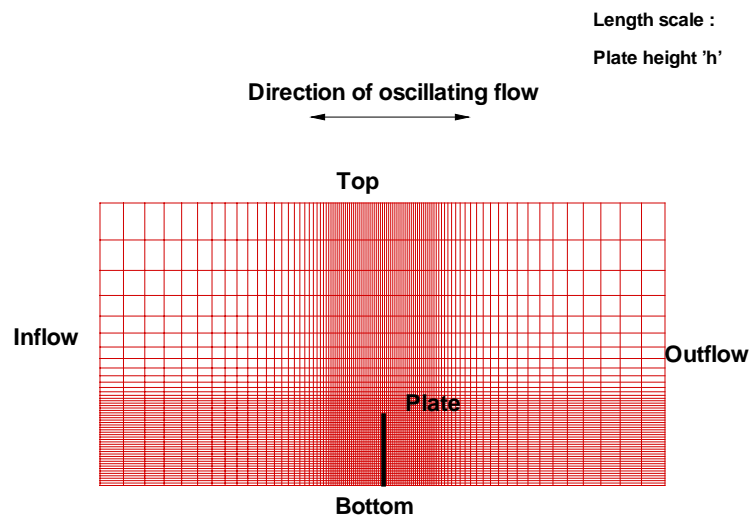
Figure 5.16: Oscillating flow past a flat plate: grid used and boundary definitions

5.3.2 Determination of the Drag and Inertia Coefficients

The force exerted on a plate can be expressed by the Morison's equation as follows [Sarpkaya and O'Keefe 1995]:

$$\frac{2F}{\rho h w U_m^2} = -C_d|cos\theta|cos\theta + C_m\frac{\pi^2}{K}sin\theta \tag{5.31}$$

where F is the force acting on the plate; ρ is the density of the fluid; h, the height of the plate; w, the width of the plate; U_m the amplitude of the oscillating fluid velocity characterized by $U = -U_m cos\theta$; $\theta = \frac{2\pi t}{T}$ where T is the period of oscillation; and C_d and C_m, the Fourier-averaged drag and inertia coefficients given by

$$C_d = -\frac{3}{4}\int_0^{2\pi}\frac{F(\theta)cos\theta}{\rho h w U_m^2}d\theta \tag{5.32}$$

$$C_m = -\frac{2K}{\pi^3}\int_0^{2\pi}\frac{F(\theta)sin\theta}{\rho h w U_m^2}d\theta \tag{5.33}$$

The coefficients for the plate held normal to the flow depend on the Keulegan-Carpenter number, $K = \frac{U_m T}{h}$ and the Reynolds number, $Re = \frac{U_m h}{\nu}$.

In order to compare results with [Sarpkaya and O'Keefe 1995], the flat plate is assumed to be two-dimensional i.e. $w = 1$. Using h as the reference length, U_m as the velocity scale and time period T as the time scale, we obtain non-dimensionalized Euler equations similar to Equation 3.4:

$$\frac{1}{K}\frac{\partial \vec{U}}{\partial t} + \frac{\partial \vec{F}}{\partial x} + \frac{\partial \vec{G}}{\partial y} = \vec{Q} \tag{5.34}$$

where the column matrices are defined same as in Equation 3.5 and K is the Keulegan-Carpenter number.

112

Equations 5.32 and 5.33 above can also be written in the non-dimensional form:

$$C_d = -\frac{3}{4} \int_0^{2\pi} \hat{F}(\theta) cos\theta d\theta \qquad (5.35)$$

$$C_m = -\frac{2K}{\pi^3} \int_0^{2\pi} \hat{F}(\theta) sin\theta d\theta \qquad (5.36)$$

where $\hat{F}(\theta)$ is the non-dimensional force function over one time period. The force can be obtained by numerically integrating the pressure on the plate. As Δt used in the problem is small ($\Delta t = 0.001$) the drag and inertia coefficients can be estimated using the trapezoidal rule.

Solution

The solution obtained using both the unsteady Euler and unsteady version of NS2D is presented in this section. The same grid and run conditions are used for both the solvers. The Navier-Stokes solver differs only in terms of the body boundary conditions (as described in the previous section) and the need to specify a Reynolds number. In order to obtain results consistent with the experiment performed by [Sarpkaya and O'Keefe 1995], a Reynolds number of $Re = 1035$ is used. The comparison between the two approaches is performed for a Keulegan-Carpenter number, $K = 1.0$. Figures 5.17 and 5.18 show the x-direction velocity contours and the streamlines. It is observed that the Navier-Stokes solver predicts tighter vortices being shed. This shed vortex pattern can be compared with Figure 3a in [Sarpkaya and O'Keefe 1995]. A pair of counter-rotating vortices is formed and this convects away in the diagonal direction, either to the left or the right side of the plate. A more important outcome is the comparison of forces predicted by the two solvers.

113

As is seen in Figure 5.19, the force history predicted by both solvers is comparable, except for a small phase difference. This difference is negligible when computing the coefficients.

The drag and inertia coefficients can be computed from the force history (using Equations 5.35 and 5.36). These coefficients, obtained using the Euler solver for a range of Keulegan-Carpenter numbers, are presented in Figures 5.20 and 5.21. A direct comparison with results published by [Sarpkaya and O'Keefe 1995] is difficult as in the paper, the coefficients are plotted on a log scale. For a Keulegan-Carpenter number of 1.0, the present method gives $C_d = 13.7$ and $C_m = 1.1$ and the Navier-Stokes solver gives $C_d = 14.6$ and $C_m = 1.03$. For the same Keulegan-Carpenter number, [Sarpkaya and O'Keefe 1995] experimentally obtain values of $C_d = 15.5$ and $C_m = 1.1$ (see Figures 1 and 2 in [Sarpkaya and O'Keefe 1995]. In general, it can be seen that the values obtained and trends observed are comparable.

5.4   Motions of a Hull

This section provides a general background for the problem of a body undergoing periodic motions at the free surface of a fluid. Flow is simulated past a rectangular FPSO hull subjected to forced heaving and rolling at the free surface. The draft of the hull is taken to be the reference length used to non-dimensionalize the Euler equations. The hull is subjected to heave or roll motion by specifying an appropriate sinusoidal exciting function and by requiring that the free-slip boundary condition be satisfied. The amplitudes of motion are varied and the effect on the hydrodynamic coefficients studied. The solution is considered assuming the flow is two-dimensional. A large solution domain is considered in order to ensure that the deep water condition is satisfied as well as to allow for the solution to develop fully.
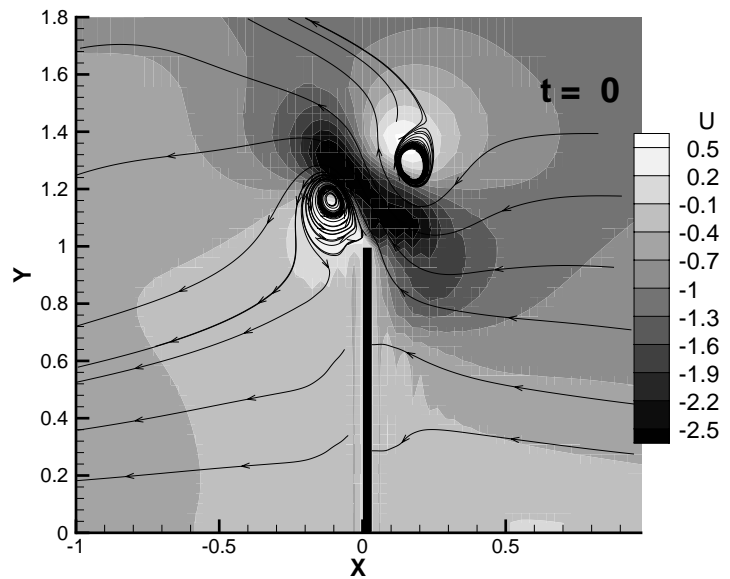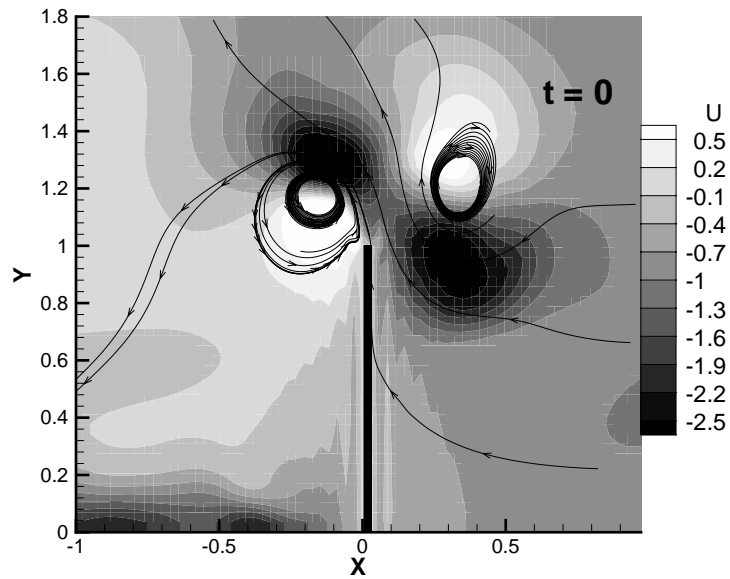
Figure 5.17: Axial velocity and streamlines predicted by the Euler solver (top) and the Navier-Stokes solver (bottom) at time instant $t = 0$, for oscillating flow past a flat plate

115
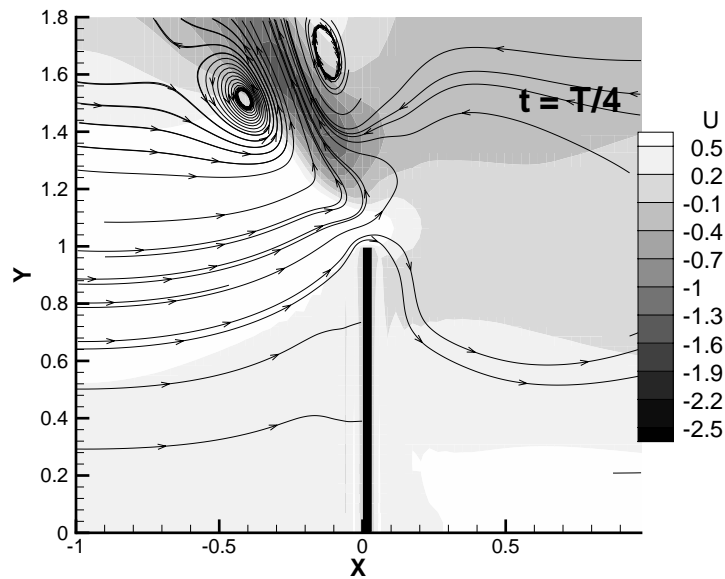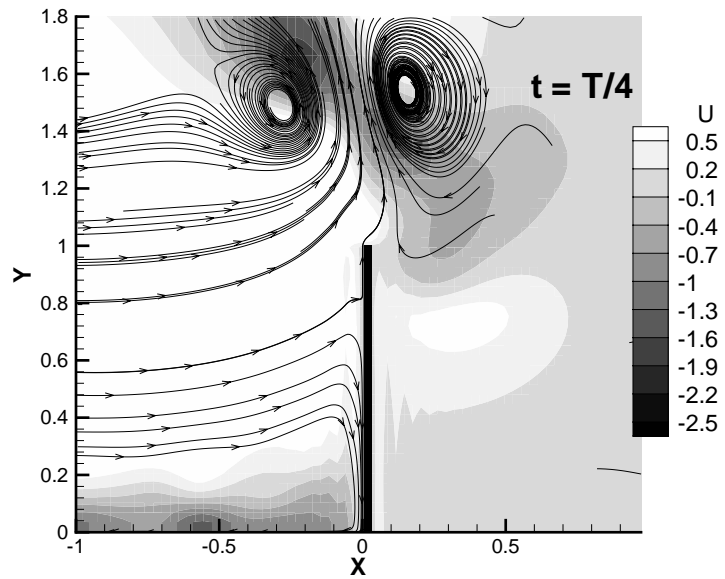
Figure 5.18: Axial velocity and streamlines predicted by the Euler solver (top) and the Navier-Stokes solver (bottom) at time instant $t = \frac{T}{4}$, for oscillating flow past a flat plate
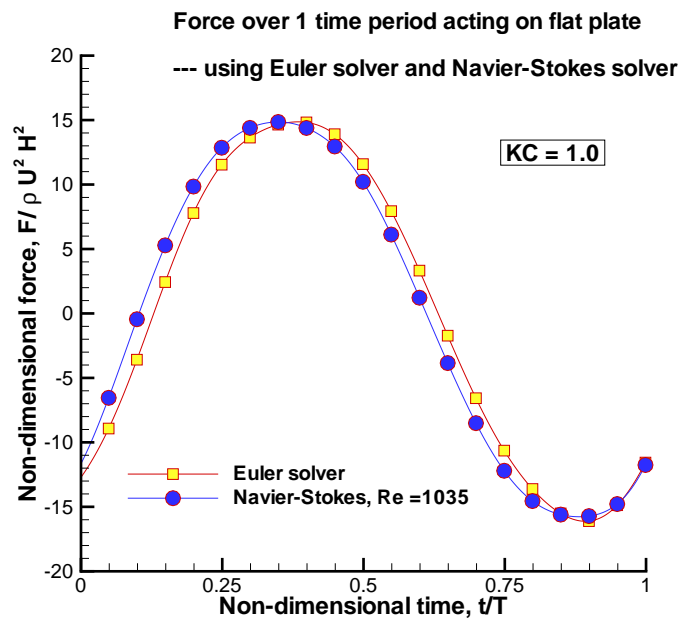
Figure 5.19: Comparison of force history (over one time period) predicted by the Euler solver and the Navier-Stokes solver, for oscillating flow past a flat plate
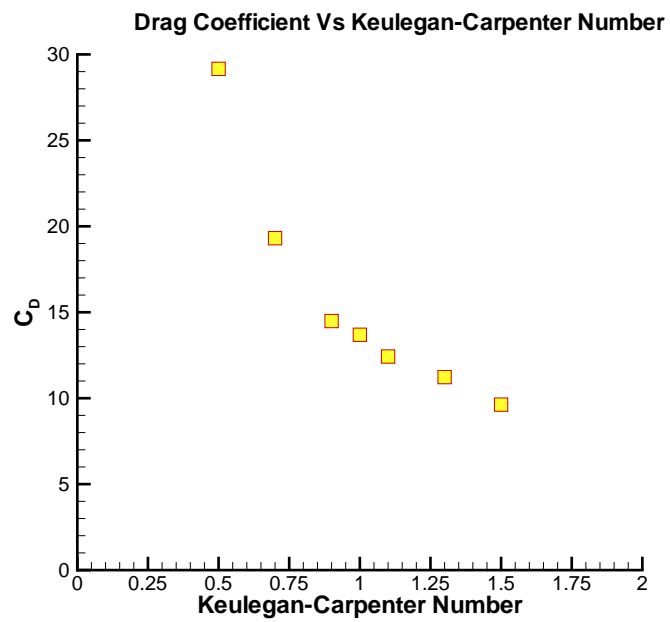
Figure 5.20: Drag coefficients obtained for the oscillating flow past a flat plate problem, for a range of Keulegan-Carpenter numbers, using an Euler solver (compare with Figure 1 in [Sarpkaya, 1995])
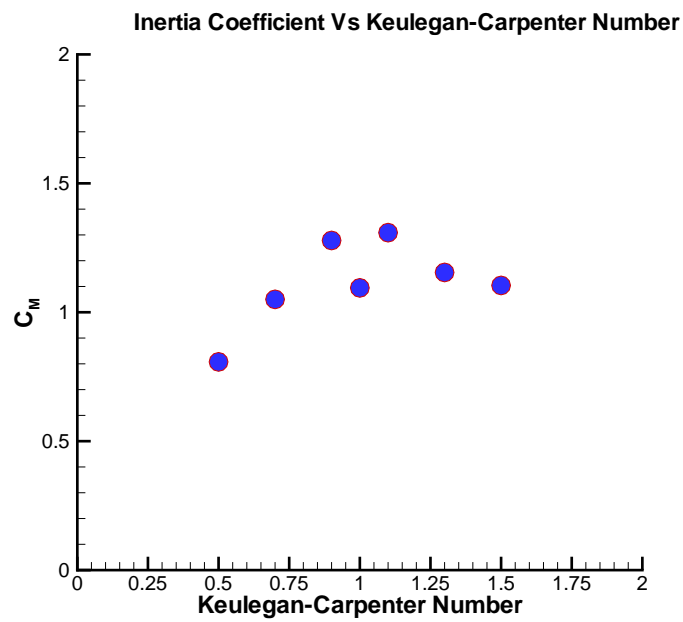
Figure 5.21: Inertia coefficients obtained for the oscillating flow past a flat plate problem, for a range of Keulegan-Carpenter numbers, using an Euler solver (compare with Figure 2 in [Sarpkaya, 1995])

5.4.1 Assumptions

The problem of a body undergoing motions at the free surface of a fluid can be complex and non-linear. In order to simplify the problem, certain assumptions need to be made. The basic assumption is that the flow is incompressible and the fluid is inviscid. Thus the flow is governed by the Euler equations.

In the present work, the motion of the hull is assumed known, while the source of the excitation (for example incident waves) is neglected. Therefore, we start of assuming that the hull is in continuous motion, with no decay in the amplitude of motion and the source of this motion is unimportant. This enables simplification in modeling of the problem.

Linear wave theory requires that the waves have "small" amplitudes and the amplitudes of the resulting motion be also "small".

The linear approach is used to satisfy the body boundary condition on the mean body position i.e. the body boundary condition is satisfied on the portion of the hull under the mean water surface, instead of satisfying it on the exact wetted portion of the hull as required by the non-linear approach.

Linearized conditions are assumed on the free surface. The linearized free surface boundary condition is applied on the undisturbed mean water surface instead of the incident wave surface.

The other assumptions are listed below:

- The vessel speed is assumed to be zero.

- Infinite water depth is assumed.

- Uncoupled roll and heave motions are considered.

FPSO Hull undergoing Roll Motion
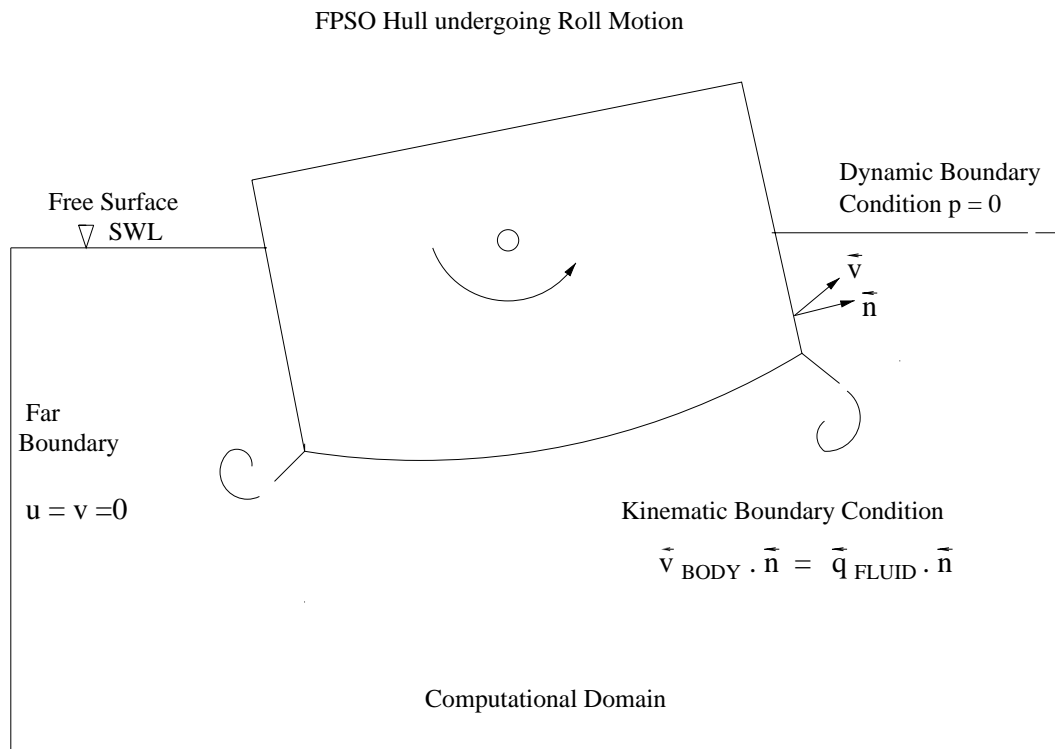
Figure 5.22: Description of boundary conditions on a hull moving at the free surface

- Computations have been done for the radiation problem with a free surface piercing body only.

- The roll axis is at the design waterline.

5.4.2 Coordinate system

The coordinate system used deviates from the typical system used in Naval Architecture (x positive towards the bow, y positive to the port). In this work, unless otherwise stated, the x-axis is considered going to the right along the bottom boundary of a rectangular domain. The y-axis extends from bottom to top. The origin is

121

located at the center of the domain, on the bottom boundary. Therefore, the grid and the hull form is symmetrical about the y-axis.

5.4.3 Grid and Geometry Details

A typical grid used for this problem is shown in Figure 5.23. The hull geometry i.e. the beam, the draft, the bilge radius and later the length of the bilge keels, form inputs for the grid generation program. It is also observed that the extent of the domain should be larger than the wavelength expected for a given Froude number. In non-dimensional units, the wavelength $L_o = \frac{2\pi}{Fn_D{}^2}$. For lower Froude numbers, the wavelength obtained is significantly larger than the draft of the hull. Having a grid with this extent is impractical as a large number of cells would be required to capture the wave profile. The study is, therefore, limited to Froude number values in the range $0.4 - 2.0$. These cover typical heave motion time periods observed in the field. Another consideration is that the results presented in [Newman 1977] are for deep-water. The extent of the grid in the y-direction should be such as to always satisfy the relation for deep-water, i.e. $\frac{d}{L_o} \geq 0.5$.

Figure 5.24 shows details of the bilge keel. The non-dimensional bilge-keel depth (non-dimensionalized by the beam, B, of the cross section), K_D is varied and the effect of the bilge-keel depth on the hydrodynamic coefficients is presented for the roll motion. A constant bilge radius of $0.02B$ is used for all the geometries considered.

5.4.4 Hull Forces

For a body moving in an infinite ideal fluid, the hydrodynamic forces and moments that develop can be expressed in terms of the added-mass coefficients m_{ij}, where

122
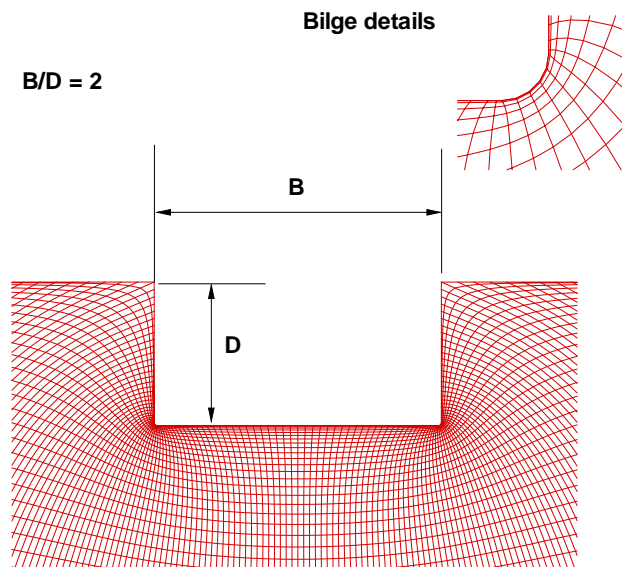
Figure 5.23: Grid used for studying the heave motion response for a rectangular hull form

2D Rectangular Hull Cross Section

Bilge radius

Bilge Keel

K_D : Bilge keel depth

•——— **Computational node**
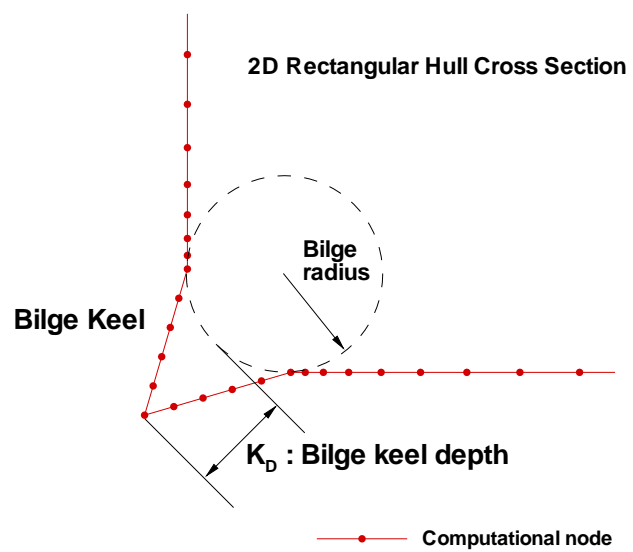
Figure 5.24: Bilge keel geometry details

both i and j refer to the six possible degrees of motion and m_{ij} is the added mass due to motion in direction j, resulting from a force in direction i. Consider a body undergoing small sinusoidal motions at the free surface. The six components of force and moments can be expressed as follows:

$$F_i = Re \sum_{j=1}^{6} \xi e^{i\omega t} f_{ij} \quad i = 1, 2, \cdots 6 \tag{5.37}$$

where

$$f_{ij} = -\rho \int_{S_B} \int \frac{\partial \phi_i}{\partial n} \phi_j dS$$

is the complex force in the direction i, due to a sinusoidal motion of unit amplitude in the j direction.

F_i can be alternatively be expressed in the form

$$F_i = -\sum_{j=1}^{6} (a_{ij} \dot{U}_j + b_{ij} U_j) \tag{5.38}$$

which is a decomposition of the sinusoidal force, associated with each mode of motion, into components in phase with the velocity and acceleration of the corresponding modes.

The coefficient a_{ij} is known as the *added-mass coefficient*, since it represents the force component proportional to the acceleration. The coefficient b_{ij} gives the force proportional to the body velocity; for this reason it is called the *damping coefficient*. The presence of such a force results from the generation of outward waves

125

in the free surface, due to motions of the body. These two coefficients are dependent on the the frequency of excitation.

The inviscid hull forces are obtained by integrating the pressure over the mean portion of the hull under the undisturbed water line. Once the force variation over one period is obtained, the least square approach can be used in order to solve Equation 5.38 for a known excitation U_j and $\dot{U}_j$ and the added-mass and damping coefficients can be determined.

5.4.5 Boundary Conditions

In order to accurately determine the force acting on the moving hull, it is essential to specify correct boundary conditions at all the boundaries. The free surface boundary conditions are applied as described in Section 5.1.4. The presence of the body creates a discontinuity in the free surface and a different set of boundary conditions need to be applied on the body. The velocity components are determined using the free-slip condition (i.e. only the velocity component tangent to the surface is allowed) and the kinematic boundary condition requiring that the normal component of the body velocity be equal to the normal component of the fluid velocity. The pressure on the body is extrapolated from internal nodes. The body velocity is specified by an appropriate sinusoidal function to describe heave and roll. For heave, only the vertical velocity of the body is considered to exist, and is described as a sinusoidal function with amplitude q_{yo}.

$$q_y(t) \;=\; q_{yo} sin(\omega t) \qquad\qquad (5.39)$$

In order to describe roll motion, the roll angle is considered as a sinusoidal

126

function.

$$\alpha(t) = \alpha_o sin(\omega t) \tag{5.40}$$

The angular velocity $\dot{\alpha}(t)$ can be determined by differentiating the above equation with respect to time. The tangential surface velocity is given by

$$q_{BODY} = \dot{\alpha}(t) \times r \tag{5.41}$$

where r is the distance of the point on the surface from the center of rotation.

Free surface-body intersection

The intersection point of the free surface and the body requires special treatment because of the drastic change in slope. The following conditions are applied at this point:

- The vertical velocity, v, and the pressure, p are obtained by extrapolating from two neighboring nodes on the free surface.

- Once the vertical velocity at the point is known, the x-direction velocity, u, can be determined by applying the Kinematic Boundary Condition, which requires that the velocity component normal to the body be zero.

5.5 Heave Motion

In this section, a heaving semi-circular hull form is considered first in order to ensure that the method can deal with body generated waves. Next, the hydrodynamic
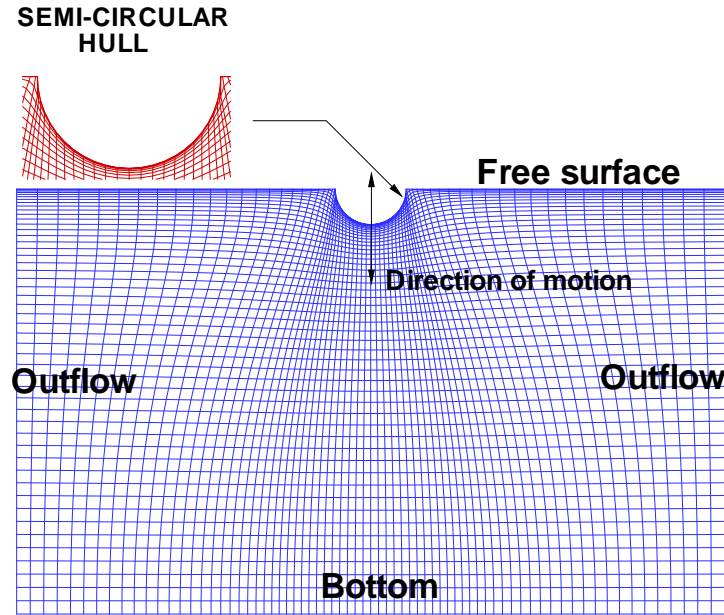
Figure 5.25: Grid used for studying the heave motion response for a semi-circular hull form

coefficients, i.e. the added-mass and damping coefficients, are determined for a rectangular hull, with a Beam/Draft=2, undergoing heave motion. These are computed for a range of Froude number values and the results obtained are compared with those presented in [Newman 1977].

5.5.1 Semi-Circular Hull form

Figure 5.25 shows a grid with a semi-circular hull, with diameter $D = 1.0$, located at the free surface. The equations are non-dimensionalized using the cylinder diameter, time period of heave motion and a velocity defined as $U^* = \frac{D}{T}$ as the reference length, time and velocity respectively. On non-dimensionalization, the Froude number ($Fn_D = \omega\sqrt{\frac{D}{g}}$) enters the equations and boundary conditions. This parameter

can be varied to simulate a large range of heave time periods.

The boundary conditions have been discussed in previous sections and are summarized below.

- Left and Right boundaries:

$$\frac{\partial(u,v,p)}{\partial x} = 0 \qquad\qquad (5.42)$$

- Bottom boundary:

$$\frac{\partial^2 p}{\partial y^2} = 0, \quad u, \ v = 0$$

- Free surface:

$$\frac{\partial u}{\partial y} = \frac{\omega^2}{g}u$$
$$\frac{\partial v}{\partial y} = \frac{\omega^2}{g}v$$
$$\frac{\partial p}{\partial t} = \rho g v$$

- Hull Boundary: Heave motion specified as $q_y = q_{yo}\sin\omega t$

$$\frac{\partial^2 p}{\partial n^2} = 0, \quad u, \ v \ \text{determined by applying KBC}$$

Results

For the case of a semi-circular hull, results are obtained for a Froude number $Fn_D = 1.5$. The free surface velocity distribution and the pressure contours for four different time instants are presented in Figure 5.26. It can be observed that the resulting

129
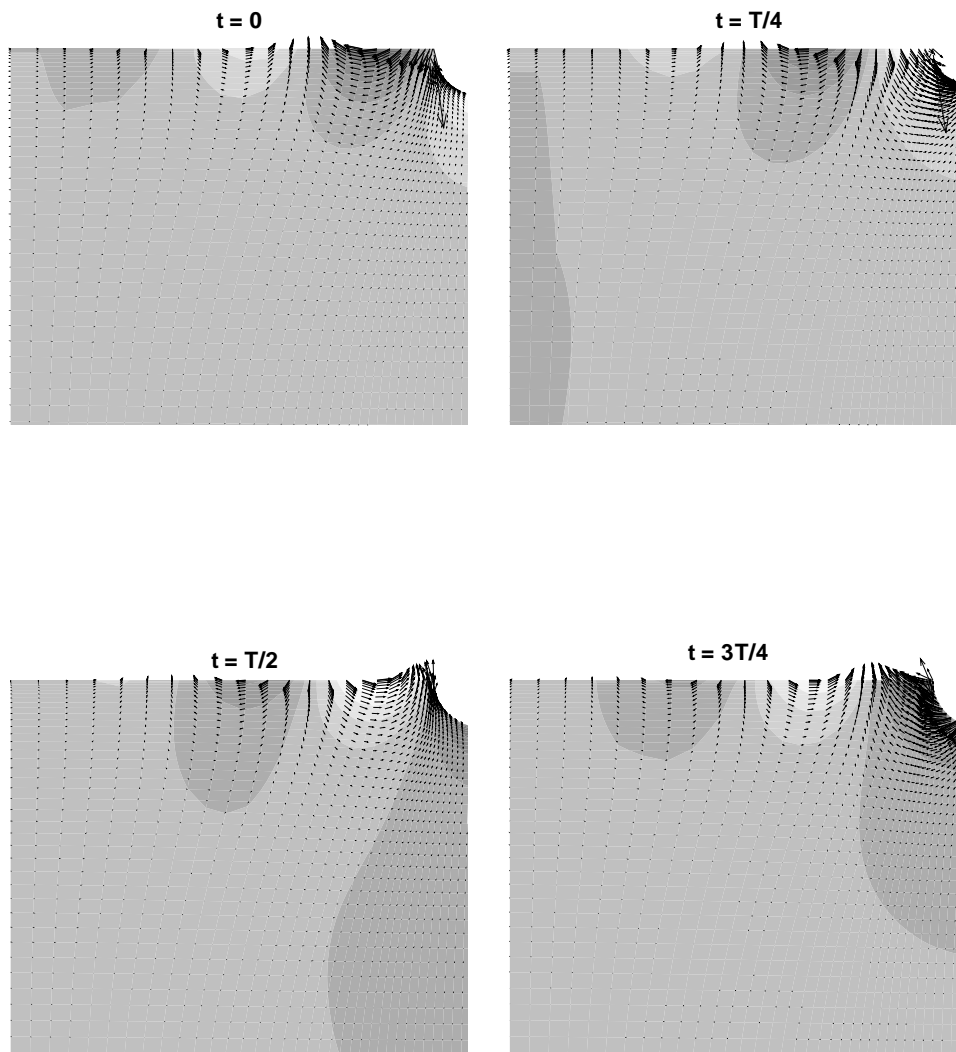
Figure 5.26: Free surface velocity distribution and pressure contours at time instants $t = 0$, $\frac{T}{4}$, $\frac{T}{2}$ and $\frac{3T}{4}$, for a heaving semi-circular hull
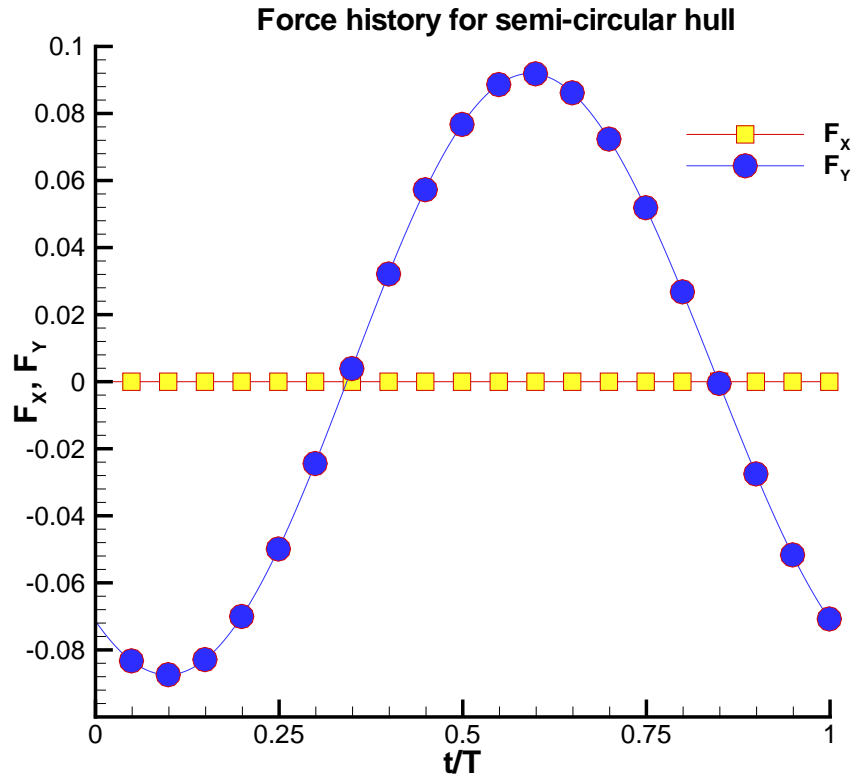
Figure 5.27: History of the vertical force acting on the semi-circular hull over one time period

surface wave radiates outwards. It should be noted that this solution is obtained from the solver without specifying an explicit radiation condition.

The force on the heaving hull is obtained by integrating the pressure on the hull surface. In the case of pure heaving, only the vertical force is of interest to us. This is shown in Figure 5.27, along with the x-direction force and the moment about z. Both the latter components are zero for the case of heaving.

5.5.2 Rectangular Hull form

In the case of heave, only the hull without the bilge keels is considered as results are available in [Newman 1977] to compare with. The grid details have already been presented in Section 5.4.3. The same boundary conditions are used in this problem as described for the heaving semi-circular hull.

Results

Many investigations have been carried out to compute the damping and added-mass coefficients of two-dimensional cylinder in deep water, as a function of frequency. For the two-dimensional case, [Vugts 1968] presented results for a family of heaving cylinders located on the free surface. The results have been revised and presented in [Newman 1977]. From these, a comparison of the coefficients is performed for a Beam/Draft ratio of 2.

Figure 5.28 shows the comparison of the added mass and damping coefficients obtained using the present solver and results presented in [Newman 1977], for a rectangular hull ($\frac{B}{D} = 2$) undergoing heave motion. As is shown in the figure, three different domain sizes and cell densities are used in order to ensure that the extent of the grid is larger than the wavelength and the deep-water condition is satisfied. The values of the hydrodynamic coefficients compare very well for Froude numbers greater than 0.5. For $Fn_D = 0.4$ the results deviate and this can be attributed to inadequate number of cells on the free surface. However, in order to maintain practical run times, a denser grid was not used.

Detailed results are presented for a typical case with $Fn_D = 1.5$ and heave velocity amplitude $q_{yo} = 0.05$. Figure 5.29 presents the velocity vectors and free surface at two different time instants, separated by $\frac{T}{2}$. The phase difference between
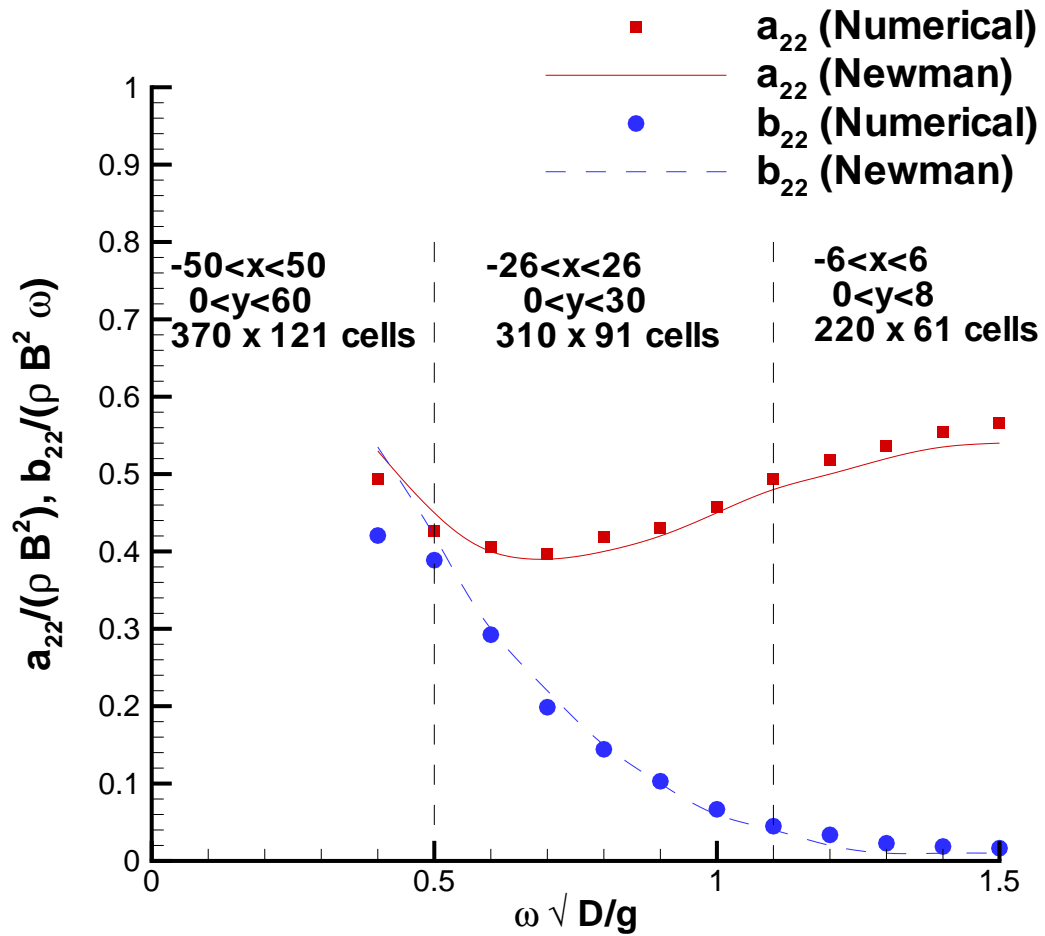
Figure 5.28: Comparison of added mass and damping coefficients for a rectangular hull ($\frac{B}{D} = 2$) undergoing heave motion in deep-water, obtained from the present solver with those presented in [Newman, 1977]

the radiated waves can be observed clearly.

Figure 5.30 shows the wave profiles of the outward radiating waves at three different time steps. (*Note: In the plot, the two axes are independent in order to highlight the wave profile*). As mentioned earlier, no explicit radiation boundary condition is specified on the free surface and the outward radiating waves are obtained from the solution.

The pressure contours at three different time instants ($t = 0$, $\frac{T}{4}$ and $\frac{T}{2}$) are shown in Figure 5.31. In order to obtain the force acting on the hull, the pressure is integrated over the the portion of the hull below the mean water line for every instant of time.

Figure 5.32 shows the three components of forces (F_x, F_y and M_z) over one time period. Of these, only the vertical force component is present and both horizontal force and moment are zero. This is expected as for every point on the boundary, there is a corresponding point where the pressure is in opposite direction, therefore cancelling the horizontal force. As mentioned earlier, the force includes only the pressure component of the force, with the viscous component being insignificant and therefore ignored.

From these typical results it is obvious that the present method could successfully simulate most of the main features of the flow due to a heaving cylinder.

5.5.3 Convergence Study

The convergence of the hydrodynamic coefficients with increasing number of computational cells is presented in this section. The three grid densities used are shown in Figure 5.33. Grid 'A' has 130×30 cells, Grid 'B' has 220×60 cells and Grid 'C'
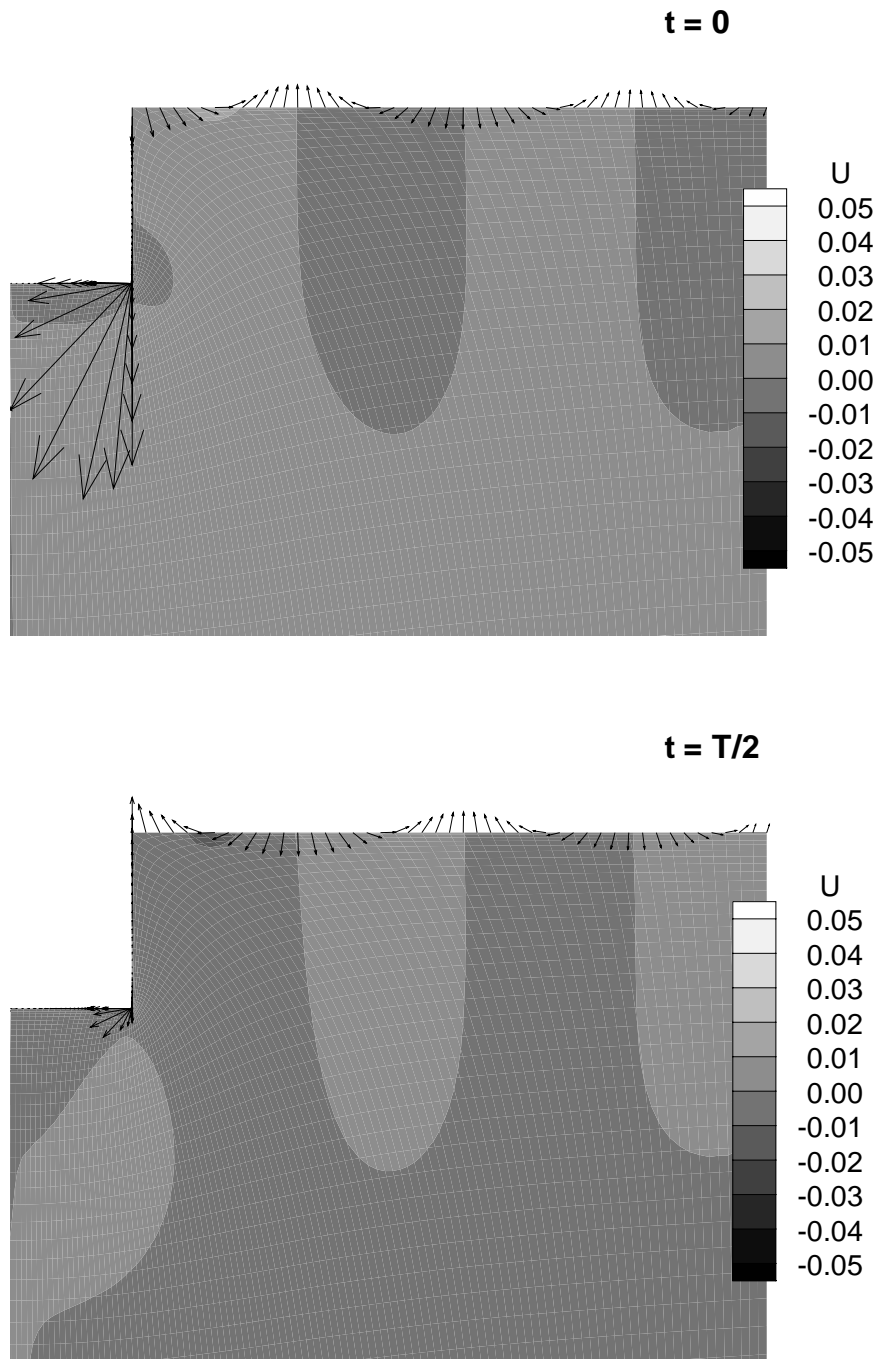
Figure 5.29: Free surface velocity distribution and axial velocity contours for $t = 0$ and $\frac{T}{2}$, for a rectangular hull undergoing heave motion ($\frac{B}{D} = 2$, $Fn_D = 1.5$, heave velocity amplitude = 0.05)
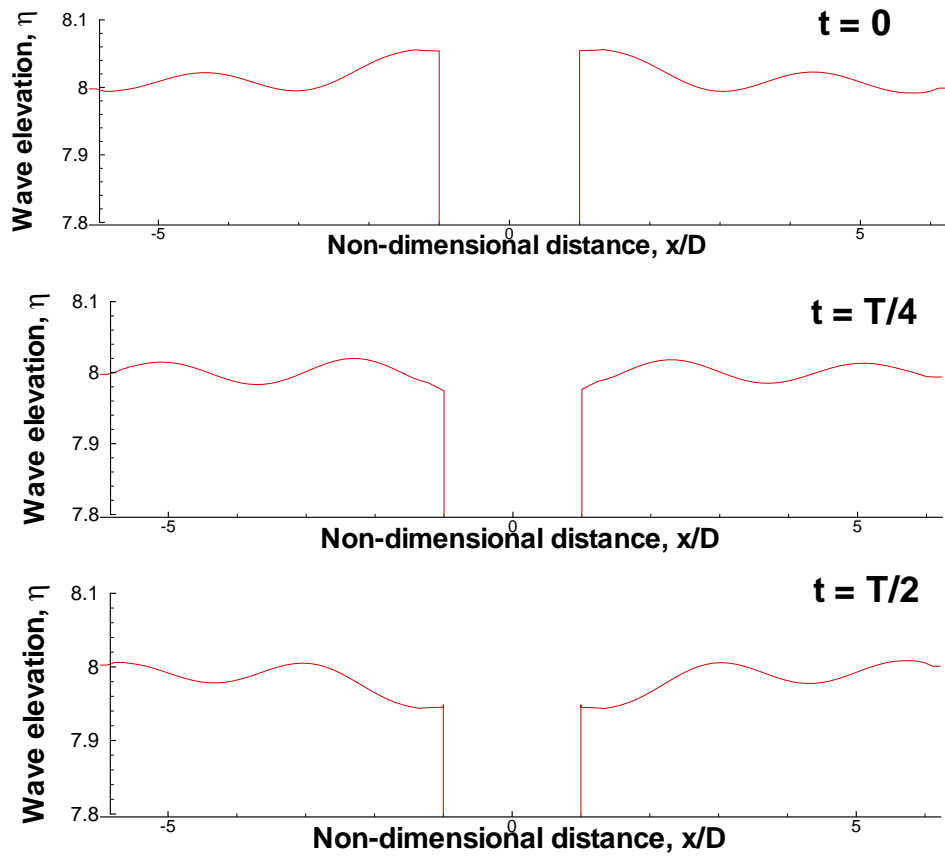
Figure 5.30: Wave profiles at three different time instants ($t = 0$, $\frac{T}{4}$ and $\frac{T}{2}$) for a heaving rectangular hull ($\frac{B}{D} = 2$, $Fn_D = 1.5$)
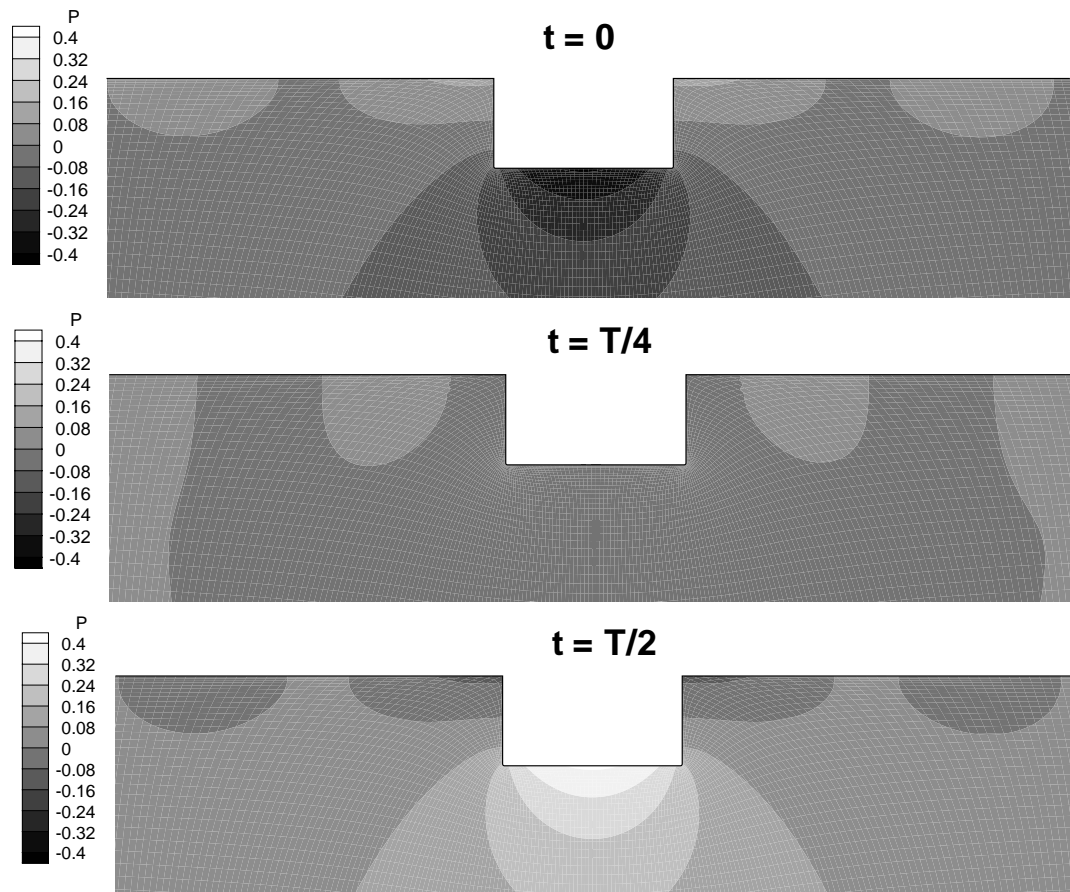
Figure 5.31: Pressure contours at three different time instants ($t = 0$, $\frac{T}{4}$ and $\frac{T}{2}$) for a heaving rectangular hull ($\frac{B}{D} = 2$, $Fn_D = 1.5$)
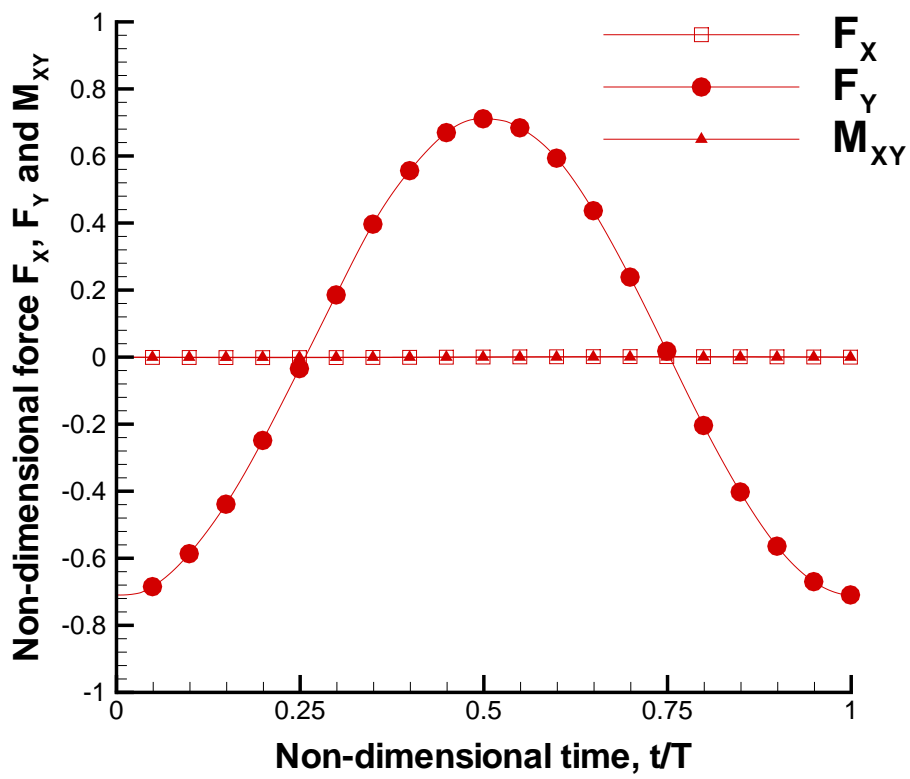
Figure 5.32: Force components F_x, F_y and M_z plotted over one time period, for a heaving rectangular hull ($\frac{B}{D} = 2$, $Fn_D = 1.5$)
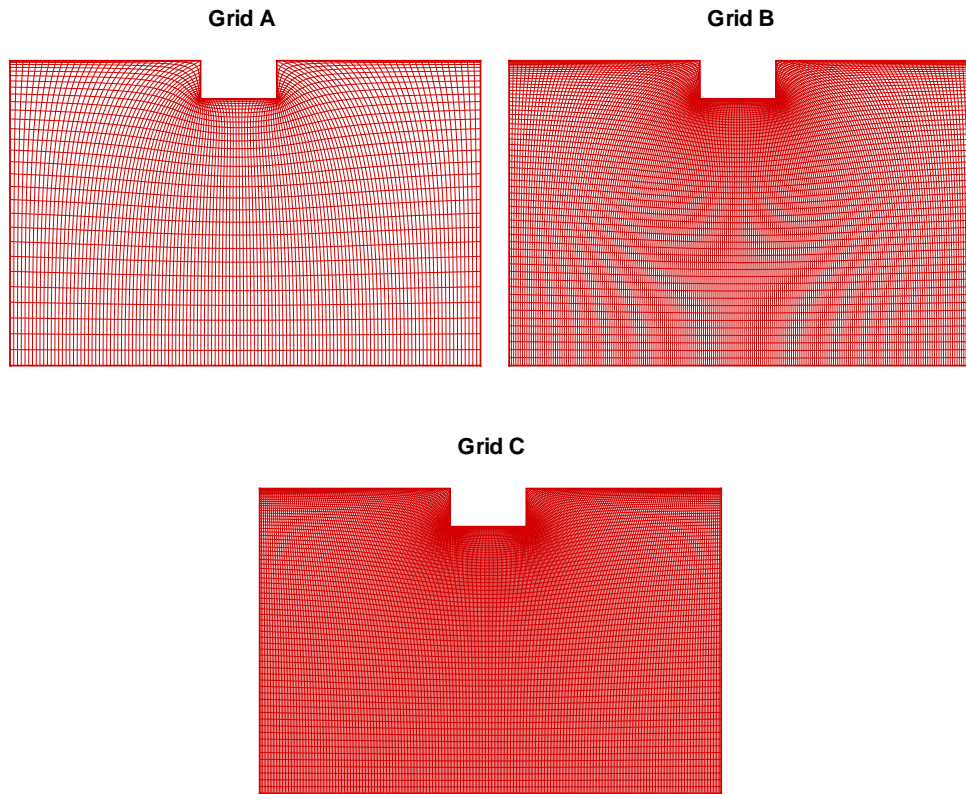
Figure 5.33: Grid densities used for convergence study: Grid A (130×30), Grid B (220×60) and Grid C (310×70) cells

has 310×70 cells.

Table 5.5 shows the added-mass and damping coefficients obtained for the three grids, for $Fn_D = 1.5$. It is seen that as the number of cells increases, the values of the coefficients converge. This is also demonstrated by Figure 5.34, where the time histories of the vertical forces is shown for the three grids.

Grid	a_{22}	b_{22}
130×30	0.5450221	9.8426165E-03
220×60	0.5661634	1.5587252E-02
310×70	0.5731037	1.6444225E-02

Table 5.5: Convergence of values of the heave added-mass and damping coefficients with increasing grid density
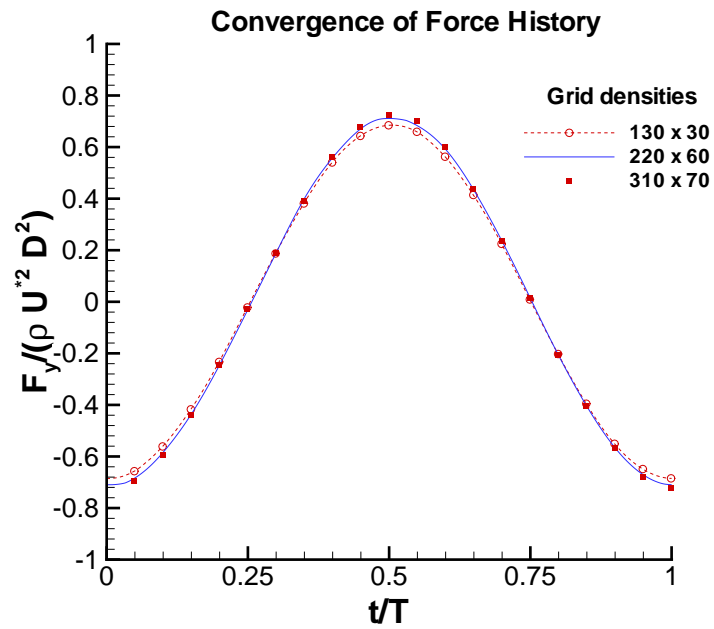
Figure 5.34: Convergence of force histories with increasing grid density

5.6   Roll motions

Ths section presents results for a 2D FPSO hull section undergoing roll motion. The motion is imposed on the mean position of the hull, in accordance with linear theory. The roll angle, α, at any time instant is given by $\alpha = \alpha_o sin(\omega \hat{t})$. In this expression, α_o is the amplitude of the motion (in radians or degrees); ω is the frequency of motion; and $\hat{t}$ is time. In the non-dimensional form, this reduces to $\alpha = \alpha_o sin(2\pi t)$ where t is time non-dimensionalized by the time period of motion, T.

The 2D hull section has the following dimensional features:

- $\frac{B}{D} = 2$

- Bilge radius $= 0.02B$

- Bilge keels located at an angle of 45° from the vertical side

- Bilge keel lengths, $K_D = 0, \ 0.02B, \ 0.04B$ and $0.06B$ are considered

- The hull geometry is located such that it is symmetrical about the y axis

- The cylinder is assumed to be rolling at the undisturbed free surface

The hydrodynamic coefficients for hull geometries with and without bilge keels are determined and compared in order to highlight the advantage offered by bilge keels as roll mitigation devices. The added-mass and damping coefficients are functions of the non-dimensional frequency (similar in form to the Froude number). This non-dimensional frequency or Froude number can be defined as $Fn_B = \omega\sqrt{\frac{B}{g}}$. It should be noted here that the definition of Fn_B differs from that used for the heave motion, where the draft (D) instead of the beam (B) was used.

141

5.6.1 Determination of Hydrodynamic Coefficients

For roll, according to linear potential theory, the hydrodynamic moment can be written as a linear combination of the inertia and damping terms.

$$M_z(t) = -a_{66}\ddot{\alpha} - b_{66}\dot{\alpha} \qquad (5.43)$$

where a_{66} is the roll added-mass coefficient; b_{66} is the roll damping coefficient; $\ddot{\alpha}$ and $\dot{\alpha}$ are the angular acceleration and velocity, respectively and these can be obtained by differentiating the expression of the roll angle, α, with respect to time. The linear hydrodynamic coefficients can be calculated by extracting the Fourier coefficient of the primary frequency over a period T. The following expressions are obtained for the coefficients:

$$\hat{a_{66}} = \frac{1}{\pi \alpha_o \omega} \int_0^T \hat{M}_z(t) sin(\omega \hat{t}) d\hat{t} \qquad (5.44)$$

$$\hat{b_{66}} = -\frac{1}{\pi \alpha_o} \int_0^T \hat{M}_z(t) cos(\omega \hat{t}) d\hat{t}$$

where the variables like $\hat{M}_z(t)$ and $\hat{t}$ are dimensional. In order to make the coefficients non-dimensional, a normalization similar to [Yeung et al. 2000] is performed.

$$a_{66} = \frac{\hat{a_{66}}}{4\rho \forall b^2} \qquad (5.45)$$

$$b_{66} = \frac{\hat{b_{66}}}{4\rho \forall b^2} \sqrt{\frac{b}{g}} \qquad (5.46)$$

$$\qquad (5.47)$$

where b is the half-beam of the hull and $\forall$ is the submerged sectional area.

Introducing the non-dimensional variables in Equation 5.44, the following expressions are obtained for the normalized coefficients:

$$a_{66} = \frac{1}{\pi^2 \alpha_o} \int_0^1 M_z(t) sin(2\pi t) dt \qquad (5.48)$$

$$b_{66} = -\frac{Fn_B}{\sqrt{2}\pi^2 \alpha_o} \int_0^1 M_z(t) cos(2\pi t) dt$$

Once the time history of the hydrodynamic moment has been obtained, the coefficients can be obtained by numerically integrating the moment, according to Equation 5.48, using the trapezoidal rule.

5.6.2 Results

The beam of the hull, B is used as the reference length. The solution domain extends from $-26.0B$ to $26.0B$ in the x-direction. This extent ensures that for the range of values of Fn_B chosen, the corresponding wavelengths are smaller than the domain. In the y-direction the solution domain extends from 0 to $30.0B$ in order to satisfy the deep-water condition. The hull geometry has a beam to draft ($\frac{B}{D}$) ratio of 2. The solution is obtained at the end of 10 time periods. The hydrodynamic coefficients are obtained for range of values of Fn_b, which is defined as $Fn_b = \frac{Fn_B}{\sqrt{2}}$[3]

Four different cases are considered. A hull with no bilge keel and hulls with bilge-keel depths $K_D = 2\%$, 4% and 6% of the beam are considered. The hull geometry without the bilge keel has a rounded corner (bilge radius $= 0.02B$). Results are presented for all four cases for a roll amplitude, α_o of 0.05 radians (2.85 degrees). For the hull without the bilge keels, the hydrodynamic coefficients are also presented

---

[3]Fn_b is the way the Froude number is defined in [Yeung et al. 2000]
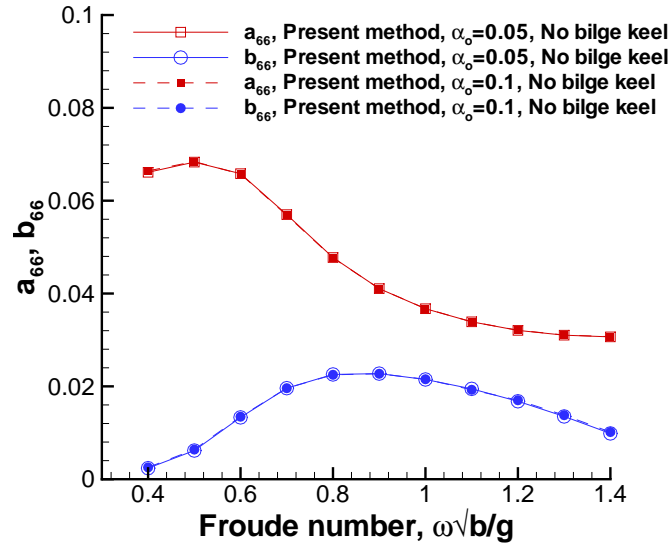
Figure 5.35: Comparison of roll added-mass and damping coefficients obtained for $\alpha_o = 0.05$ & $\alpha_o = 0.1$ (No bilge keel, $0.4 \leq Fn_b \leq 1.4$)

for an amplitude of 0.1 radians (5.73 degrees). This is done in order to demonstrate the linear behavior of the coefficients. Though the present method does not include viscous effects, it can capture the separated vortices being shed off the bilge keels. Therefore it is different from a potential flow solver which would allow the streamlines to follow the keel geometry, without capturing the separation. However, in the absence of the bilge keels, there is no vorticity shed and the present solver gives the inviscid hydrodynamic coefficients. As expected, these inviscid hydrodynamic coefficients are linear i.e. the values are independent of the roll amplitude. This has also been observed in [Yeung et al. 2000] for roll amplitudes less than 10 degrees. The hydrodynamic coefficients obtained for the two roll amplitudes are presented in Figure 5.35 for Fn_b ranging from 0.4 to 1.4. The coefficients are almost identical, thereby confirming their linear nature.

The numerical values of the added-mass and damping coefficients (for no
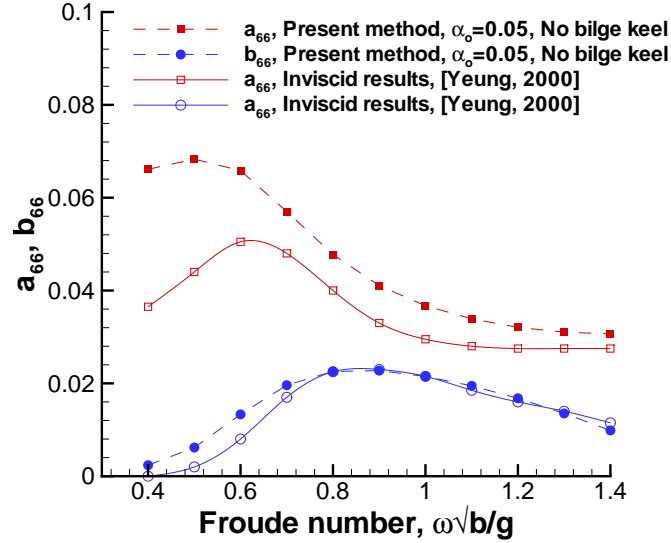
Figure 5.36: Comparison of roll added-mass and damping coefficients obtained from present method for $\alpha_o = 0.05$ and results presented in [Yeung et al. 2000] (No bilge keel, $0.4 \leq Fn_b \leq 1.4$)

bilge keel, $\alpha_o = 0.05$) are also compared with the 'inviscid' results presented in [Yeung et al. 2000]. As is seen in Figure 5.36, the damping coefficients obtained from the present method compare well with the results of [Yeung et al. 2000]. However, the present method predicts much higher values of the added-mass coefficients, especially for lower values of Fn_b.

In order to investigate the effect of the grid and domain size on the added-mass coefficients, the coefficients obtained using three different domain sizes and grid densities are compared in Table 5.6. It is seen that increasing the grid density or the domain size does not lead to a substantial change in the values of the coefficients. Therefore, the reason for the discrepancy in the results from the present method and the inviscid results presented in [Yeung et al. 2000] needs to be further investigated.

A typical time history of the hydrodynamic moment for $Fn_b = 0.8$ (4%

145

Grid	a_{22}	b_{22}
$-26B < x < 26B,\ 0 < y < 30B,\ 370 \times 100$	0.06582	0.01332
$-26B < x < 26B,\ 0 < y < 30B,\ 490 \times 150$	0.0649	0.01405
$-50B < x < 50B,\ 0 < y < 60B,\ 590 \times 200$	0.06416	0.01378

Table 5.6: Variation in values of the roll added-mass and damping coefficients for different grid densities and domain sizes (No bilge keel, $\alpha_o = 0.05$, $Fn_b = 0.6$)

bilge keel) is presented in Figure 5.37. The figure shows the convergence of the moment over 10 time periods. The force history over the last period is used to determine the hydrodynamic coefficients. In Figure 5.38, the hydrodynamic moment for the four hull geometries is presented over one time period and a value of $Fn_b = 0.8$. It is observed that with increasing bilge keel depth, the hydrodynamic moment increases and undergoes a phase shift. Equation 5.38 can be solved for using the approach described in Section 5.6.1. Expressions for $\dot{\alpha}$ and $\ddot{\alpha}$ can be obtained by differentiating the expression of the roll angle with respect to time.

The effect of the bilge keels is to increase the added moment of inertia and the radiation damping considerably. This is demonstrated in Figures 5.39 and 5.40, where the hydrodynamic coefficients for the four different hull geometries are compared. As expected, an increase in keel depth increases both the added-mass and damping coefficients over the entire range of Fn_b values. This goes to show the effectiveness of the bilge keels in roll motion mitigation.

Vorticity and Flow Patterns

Figure 5.41 details the converged flow patterns at four different time instants over one period of oscillation for the 6% bilge keel hull at $Fn_b = 0.8$. Strong vortices are created due to the bilge keels and these are shed as the keel moves in the opposite

146
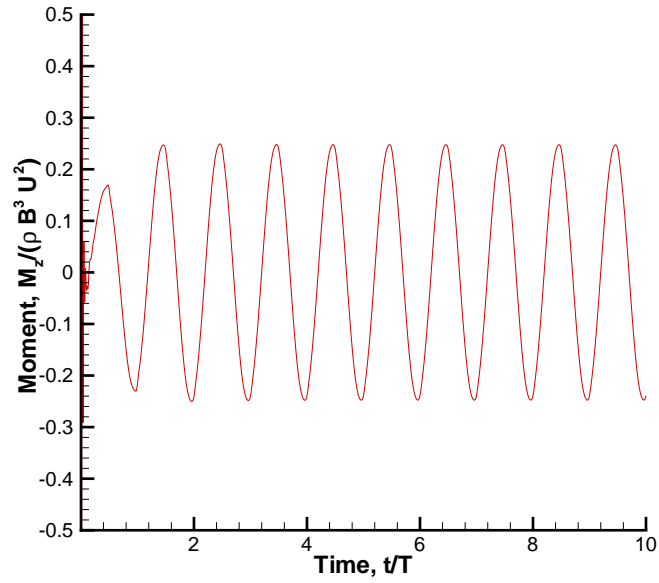
Figure 5.37: Time history of hydrodynamic moment for $Fn_b = 0.8$, 4% bilge keel and $\alpha_o = 0.05$

direction. Comparing time instants half a period apart, it can be seen that the shed vortices are symmetrical.
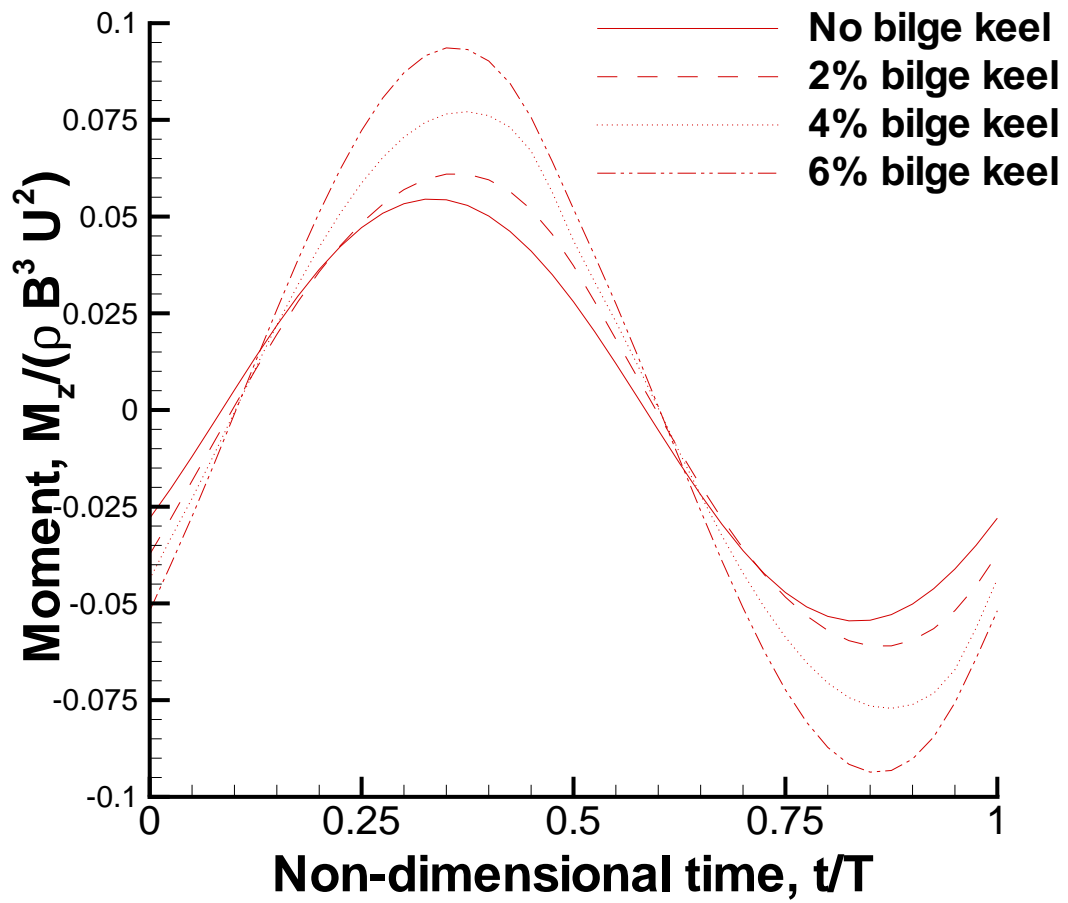
Figure 5.38: Hydrodynamic moment for $Fn_b = 0.8$ and $\alpha_o = 0.05$, for the four different hull geometries: No bilge keel, 2%, 4% and 6% bilge keels
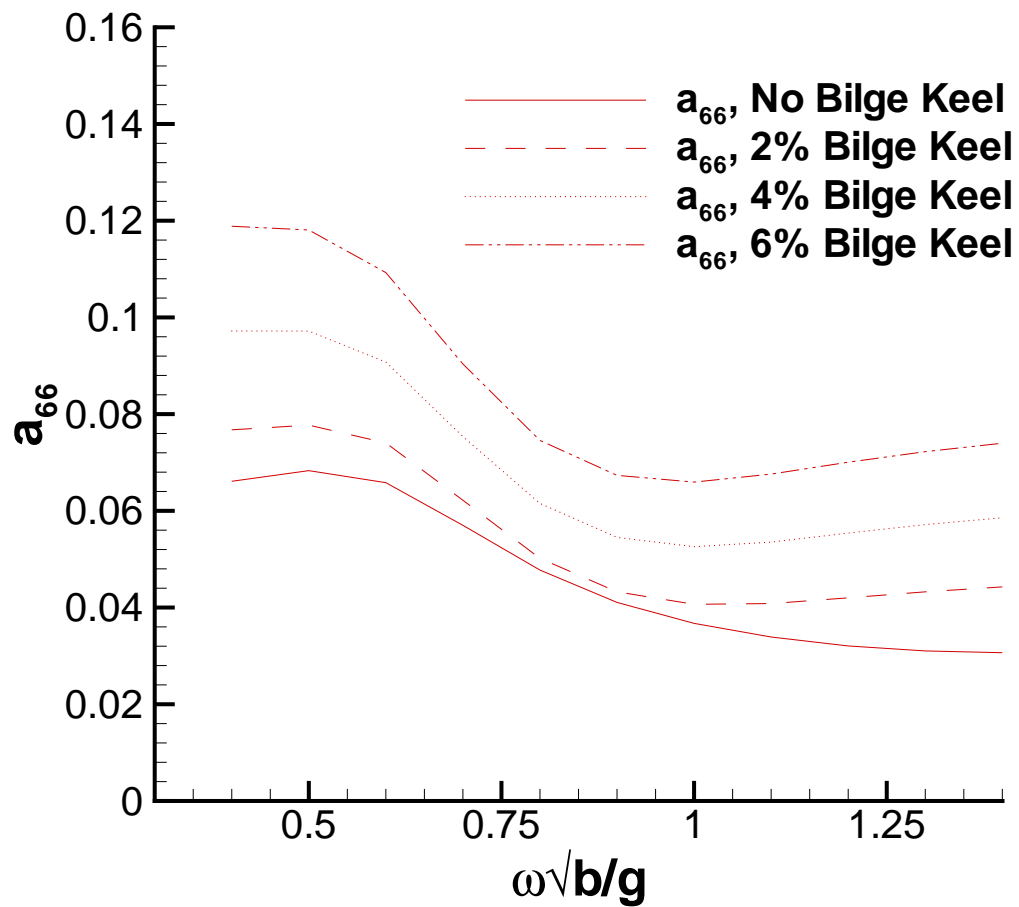
Figure 5.39: Comparison of roll added-mass coefficients obtained from present method for four different hull geometries: No bilge keel, 2%, 4% and 6% bilge keels ($\alpha_o = 0.05$, $0.4 \leq Fn_b \leq 1.4$)
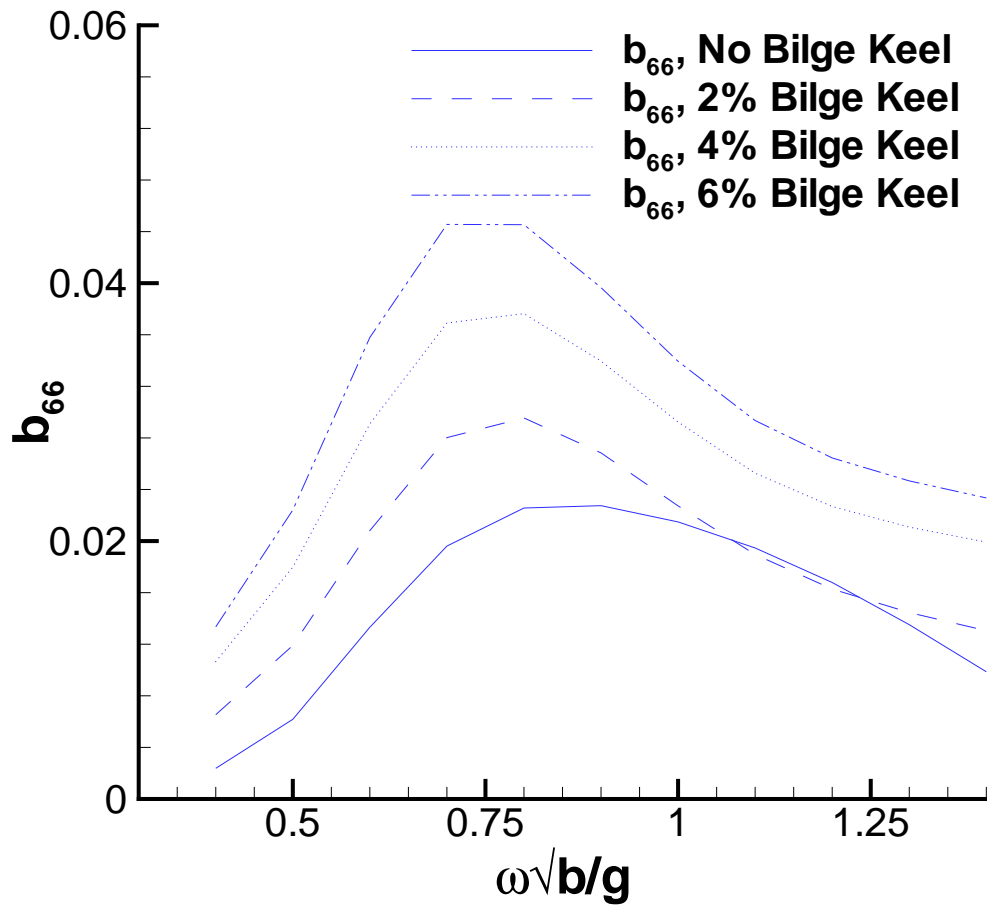
Figure 5.40: Comparison of roll damping coefficients obtained from present method for four different hull geometries: No bilge keel, 2%, 4% and 6% bilge keels ($\alpha_o = 0.05$, $0.4 \leq Fn_b \leq 1.4$)

t = 0

Figure 5.41 (a) t = 0

t = T/4

Figure 5.41 (b) t = $\frac{T}{4}$

151

t = T/2
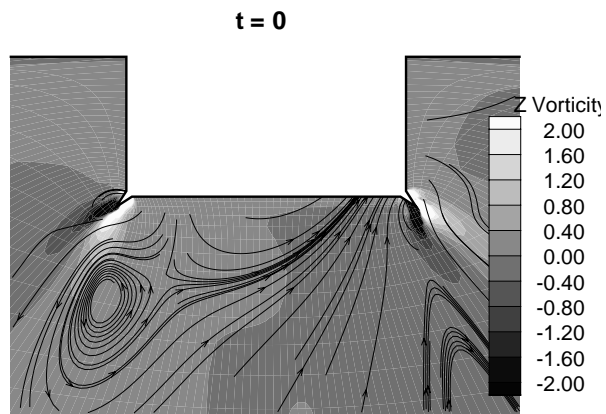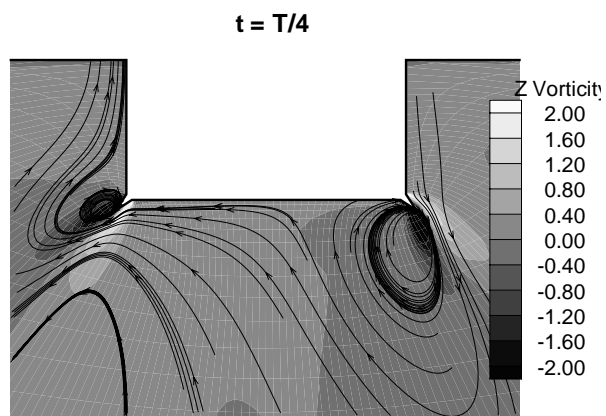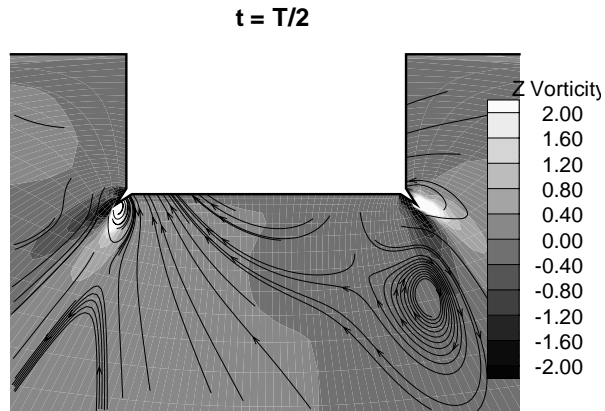
Figure 5.41 (c) t = $\frac{T}{2}$
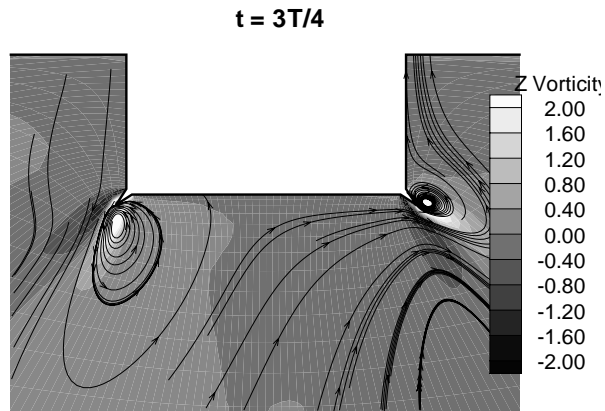
t = 3T/4

Figure 5.41 (d) t = $\frac{3T}{4}$

Figure 5.41: Flow-field around the hull at four time instants: (a) t = 0, (b) t = $\frac{T}{4}$, (c) t = $\frac{T}{2}$ and (d) t = $\frac{3T}{4}$ (6% bilge keel, $\alpha_o = 0.05$, $Fn_b = 0.8$)

152

Chapter 6

Conclusions and Recommendations

6.1 Conclusions

A marriage of the stator-rotor-pod is seen in the Siemens Schottel Propuslor (SSP) [Blenkey 1997] (see Figure 1.1). This propulsor features the Schottel Twin Propeller (STP), where the propeller load is distributed 50/50 to two propellers, one forward and one aft of a lower housing. This housing features two airplane type fins (similar to stator blades) that recover rotational energy from the forward propeller. The STP in itself achieves efficiencies up to 20% higher than standard Rudder-propellers. Conventional high power, low speed synchronous motors are so large and heavy that they must be housed within underwater housings with a diameter of as much as 60% that of the propeller diameter, with a dramatic negative influence on the unit's overall efficiency. Siemens has developed permanently-excitepd synchronous motors with a longitudinal electrical flow design, which allows a significant reduction in the diameter of the motor and, in turn, in the diameter of the housing of a podded drive. This allows optimum hub/propeller diameter ratios to be achieved.

This is just one example of the growing complexity of marine propulsors. As the marine industry's demand for efficient propulsors increases, better and robust CFD tools are required to handle the complex geometries and difficult flow conditions inherent to the new design propulsors. This work is an effort towards that end.

153

A vortex lattice method based potential solver has been successfully coupled with a finite volume method based Euler solver to solve for flow around multi-component and podded propulsor systems. Convergence studies for the method as well comparison with experimental data has been performed for both a stator-rotor configuration and a pull-type podded propulsor. For a simple pod geometry, different propeller configurations have been solved for and it has been found that the pull-type propulsor offers maximum advantage in terms of drag reduction. Numerical results have been compared with experimental data as well as with results from a coupled viscous/potential flow code for a single pulling podded propulsor and the values compare well.

Another solver based on the finite volume method has been developed for solving the unsteady, two-dimensional Euler and Navier-Stokes equations. This has been validated extensively using simple tests for which analytical results are known, all the while advancing in a logical manner towards the final goal of studying the separated flow past bilge keels fitted to the hull of a FPSO. In order to validate the adequacy of the Euler solver for capturing the effects accurately, results for oscillating flow past a flat plate have been obtained using both the developed solver and a laminar, unsteady Navier-Stokes solver. The force history obtained compares well and justifies the use of the Euler solver for modeling strongly separated flow. As a first step towards modeling of hull motions, the heave hydrodynamic coefficients for a rectangular hull in deep water have been compared with results presented in [Newman 1977]. Next, results are presented for a hull, with and without bilge keels, undergoing roll motions. The added-mass coefficients obtained from the present method are much higher compared to those presented by [Yeung et al. 2000]. The reason for this discrepancy needs to be investigated. Once the issue has been re-

154

solved, it would be possible to make fair comparisons with the experimental data presented in [Yeung et al. 2000]. The coefficients obtained for different bilge keel depths and forcing function amplitudes are compared and the effect of the bilge keels on roll motion mitigation is demonstrated. The results show that the present method can successfully simulate most of the characteristics of the physical flow, including the vortex shedding.

6.2 Recommendations

The present work is but a first step in developing a robust and accurate tool for modeling flow past bilge keels. Following are some recommendations for further research that needs to be done before the final goal is achieved.

- Determination of three-dimensional hydrodynamic coefficients: The present method determines the two-dimensional hydrodynamic coefficients for a 2D hull section. The final goal is to estimate the hydrodynamic coefficients for a 3D ship hull. This can be done using *strip theory*. Strip theory has been extensively used since the 1950's to provide reliable estimates of sea keeping performance for a wide range of hull forms and sea conditions. Calculations are made in the frequency domain, with some modifications due to forward speed. There are three main stages to computing the sea keeping response:

  1. The ship is divided into a number of transverse sections, and the two-dimensional hydrodynamic coefficients are calculated for each section. The barge-type rectangular hull section used in the present work is typical for the mid-ship region of the FPSO. As the bilge keels are likely

to be located around this length, using strip theory simply involves performing repeated calculations for simple rectangular hull forms, which the method has been shown capable of doing.

2. The two-dimensional values obtained are integrated along the length of the vessel, to obtain the global coefficients of the coupled motions of the vessel. It is often assumed that the vertical plane and horizontal plane motions may be considered independently. Thus the coupled heave and pitch responses are computed and then the coupled sway, roll and yaw.

3. Having obtained the global hydrodynamic coefficients, the equations of motion can now be solved to give the amplitudes and phases of the heave, pitch, sway, roll and yaw motions. Once the motions are known, it is possible to calculate the wave induced shear force and bending moment.

- Combine with potential flow solver: A potential flow solver such as WAMIT is an accurate and fast tool to determine the hydrodynamic coefficients. However, due to the assumptions of potential flow theory, the effects of the separated flow cannot be captured by it. That is where the present tool fits in. It provides a fast and computationally cheap (compared to a viscous solver) means of determining the hydrodynamic coefficients which include the separation effects. These can be used to correct the coefficients from WAMIT and therefore, model the motions of the FPSO better.

- Three-dimensional unsteady Euler solver: Another approach to determine the 3D hydrodynamic coefficients would be to extend the present method to three dimensions. This would allow modeling of the entire ship hull.

- Inclusion of incident waves: The present method assumes that the forcing function is periodic and known. However, in real sea environment, this is never true. A more useful tool would have allow the user to specify a given sea-state and study the resulting motions.

- For the coupled VLM/FVM solver, extensive validation tests are required before contemplating the application of the technique to real life problems. Further validations are required and results need to be compared with experimental data, for more realistic geometries. The method can just as easily be extended for multi-component podded geometries. Future work in this direction would include prediction of cavitation inception on the strut. This can also be extended to rudder geometries. Using the hydrofoil version of a panel code such as PROPCAV would allow rudder cavitation to be studied.

157

Bibliography

Alessandrini, B. and Delhommeau, G. (1995). A multigrid velocity-pressure-free surface elevation fully coupled solver for turbulent incompressible flow around a hull calculations. In *Proceedings of Ninth International Conference on Numerical Methods in Laminar and Turbulent Flows*, pages pp. 1173–1184, Atlanta, USA.

Anderson, J. (1995). *Computational Fluid Dynamics: The Basics with Applications*. McGraw-Hill, Inc., New York.

Blenkey, N. (1997). Getting twin propeller efficiency from a pod. *Marine Log*.

Bowling, L. (1987). Design of a non-axisymmetric stator for improved propeller performance. Master's thesis, MIT.

Breslin, J., Van Houten, R., Kerwin, J., and Johnsson, C.-A. (1982). Theoretical and experimental propeller-induced hull pressures arising from intermittent blade cavitation, loading, and thickness. *Trans. SNAME*, 90.

Choi, J.-K. (2000). *Vortical Inflow – Propeller Interaction Using an Unsteady Three-Dimensional Euler Solver*. PhD thesis, Department of Civil Engineering, The University of Texas at Austin.

Choi, J.-K. and Kinnas, S. (1998). A 3-D Euler solver and its application on the analysis of cavitating propellers. In *Proceedings of the 25th ATTC*, Iowa City, Iowa. American Towing Tank Conference.

Choi, J.-K. and Kinnas, S. (2000a). Non-axisymmetric effective wake prediction by using an unsteady three-dimensional Euler solver. In *Propellers/Shafting '00 Symposium*, Virginia Beach, VA. Soc. Naval Arch. & Marine Engnrs.

Choi, J.-K. and Kinnas, S. (2000b). An unsteady 3-D Euler solver coupled with a cavitating propeller analysis method. In *23rd Symposium on Naval Hydrodynamics*, Val de Reuil, France.

Choi, J.-K. and Kinnas, S. (2001). Prediction of Non-axisymmetric Effective Wake by a Three-Dimensional Euler Solver. *Journal of Ship Research*, 45(1):pp. 13–33.

Chorin, A. J. (1967). A numerical method for solving incompressible viscous flow problems. *Journal of Computational Physics*, 2:pp.12–26.

Courant, R., Friedrichs, K., and Lewy, H. (1967). On the partial difference equations of mathematical physics. *IBM Journal*, pages pp.215–234.

Dai, C., Gorski, J., and Haussling, H. (1991). Computation of an integrated ducted propulsor/stern performance in axisymmetric flow. In *Propellers/Shafting '91 Symposium*, Virginia Beach, VA. Soc. Naval Arch. & Marine Engnrs.

Faltinsen, O. and Sortland, B. (1987). Slow drift eddy making damping of a ship. *Applied Ocean Research*, 9(1):pp. 37–46.

Gawn, R. and Burrill, L. (1957). Effect of cavitation on the performance of a series of 16 in. model propellers. *Transactions INA*, 99:pp. 690–728.

Ghassemi, H. and Allievi, A. (1999). A Computational Method for the Analysis of Fluid Flow and Hydrodynamic Performance of Conventional and Podded Propulsion Systems. *Oceanic Engineering International*, 3(1):pp. 101–115.

159

Greeley, D. and Kerwin, J. (1982). Numerical methods for propeller design and analysis in steady flow. *Trans. SNAME*, vol 90.

Hsin, C.-Y., Chou, S.-K., and Chen, W.-C. (2002). A new propeller design method for the pod propulsion system. In *Proceedings of Twenty-Fourth Symposium on Naval Hydrodynamics*, Fukuoka, Japan.

Huang, T. and Cox, B. (1977). Interaction of afterbody boundary layer and propeller. In *Symposium on Hydrodynamics of Ship and Offshore Propulsion System*, Høvik outside Oslo.

Huang, T. and Groves, N. (1980). Effective wake : Theory and experiment. In *13th Symposium on Naval Hydrodynamics*, Tokyo.

Huang, T., Wang, H., Santelli, N., and Groves, N. (1976). Propeller/stern boundary layer interaction on axisymmetric bodies : Theory and experiment. Technical Report DTNSRDC 76-0113, DTNSRDC.

Hughes, M. (1993). *Analysis of Multi-component Ducted Propulsors in Unsteady Flow*. PhD thesis, M.I.T., Department of Ocean Engineering.

Hughes, M. and Kinnas, S. (1991). A analysis method for a ducted propeller with pre-swirl stator blades. In *Propellers/Shafting '91 Symposium*, pages 1–8 (paper No. 15), Virginia Beach, VA. Soc. Naval Arch. & Marine Engnrs.

Hughes, M. and Kinnas, S. (1993). Unsteady flows around multi-component integrated propulsors. In *Forum on Unsteady Flows, (FED-Vol. 157)*, pages 21–31. Fluids Engineering Division, ASME.

HYDROCOMP, I. (1999). Modeling tractor-style azimuthing podded drives. Technical Report 127, HYDROCOMP Inc.

Kasten, M. (2002). An overview of a few common roll attenuation strategies for motor yachts and motor sailors.

Kerwin, J., Keenan, D., Black, S., and Diggs, J. (1994). A coupled viscous/potential flow design method for wake adapted multi-stage, ducted propulsors using generalized geometry. *Trans. SNAME*, 102.

Kerwin, J. and Lee, C.-S. (1978). Prediction of steady and unsteady marine propeller performance by numerical lifting-surface theory. *Trans. SNAME*, vol 86.

Kerwin, J., Taylor, T., Black, S., and McHugh, G. (1997). A coupled lifting-surface analysis technique for marine propulsors in steady flow. In *Propellers/Shafting '97 Symposium*, pages 1–15 (Paper No. 20), Virginia Beach, VA. Soc. Naval Arch. & Marine Engnrs.

Kerwin, J. E., Coney, W. B., and Hsin, C.-Y. (1988). Hydrodynamic aspects of propeller/stator design. In *Proceedings of the Propellers '88 Symposium*, number 3, Virginia Beach, VA. SNAME.

Kinnas, S. (1991). Leading-edge corrections to the linear theory of partially cavitating hydrofoils. *Journal of Ship Research*, 35(1):pp. 15–27.

Kinnas, S. (1992). A general theory for the coupling between thickness and loading for wings and propellers. *Journal of Ship Research*, 36(1):pp. 59–68.

Kinnas, S. (1996). An international consortium on high-speed propulsion. *Marine Technology*, 33(3):pp. 203–210.

Kinnas, S. ((editor) 1999). University/Navy/Industry Consortium on Cavitation Performance of High Speed Propulsors - Presentations and Progress Reports - 11th Steering Committee Meeting. Dept. of Civil Engineering, UT Austin.

Kinnas, S. ((editor) 2001). University/Navy/Industry Consortium on Cavitation Performance of High Speed Propulsors - Presentations and Progress Reports - 15th Steering Committee Meeting. Dept. of Civil Engineering, UT Austin.

Kinnas, S. ((editor) 2002). University/Navy/Industry Consortium on Cavitation Performance of High Speed Propulsors - Presentations and Progress Reports - 18th Steering Committee Meeting. Dept. of Civil Engineering, UT Austin.

Kinnas, S. and Fine, N. (1989). Theoretical prediction of the midchord and face unsteady propeller sheet cavitation. In *Proceedings of the Fifth International Conference on Numerical Ship Hydrodynamics*, Hiroshima, Japan.

Kinnas, S., Griffin, P., Choi, J.-K., and Kosal, E. (1998). Automated design of propulsor blades for high-speed ocean vehicle applications. *Trans. SNAME*, 106.

Kinnas, S. and Pyo, S. (1999). Cavitating propeller analysis including the effects of wake alignment. *Journal of Ship Research*, 43(1):pp. 38–47.

Klaka, K. (2001). A simplified roll model. Technical Report 2001-09, Center for Marine Science and Technology, Curtin University of Technology, Perth, Australia.

Kudo, T. and Kinnas, S. (1995). Application of vortex/source lattice method on supercavitating propellers. In *24th American Towing Tank Conference*, College Station, TX.

Lee, C.-S. (1979). *Prediction of Steady and Unsteady Performance of Marine Propellers with or without Cavitation by Numerical Lifting Surface Theory*. PhD thesis, M.I.T., Department of Ocean Engineering.

Lee, H., Gu, H., Kakar, K., and Kinnas, S. (2001). Mpuf-3a (version 2.0) user's manual and documentation. Technical Report No. 01-5, Ocean Engineering Group, UT Austin.

Maskew, B. (1990). USAERO, A Time-stepping Analysis Method for the Flow About Multiple Bodies in General Motions, User's Manual . Technical report, Analytical Methods, Inc., Redmond, WA.

Miller, R., Gorski, J., and Fry, D. (2002). Viscous roll predictions of a cirular cylinder with bilge keels. In *Proceedings of Twenty-Fourth Symposium on Naval Hydrodynamics*, Fukuoka, Japan.

Newman, J. (1977). *Marine Hydrodynamics*. The MIT Press, Cambridge, Massachusetts.

Ohkusu, M., editor (1996). *Advances in Marine Hydrodynamics*. Computational Mechanics Publications, Southampton, UK.

Panton, R. (1996). *Incompressible Flow*. John Wiley & Sons, New York, 2nd edition.

Patankar, S. (1980). *Numerical Heat Transfer and Fluid Flow*. Hemisphere Publishing, New York.

Rhie, C. and Chow, W. (1983). Numerical study of the turbulent flow past an airfoil with trailing edge separation. *AIAA Journal*, 21(11):pp.1525–1532.

Sanchez-Caja, A., Rautaheimo, P., and Siikonen, T. (1999). Computation of the incompressible viscous flow around a tractor thruster using a sliding-mesh technique. In *Proceedings of Seventh International Conference on Numerical Ship Hydrodynamics*, France.

Sarpkaya, T. and O'Keefe, J. (1995). Oscillating flow about two- and three dimensional bilge keels. In *Proceedings of the 14th International Conference on Offshore Mechanics and Arctic Engineering*, pages pp. 263–270, Copenhagen, Denmark.

Shih, W.-Z. (1988). *A Combined Euler Equation/Surface Panel Solution to The Shear Interaction Problem of An Open or Ducted Propeller*. PhD thesis, Department of Ocean Engineering, M.I.T.

Stern, F., Kim, H., Patel, V., and Chen, H. (1988a). Computation of viscous flow around propeller-shaft configurations. *Journal of Ship Research*, 32(4):pp.263–284.

Stern, F., Kim, H., Patel, V., and Chen, H. (1988b). A viscous-flow approach to the computation of propeller- hull interaction. *Journal of Ship Research*, 32(4):pp. 246–262.

Sturova, I. and Motygin, O. (2002). Radiation problem for an interface-piercing cylinder in a two-layer fluid. In 17_{th} *International Workshop on Water Waves and Floating Bodies*, Cambridge, UK.

Szantyr, J. (2002). Hydrodynamic model experiments with pod propulsors. *Oceanic Engineering International*, 5(2):pp. 95–103.

164

Tsakonas, S., Jacobs, W., and Liao, P. (1983). Prediction of steady and unsteady loads and hydrodynamic forces on counterrotating propellers. *Journal of Ship Research*, 27(3):pp. 197–214.

Vartdal, L. and Bloch, F. (2001). Ferrycat 120 propulsion aspects and manoeuvring capabilities. In *Proceedings of First International Conference on Double-ended Ferries*, Molde, Norway.

Vartdal, L., Gjerde, K. M., Bloch, F., and Sittanggang, P. (1999). Application of various cfd methods in the development of the azipull podded propulsion system. In *The International CFD Conference in Ship Hydrodynamics*, Ulsteinvik, Norway.

Vugts, J. (1968). The hydrodynamic coefficients for swaying, heaving and rolling cylinders in a free surface. In *International Shipbuilding Progress*, pages pp. 251–276.

Warren, C. (1999). *Prediction of Propulsor-Induced Maneuvering Forces Using a Coupled Viscous/Potential-Flow Method for Integrated Propulsors*. PhD thesis, Department of Ocean Engineering, MIT.

Warren, C., Taylor, T., and Kerwin, J. (2000). A coupled viscous/potential-flow method for the prediction of propulsor-induced maneuvering forces. In *Propellers/Shafting '00 Symposium*, Virginia Beach, VA. Soc. Naval Arch. & Marine Engnrs.

Yang, C.-J., Wang, G., Tamashima, M., Yamazaki, R., and Koizuka, H. (1992). Prediction of the unsteady performance of contra-rotating propellers by lifting surface theory. *Trans. of the West-Japan Society of Naval Architects*, (No. 83):pp. 47–65.

Yeung, R. and Ananthakrishnan, P. (1992). Oscillation of a floating body in a viscous fluid. *Journal of Engineering Mathematics*, 26:pp. 211–230.

Yeung, R., Liao, S.-W., and D., R. (1998). Hydrodynamic coefficients of rolling rectangular cylinders. *International Journal of Offshore and Polar Engineering*, 8(4):pp. 241–250.

Yeung, R., Roddier, D., Liao, S.-W., Alessandrini, B., and Gentaz, L. (2000). On roll hydrodynamics of cylinders fitted with bilge keels. In *Proceedings of Twenty-Third Symposium on Naval Hydrodynamics*, Val De Reuil, France.

Vita

Karan Kakar was born in Indore, India on February 7, 1978. He is the son of Sheila and Ranjan Kakar. He obtained his Bachelor of Technology in Naval Architecture from the Indian Institute of Technology at Madras in May, 2000. He started his Masters program in civil engineering at The University of Texas at Austin in September, 2000.

Permanent address: Apt 1036, B-1, Vasant Kunj
　　　　　　　　　New Delhi-110070, India

This thesis was typeset with LATEX‡ by the author.

---

‡LATEX is a document preparation system developed by Leslie Lamport as a special version of Donald Knuth's TEX Program.